

**University of Miami  
Scholarly Repository**

---

Open Access Theses

Electronic Theses and Dissertations

---

2016-12-07

# The Role of Air-Sea Interaction in Structure and Intensity Change in Hurricane Ophelia (2005): Coupled Modeling and RAINEX Observations

Andrew Wyatt Smith  
*University of Miami*

Follow this and additional works at: [http://scholarlyrepository.miami.edu/oa\\_theses](http://scholarlyrepository.miami.edu/oa_theses)

---

## Recommended Citation

Smith, Andrew Wyatt, "The Role of Air-Sea Interaction in Structure and Intensity Change in Hurricane Ophelia (2005): Coupled Modeling and RAINEX Observations" (2016). *Open Access Theses*. Paper 636.

---

This Open access is brought to you for free and open access by the Electronic Theses and Dissertations at Scholarly Repository. It has been accepted for inclusion in Open Access Theses by an authorized administrator of Scholarly Repository. For more information, please contact [repository.library@miami.edu](mailto:repository.library@miami.edu).

UNIVERSITY OF MIAMI

THE ROLE OF AIR-SEA INTERACTION IN STRUCTURE AND INTENSITY  
CHANGE IN HURRICANE OPHELIA (2005): COUPLED MODELING AND  
RAINEX OBSERVATIONS

By

Andrew W. Smith

A THESIS

Submitted to the Faculty  
of the University of Miami  
in partial fulfillment of the requirements for  
the degree of Master of Science

Coral Gables, Florida

December 2016

©2016  
Andrew W. Smith  
All Rights Reserved

UNIVERSITY OF MIAMI

A thesis submitted in partial fulfillment of  
the requirements for the degree of  
Master of Science

THE ROLE OF AIR-SEA INTERACTION IN STRUCTURE AND INTENSITY  
CHANGE IN HURRICANE OPHELIA (2005): COUPLED MODELING AND  
RAINEX OBSERVATIONS

Andrew W. Smith

Approved:

---

Shuyi S. Chen, Ph.D.  
Professor of Ocean Sciences

---

Mohamed Iskandarani, Ph.D.  
Professor of Ocean Sciences

---

William M. Drennan, Ph.D.  
Professor of Ocean Sciences

---

Guillermo Prado, Ph.D.  
Dean of the Graduate School

---

Frank D. Marks, Ph.D.  
Director of the Hurricane Research Division  
NOAA AOML  
Miami, Florida

SMITH, ANDREW W.

(M.S., Meteorology and Physical Oceanography)

(December 2016)

The Role of Air-Sea Interaction in Structure and  
Intensity Change in Hurricane Ophelia (2005):  
Coupled Modeling and RAINEX Observations

Abstract of a thesis at the University of Miami.

Thesis supervised by Professor Shuyi S. Chen

No. of pages in text. (143)

Intensity and intensity change remain one of the most significant challenges in tropical cyclone (TC) prediction. Instantaneous intensity and its evolution result from complex storm-environment interactions and internal structure changes across multiple time and spatial scales. These interactions truly couple the TC to the ocean as well as the ambient environment, however have been insufficiently observed and are difficult to model. Many earlier studies have demonstrated the impact of air-sea coupling to TC intensity, as well as the physical processes involved in the ocean response to TC passage. More recent work however has shown air-sea coupling affects both structure and intensity.

Hurricane Ophelia in 2005 was well – observed by research reconnaissance aircraft during the fortuitous Hurricane Rainband and Intensity Change Experiment (RAINEX) field campaign. This mission included unprecedented airborne Doppler radar and dropsonde sampling of internal inner-core and rainband structures. These observations, supplemented by satellite, buoy, and analysis products captured a unique structural evolution in Ophelia that involved the collapse and recovery of its inner core. This thesis

will investigate the structure and intensity changes that occurred in Hurricane Ophelia as a result of air-sea interaction, with particular focus on the impact of interactive ocean coupling and structure changes. Additionally, based on observations of double-eyewall-like structure during part of Ophelia's life cycle we will examine the intensity changes to address a possible interrupted or incipient eyewall replacement cycle (EWRC). A high-resolution, coupled atmosphere-ocean (AO) numerical model (UWIN-CM) simulation initialized with vortex-following nested grids and global analysis fields correctly captured the inner eyewall collapse, discrete outer secondary rainband/eyewall, and recovery of distinct eyewall and rainband features as well as more appropriately simulating the true storm intensity. Model output will be used to evaluate the structure and intensity changes between uncoupled (atmosphere-only) and coupled simulations, and then focus more closely on air-sea interaction instigating changes in air-sea enthalpy flux.

Good agreement between RAINEX observations and the coupled model simulation allowed for detailed analysis of the role of air-sea interaction. Without an interactive ocean, the uncoupled TC is too strong and the lack of coupling prohibits feedbacks and air-sea interactions that modify air-sea enthalpy flux and ultimately storm structure and intensity. The presence of an interactive ocean is also critical to producing the observed induced cold pool and its distribution relative to TC wind stress. The TC surface circulation feedback on the ocean was found to be important for locally modifying air-sea enthalpy flux in the inner core via upper ocean cooling, while also being important to air-sea enthalpy flux distribution when Ophelia's circulation becomes large after interacting with the cold pool. Advection of high enthalpy air at distant radii and lower enthalpy air from over the cold pool in the inner core region helped to support

(suppress) convection far from (near) the storm center during the expansion, particularly a discrete outer rainband that may have served as a secondary eyewall. Finally, it should be noted that even the coupled simulation overestimates wind and precipitation intensity and initial SST, highlighting the outstanding challenge of model initial condition errors and appropriate parameterizations for convection and air-sea interaction physical processes in the complex TC-atmosphere-ocean environment.

## **DEDICATION**

To my parents Jason and Melissa Smith, grandfather Dr. Winston Smith, and Alison Enchelmaier, for their wisdom, love, encouragement, and support of me, my pursuit of science, and this work – the culmination of youthfully fostered curiosity, stubbornness, and the hope to benefit others in some small way.

## **ACKNOWLEDGEMENTS**

Sincere thanks and gratitude foremost to my advisor, Dr. Shuyi S. Chen, for her guidance and support in my research and for the wisdom, knowledge, and perspective that has and will continue to cultivate my growth as a scientist in the future.

I would also like to thank my committee members, Dr. Frank D. Marks, Dr. Will M. Drennan, and Dr. Mohamed Iskandarani, for your expertise, invaluable feedback, and ideas on the scope and analysis of this work.

Special thanks to Dr. Frank D. Marks, Dr. Paul D. Reasor, and Dr. John F. Gamache, for providing the aircraft tail radar real-time diagnostic software which was very useful for presentation and analysis of the hurricane observations herein. I feel very fortunate to have had the opportunity and privilege to involve life-long scientists from the Hurricane Research Division with your wealth of experience (and Dr. Marks, your stories of Hugo) as part of the execution of this study.

Thanks to Dr. Mohamed Iskandarani, for introducing me to what lies behind the scenes of modeling in his computational fluid dynamics course and for his time and advice as a student in general.

Thanks to my friends and colleagues within the Hurricanes and Coupled Atmosphere-Ocean Systems research lab, with particular thanks to Dr. Milan Curcic and Dr. Brandon W. Kerns - for their help with coupled model implementation and troubleshooting,

programming and other questions and numerous journeys for coffee. Thanks to Dr. Falko Judt, for his advice, friendship, and for sharing his passion for hurricanes with me while part of the lab.

Special thanks to Marc Michelsen from the University of Washington, for swiftly solving Linux problems and other computing magic during the course of this work.

Finally, I would like to thank the many friends I have gained as a member of the RSMAS community – especially Milan Curcic, Johnna Infanti, and Yemi Adebiyi, who I see as kindred spirits.

This research has been supported by grants from the National Science Foundation (NSF) and the Gulf of Mexico Research Initiative (GoMRI).

## TABLE OF CONTENTS

|                                                                                  | Page |
|----------------------------------------------------------------------------------|------|
| List of Figures                                                                  | viii |
| Chapter                                                                          |      |
| 1      INTRODUCTION                                                              | 1    |
| 1.1    Motivation                                                                | 1    |
| 1.2    Background and literature review                                          | 2    |
| 1.2.1 Air-sea interaction and tropical cyclone intensity                         | 2    |
| 1.2.2 Structure and intensity change via air-sea interaction                     | 8    |
| 1.2.3 Hurricane Ophelia                                                          | 14   |
| 1.3    Science objectives                                                        | 21   |
| 2      MODEL DESCRIPTION AND ANALYSIS METHODOLOGY                                | 22   |
| 2.1    The numerical model                                                       | 22   |
| 2.2    Analysis methodology                                                      | 25   |
| 2.2.1 Track and intensity verification                                           | 25   |
| 2.2.2 Storm-relative flight-level and vertical transects                         | 26   |
| 2.2.3 Earth-relative spatial maps                                                | 27   |
| 2.2.4 Azimuthal average analyses                                                 | 28   |
| 2.2.5 Model simulated buoy verification                                          | 28   |
| 2.2.6 Timeseries and Hovmoller diagrams                                          | 29   |
| 2.2.7 Contoured frequency by altitude diagrams                                   | 30   |
| 2.2.8 Summary                                                                    | 30   |
| 3      STRUCTURE AND INTENSITY EVOLUTION IN HURRICANE OPHELIA (2005)             | 33   |
| 3.1    Observational datasets                                                    | 34   |
| 3.1.1 Airborne radar                                                             | 34   |
| 3.1.2 Flight-level data and SFMR                                                 | 35   |
| 3.1.3 Satellite                                                                  | 35   |
| 3.1.4 Buoy                                                                       | 37   |
| 3.1.5 GPS dropsondes                                                             | 37   |
| 3.1.6 SHIPS wind shear product                                                   | 38   |
| 3.1.7 H*WIND analysis                                                            | 39   |
| 3.2    Asymmetric near-hurricane prior to cold pool formation                    | 39   |
| 3.3    Shallowing, asymmetric structure traversing cold pool                     | 50   |
| 3.4    Expanded, shallow storm with peripheral discrete convective rainband      | 60   |
| 3.5    New symmetric eye forms and convection reinvigorates over the Gulf Stream | 70   |
| 3.6    Summary                                                                   | 76   |

|     |                                                                             |     |
|-----|-----------------------------------------------------------------------------|-----|
| 4   | IMPACT AND ROLE OF AIR-SEA INTERACTION IN HURRICANE OPHELIA (2005)          | 81  |
| 4.1 | Model verification                                                          | 81  |
|     | 4.1.1 Track and intensity                                                   | 81  |
|     | 4.1.2 Storm environment and structure                                       | 83  |
| 4.2 | Role of air-sea interaction on inner-core collapse and recovery             | 103 |
|     | 4.2.1 Air-sea enthalpy flux modification and structure change               | 103 |
|     | 4.2.2 Storm size implications for local and non-local air-sea enthalpy flux | 113 |
|     | 4.2.3 Summary                                                               | 120 |
| 5   | CONCLUSIONS                                                                 | 127 |
| 5.1 | Role of air-sea interaction                                                 | 127 |
|     | REFERENCES                                                                  | 136 |

## LIST OF FIGURES

|                                                                                                                                                                                                                                                                                                                                                                                                                                                   | Page |
|---------------------------------------------------------------------------------------------------------------------------------------------------------------------------------------------------------------------------------------------------------------------------------------------------------------------------------------------------------------------------------------------------------------------------------------------------|------|
| 1.1 Ophelia's NHC best-track (a) 6-hourly positions and (b) intensity given by maximum sustained winds (kt) and minimum sea-level pressure (hPa). Black arrows indicate the two RAINEX flight missions (RF04 and RF05) during which Ophelia was a tropical cyclone.                                                                                                                                                                               | 15   |
| 1.2 NCAR/Penn-State 5 <sup>th</sup> -Generation Mesoscale Model (MM5) forecast rain rate (mm/hr) verified against GOES-12 infrared satellite brightness temperature imagery for (a,d) September 11 1100 UTC (b,e) September 11 1800 UTC, and (c,f) September 11 2200 UTC.                                                                                                                                                                         | 17   |
| 1.3 TRMM PR 85 GHz vertical polarization microwave brightness temperature (degrees Kelvin) for September 11 (a) 1510 (b) 1648, and (c) 1826 UTC. The magenta circle is roughly situated about the storm center.                                                                                                                                                                                                                                   | 18   |
| 1.4 TRMM PR 85 GHz polarization corrected (PCT) microwave brightness temperature (degrees Kelvin) for September 12 (a) 1415 (b) 1730, and September 13 (c) 1457 UTC. The magenta circle is sized according to the convective outer rainband in (a), and is the same size and position in (b) and (c), to show propagation and consolidation of convection during the recovery of Ophelia's inner core.                                            | 19   |
| 1.5 NASA AQUA-1 AMSR-E (a) 85 GHz PCT (degrees Kelvin) and (b) QuikSCAT Version 4 near-surface winds (knots) late on September 13. The magenta circle is situated at the outer radial edge of the strongest rain in (a), and is located at the same position and size in (b), to show the similar location of heavy rain and strong winds.                                                                                                        | 20   |
| 2.1 Schematic diagram of the UWIN-CM atmosphere and ocean component domains for Hurricane Ophelia.                                                                                                                                                                                                                                                                                                                                                | 23   |
| 3.1 (a) University of Wisconsin/CIMSS wind shear product (200-850 hPa deep-layer in colors, kt) overlaid with 200 hPa white streamlines for September 9 1500 UTC. The storm center location of Ophelia, Nate, and Maria are indicated by the tropical storm symbols (b) TRMM AMSR-E merged daily SST overlaid with Ophelia's track since September 9 0000 UTC and position at September 9 1600 UTC.                                               | 40   |
| 3.2 (a) NCEP final analysis (FNL, GFS + late observations) DLS maps for September 9 1800 UTC, September 10 0000 UTC, and September 10 1200 UTC (SHIPS uses real-time GFS). The black thick line denotes the storm track from September 9 0000 UTC through the time indicated. A black arrow shows the storm heading. The magenta arrow denotes the shear vector. The black circle indicates 200-km from storm center. Black quivers show the 200- |      |

- hPa wind (b) Timeseries of 6-hourly SHIPS DLS (black x's), FNL DLS (black line), and 6-hourly MWSP. All values are given in knots. 41
- 3.3 (a) NOAA HRD 3D Doppler Analysis (3D DA) composite flight-level radar reflectivity (dBZ) for September 9 1258 UTC – 1446 UTC. Azimuthal average flight-level RMR and value at that radius are indicated at top left. Black wind barbs give the flight level wind (kt) (b) Azimuthal average radar reflectivity profile (dBZ, black) and composite coverage along each azimuth (%), red) (c) Same as (a) except for flight-level wind speed. Black (grey) streamlines are at 0.5km (3 km) altitude. (d) Same as (b) except for tangential wind speed (kt, solid black) and radial wind speed (kt, dashed black). 43
- 3.4 Vertical transects of (a,c) radar reflectivity and (b,d) horizontal wind taken through the composites in Figure 3.3. Slices in (a) and (b) are taken across-track, whereas (c) and (d) are taken along-track. Contours in (a) and (c) denote 20 (light to moderate) and 40 (strong to intense) dBZ. In (b) and (d), quivers depict the indicated 2D wind structure. 45
- 3.5 (a) NOAA HRD 3D DA flight-level radar reflectivity composite as in Figure 3.3a, overlaid with the aircraft flight path September 9 1300 UTC – 1350 UTC (b) Profile of aircraft flight-level wind (kt, solid black), SFMR surface wind estimate (kt, dashed black), and flight-level radar reflectivity from the composite (dBZ, green). 46
- 3.6 (a) TRMM AMSR-E merged daily SST for September 9 with Ophelia's track since September 9 0000 UTC and center position at September 9 1600 UTC. The magenta 'x' indicates the position of the buoy NDBC 41010 (b) Same as (a), except overlaid with the latitude-longitude positions of the September 9 dropsondes (magenta) (c) Storm-relative location of the September 9 dropsondes by RMW (d) 0-1.5km equivalent potential temperature (EPT, deg K) profiles from the September 9 dropsondes (e) Same as (d) except for air temperature (TAIR, deg C) (f) 0.6m water temperature (red) and surface pressure (black) measured by NDBC 41010, September 9 – 15. 48
- 3.7 TRMM AMSR-E merged daily SST overlaid with Ophelia's storm track since September 9 0000 UTC for (a) September 11 (center position 1600 UTC) (b) September 12 (center position at 1600 UTC). The black solid contour denotes 26.5°C. 51
- 3.8 Same as 3.3, except for September 11 1616 UTC – 1812 UTC. 52
- 3.9 Same as 3.4, except for September 11 1616 UTC – 1812 UTC. 54
- 3.10 Same as 3.5, except for September 11 1616 UTC – 1812 UTC. 56

- 3.11 (a) TRMM AMSR-E merged daily SST for September 11 with Ophelia's track since September 9 0000 UTC and center position at September 11 1600 UTC. The magenta 'x' indicates the position of the buoy NDBC 41002 (b) Same as (a), except overlaid with the latitude-longitude positions of the September 11 dropsondes (magenta) (c) Storm-relative location of the September 11 dropsondes by RMW (d) 0-1.5km equivalent potential temperature (EPT, deg K) profiles from the September 11 dropsondes (e) Same as (d) except for air temperature (TAIR, deg C) (f) 0.6m water temperature (red) and surface pressure (black) measured by NDBC 41002, September 9 – 15. 58
- 3.12 Same as 3.3, except for September 12 2000 UTC – 2338 UTC. 61
- 3.13 Same as 3.4, except for September 12 2000 UTC – 2338 UTC. 63
- 3.14 Same as 3.5, except for September 12 2000 UTC – 2338 UTC. 64
- 3.15 HRD H\*WIND analysis surface wind (kt, colors and barbs) in storm-relative space for September 12 (a) 1330 UTC (b) 1930 UTC and September 13 (c) 0730 UTC (d) 1930 UTC. The magenta contour denotes 34kt (tropical storm force) winds. 67
- 3.16 Timeseries of H\*WIND-derived radius of maximum wind (RMW) (km, blue) and integrated kinetic energy (TJ, green) as in Powell and Reinhold (2007) for September 9 – 15. Letters correspond to the times in Figure 3.15. 67
- 3.17 TRMM AMSR-E merged daily SST overlaid with Ophelia's storm track since September 9 0000 UTC for (a) September 12 (center position 1600 UTC) (b) September 13 (center position at 1600 UTC). The black solid contour denotes 26.5°C. 70
- 3.18 University of Wisconsin/CIMSS Morphed Microwave (MIMIC; Wimmers and Velden, 2007) microwave brightness temperature imagery September 12 1200 UTC – September 13 1200 UTC for the indicated times in (a) – (f). 71
- 3.19 Same as 3.3, except for September 13 2000 UTC – September 14 0010 UTC. 72
- 3.20 Same as 3.4, except for September 13 2000 UTC – September 14 0010 UTC. 73
- 3.21 TRMM AMSR-E merged daily SST overlaid with Ophelia's storm track since September 9 0000 UTC for September 13 (center position 1600 UTC). The black solid contour denotes 26.5°C. The magenta contour outlines the

undisturbed Gulf Stream west and northwest of Ophelia's cold pool. The dashed arrow extending beyond the black dot follows Ophelia's future storm track through September 15 0000 UTC. 74

- 3.22 NOAA HURSAT 85 GHz polarization corrected (PCT) microwave brightness temperature (BRT, deg K) indicating moderate to intense convection at (a) September 12 1230 UTC (b) September 13 2330 UTC. The H\*WIND-derived RMW is indicated by the magenta circle. 75
- 3.23 NOAA HRD 3D DA contoured-frequency by altitude diagram for radar reflectivity during Stage 1, when Ophelia was near hurricane intensity. Radar reflectivity (dBZ) is given on the x-axis, altitude is given in on the y-axis. Colors reflect frequency (%) per dBZ per meter. The black dashed contour indicates 25% per dBZ per meter. 77
- 3.24 Same as 3.23, but for Stage 2, when Ophelia was interacting with its' cold pool. 78
- 3.25 Same as 3.23, but for Stage 3, when Ophelia was in a structural transition phase, with an expanded circulation and distant outer rainband. 79
- 3.26 Same as 3.23, but for Stage 4, when Ophelia recovers over the Gulf Stream. 80
- 4.1 NHC best track (black) and UWIN-CM UA (blue), AO (red) simulation storm tracks shown every 6h from September 9 – 15. 81
- 4.2 NHC best track (black) and UWIN-CM UA (blue), AO (red) simulation maximum wind speed intensity shown every 6h from September 9 – 15. 83
- 4.3 SHIPS (black) and UWIN-CM UA (blue), AO (red) simulation deep-layer (200 – 850 hPa) wind shear using the 200 – 800 km annulus from storm center. SHIPS shear was provided every 6h in both developmental (archive) data and from the FNL (real-time GFS) analysis, September 9 - 15. 84
- 4.4 (a) TRMM, UWIN-CM UA, and UWIN-CM AO SST (deg C) with NDBC 41010 position indicated by the magenta 'x' (b) as in (a) but for September 10 1800 UTC (c) NDBC 41010 storm-relative SST from the buoy (black), UWIN-CM UA (blue), and UWIN-CM AO (red). 86
- 4.5 (a) NOAA WP-3D 3D Doppler Analysis flight-level composite (Sep 9 1258 UTC – 1440 UTC) and UWIN-CM storm-relative composite (1300 UTC – 1400 UTC) radar reflectivity (b) same as (a) but for wind speed (c) corresponding observed and model 2D azimuthal average radius-height radar reflectivity and (d) wind speed. In rows (a) and (b), black circles show distance every 50km. Flight-level wind barbs are overlaid on reflectivity

|                                                                                                                                                                                                                                                                                                                                                                                                                           |     |
|---------------------------------------------------------------------------------------------------------------------------------------------------------------------------------------------------------------------------------------------------------------------------------------------------------------------------------------------------------------------------------------------------------------------------|-----|
| figures, 0.5 (black) and 3km (grey) streamlines are overlaid on wind figures.<br>For the 2D azimuthal average diagrams, reflectivity is contoured at 20 and 40<br>dBZ. Wind speed is contoured at 25 and 30 kt. Quivers show the radial-<br>vertical velocity with length normalized to unity.                                                                                                                            | 88  |
| 4.6 (a) TRMM, UWIN-CM UA, and UWIN-CM AO SST (deg C) with NDBC<br>41002 position indicated by the magenta ‘x’ (b) as in (a) but for September 12<br>0300 UTC (c) NDBC 41002 storm-relative SST from the buoy (black),<br>UWIN-CM UA (blue), and UWIN-CM AO (red). The black line shows the<br>storm track to the indicated time. The black dot is situated at the storm center.<br>The black circle denotes 200km radius. | 90  |
| 4.7 Same as 4.5, but comparing to observations taken September 11 1612 UTC –<br>1812 UTC.                                                                                                                                                                                                                                                                                                                                 | 92  |
| 4.8 (a) TRMM, UWIN-CM UA, and UWIN-CM AO SST (deg C) for September<br>12 0600 UTC. The black contour in TRMM (magenta in AO) indicates<br>26.5°C. The black line shows the storm track to the indicated time. The black<br>dot is situated at the storm center. The black circle denotes 200km radius.                                                                                                                    | 94  |
| 4.9 Same as 4.5, but comparing to observations taken September 12 2000 – 2338<br>UTC.                                                                                                                                                                                                                                                                                                                                     | 96  |
| 4.10 (a) TRMM, UWIN-CM UA, and UWIN-CM AO SST (deg C) for September<br>13 1200 UTC. The black contour in TRMM (magenta in AO) indicates<br>26.5°C. The black line shows the storm track to the indicated time. The black<br>dot is situated at the storm center. The black circle denotes 200km radius.                                                                                                                   | 98  |
| 4.11 Same as 4.5, but comparing to observations taken September 13 2000 UTC –<br>September 14 0010 UTC.                                                                                                                                                                                                                                                                                                                   | 99  |
| 4.12 Timeseries of azimuthal average latent heat flux at 50km (black), 100km<br>(red), 150km (green), and 200km (blue) for (a) UWIN-CM UA simulation and<br>(b) UWIN-CM AO simulation. MWSP is given in magenta for the simulations<br>in their respective panel                                                                                                                                                          | 101 |
| 4.13 Summary of TC-induced upper ocean cooling physical processes through a<br>sample TC in cross-section.                                                                                                                                                                                                                                                                                                                | 104 |
| 4.14 (a) T100 (left, deg C), azimuthal average T100 (center, blue), and<br>observed/model maximum wind speed for September 10 1800 UTC (b) same<br>as (a) except for September 12 0600 UTC. Azimuthal average surface wind<br>speed (kt) is given in the center panel.                                                                                                                                                    | 105 |

- 4.15 (a) storm-relative T100 (deg C), 0.5km streamlines (magenta, kt), and flight-level radar reflectivity (contoured at 20 and 40 dBZ) (b) quadrant azimuthal average surface wind speed (kt) and flight-level radar reflectivity (dBZ) with RMW and RMR indicated by the vertical blue and green lines (c) quadrant azimuthal average qSST (g/kg; green solid), qa10 (g/kg; dashed green), and equivalent potential temperature (deg K; orange). Azimuthal averages 0-200 km. Top row corresponds to September 11 0600 UTC, bottom row corresponds to September 12 0600 UTC. 107
- 4.16 (a) T100 (left, deg C), upper ocean along-track vertical transect (center), and observed/model maximum wind speed for September 12 1200 UTC (b) same as (a) except for September 12 1300 UTC. Azimuthal average T100 (blue, deg C) and surface wind speed (black, kt) is given in the center panel. 110
- 4.17 (a) storm-relative T100 (deg C), 0.5km streamlines (magenta, kt), and flight-level radar reflectivity (contoured at 20 and 40 dBZ) (b) quadrant azimuthal average surface wind speed (kt) and flight-level radar reflectivity (dBZ) with RMW and RMR indicated by the vertical blue and green lines (c) quadrant azimuthal average qSST (g/kg; green solid), qa10 (g/kg; dashed green), and equivalent potential temperature (deg K; orange). Azimuthal averages 0-200 km. Top row corresponds to September 12 1200 UTC, bottom row corresponds to September 13 1200 UTC. 111
- 4.18 Timeseries of UWIN-CM AO radius of maximum wind (blue, km) and maximum wind speed (magenta, kt), September 9 – 15. 114
- 4.19 2D azimuthal average radius-height diagrams of UWIN-CM AO wind speed (0-18 km, 0.5km intervals) at (a) September 12 0000 UTC (b) September 12 1200 UTC and (c) September 13 1200 UTC. Magenta lines denote 6km altitude and 75km radius. 115
- 4.20 Storm-relative UWIN-CM AO (a) surface current velocity (cm/s) (b) T100 (deg C) and (c) azimuthal average profiles of surface wind speed (m/s, black), T100 (deg C, blue), and surface current velocity (cm/s, purple). Top row is for September 12 0000 UTC, bottom row is for September 12 1200 UTC. 116
- 4.21 Timeseries of UWIN-CM AO maximum wind speed (black, kt) and integrated kinetic energy (using PR07 method; green, TJ), September 9 – 15. 119
- 4.22 Timeseries of UWIN-CM AO azimuthal average surface wind speed at 50km (black), 100km (red), 150km (green), and 200km (blue), September 9 – 15. 120

- 4.23 Timeseries of UWIN-CM AO (a) azimuthally averaged SST difference (red, deg C) and surface equivalent potential temperature advection (orange, K/hr) overlaid with a magenta line denoting zero (b) MWSP (black, kt) vs. IKE (green, TJ; PR07). 121
- 4.24 Timeseries of UWIN-CM AO (a) azimuthally averaged latent heat flux difference (black,  $\text{Wm}^{-2}$ ) overlaid with flight-level RMR (green, km) and surface RMW (blue, km). (b) Azimuthally averaged flight-level radar reflectivity difference (green, dBZ) and azimuthally averaged surface wind speed (blue, kt). Magenta line denotes zero. 124
- 5.1 Grouped contoured frequency by altitude (CFAD) difference summary diagrams for radar reflectivity during the (a) organization, (b) cold-pool interaction, (c) expansion, and (d) recovery stages (left to right) in UWIN-CM AO – UA (frequency difference, % per dBZ per m). The magenta lines denote 10-kilometer altitude, 20 and 40 dBZ. The black dotted contour indicates 0%. 131
- 5.2 Hovmoller diagrams of UWIN-CM AO (a) flight-level radar reflectivity with 30 dBZ contours (b) flight-level wind speed with 64 kt contoured (c) 0.5km moisture convergence, and (d) T100 with 26.5C contoured. RMW is overlaid in magenta on all diagrams. 134

## **Chapter 1: Introduction**

### **1.1 Motivation**

Intensity and intensity change remain one of the most significant challenges in tropical cyclone (TC) prediction. Hurricane Ophelia was a unique and impactful tropical cyclone during the record-breaking 2005 Atlantic hurricane season that clearly demonstrated the value of and need for progress in intensity prediction, which has been limited in recent decades (Rappaport et al. 2009). Ophelia oscillated between tropical storm and Category 1 hurricane intensity eight times during its life cycle and had an unusually slow and erratic track, during which time the storm was incorrectly forecast to make landfall in Florida, South Carolina, and North Carolina. Ophelia's intensity changes, as with those in any TC, result from complex storm-environment interactions and internal storm structure changes that are difficult to observe and model. These interactions and structure changes occur across multiple small time and spatial scales and have been under-observed, particularly in the high-wind regions of the hurricane boundary layer (HBL) and inner core. Insufficient and inherently imperfect observations in these regions of the hurricane environment translate into error in numerical models, both in the initial state of the atmosphere-ocean system and in the appropriate representation of the complex physical and dynamical processes involved in the interactions and structure changes (Marks & Shay 1998; Bender & Ginis 2000). Ophelia's utility in addressing the outstanding problem of TC intensity change prediction is two-fold. The storm's intensity changes were accompanied by substantial changes in storm structure, and these structure changes were well observed during the Hurricane Rainband and Intensity Change Experiment (RAINEX, Houze, et al. 2006; see also

Intensity Forecasting Experiment (IFEX), Rogers et al. 2006). In this study, we take advantage of the unprecedented airborne Doppler radar, GPS dropsonde, satellite, and buoy observations from RAINEX, and high-resolution coupled atmosphere-ocean modeling to address the impact of air-sea interaction on storm structure and its role in the dynamics of TC structure and intensity changes. Herein, we focus on the contribution of air-sea interaction to storm structure changes, particularly the observed collapse and recovery of Ophelia's inner core, and the subsequent intensity changes experienced by the storm in a complex atmosphere-ocean environment that included propagation over its TC-induced cold pool and the Gulf Stream.

## **1.2 Background and literature review**

### ***1.2.1 Air-sea interaction and tropical cyclone intensity***

Air-sea interaction has long been recognized as important to the energetics, and therefore the intensity of TCs. Early modeling studies identified the relationship between warm (cool) sea surface temperature (SST) and the formation and strengthening (weakening) of these storms (Palmen 1948; Fisher 1958; Perlroth 1969; Gray et al. 1975; Ooyama 1969; Rosenthal 1971). Malkus & Riehl (1960) and others built upon this SST-intensity change link by computing energy budgets to understand how energy is transformed by the TC, that is the conversion of latent heat energy into mechanical energy to accelerate tangential hurricane winds put forth by Riehl (1954). Malkus and Riehl found the degree of latent heat release at high  $\theta_e$  due to a strong oceanic heat source to be an ‘essential’ ingredient distinguishing tropical-storm and hurricane force TCs, demonstrating the role of the ocean as the primary source of heat and moisture opposing frictional dissipation both internal to the TC and at the air-sea interface. Using

results from a highly idealized nonlinear axisymmetric model, Emanuel (1986) put forth a comprehensive theory of air-sea interaction in TCs focused on the exclusive role of the ocean in supporting intense hurricanes at steady state, challenging the need for ambient conditional instability in the atmosphere (CISK, e.g. Charney & Eliassen 1964) inherent to prior numerical models initialized with moist tropical soundings (e.g. Jordan 1958). The model results from Emanuel suggested intense TCs would occur if warmer SST or colder upper tropospheric temperatures existed. Such condition would support more thermodynamic efficiency (defined as  $(T_B - T_{out})/T_B$ ), which the author directly relates to the minimum attainable central pressure. This minimum pressure is a metric of the maturity of the TC warm core, and is a function of both the surface moisture and turbulent exchange of moist entropy and angular momentum at the top of the hurricane boundary layer. A set of early numerical model simulations of the TC life cycle (Ooyama, 1969) prior produced only a weak TC without sea surface evaporation (i.e. air-sea heat fluxes) consistent with Emanuel's later theory, but also indicated that intensity is peculiarly sensitive to SST changes (Ooyama 1969; Anthes 1974).

The heat, moisture, and momentum fluxes that comprise air-sea interaction and are related to the intensity are communicated through the interface in direct contact with the planetary boundary layer (PBL; often denoted HBL in the context of hurricanes). Hurricane response to SST changes has been investigated in previous modeling studies which include a PBL, however, typically this PBL was a single layer of  $\sim 1$  km depth containing both the surface and boundary layer. In this setup, the boundary layer in a hurricane lacks detail, is misrepresented by having constant height, and TC-ocean interactions are not permitted. Anthes and Chang (1978) used an axisymmetric model

(see Anthes et al. (1971)) modified with the multi-layer PBL parameterization employed in Busch et al. (1976). This PBL contains a surface layer where the various fluxes are computed using Monin-Obukhov similarity theory, and a well-mixed layer with a capping inversion. The authors used this (9-layer total) model to investigate intensity response to SST changes (increase and decrease SST by 1°C, at model hour 96) and dynamic and thermodynamic coupling between model TCs and the ocean. In the two experiments, the model hurricane response had two stages: an adjustment of the HBL to the new ocean environment, and steady change of the model TC intensity thereafter ( $\sim 3 \text{ ms}^{-1}$ , at model hour 120). Two important findings emerged from this idealized work, firstly that an adjustment occurs within the HBL: increased (decreased) SST changes the thermal instability of the HBL which is reflected in increased (decreased) downward momentum transfer from above the HBL (latent heat energy conversion) and accelerated (decelerated) surface wind speed, which then steadies the response as surface friction increases (decreases) accordingly. Secondly, the small magnitude of the intensity change due to SST reflects the observation that TCs typically propagate beyond cooled ocean and over undisturbed regions quicker than the time necessary for a TC-ocean coupled response to the cooling to occur.

TC-induced upper ocean cooling, or more generally the ocean response to hurricane passage has been the subject of considerable previous investigations (Leipper 1967; Price 1981; Price et al. 1994; Shay et al. 1992) on the basis of ship-observed anomalous low SST regions in the wake of TCs (Fisher 1958; Jordan 1964). Both studies hypothesized modification of the ocean was induced by hurricane winds, either by vertical mixing or upwelling. Two studies on the upper ocean response to hurricanes

(Price 1981, 1994) would later reaffirm both these TC-forced ocean processes dominate over simple evaporation as the cause of ocean cooling beneath a hurricane. Liepper (1967) investigated in particular, the Gulf of Mexico before and after the passage of Hurricane Hilda (1964) via coordinated bathythermograph measurements over the region where strong winds occurred. Observed upper ocean temperature structure in the transects indicated warm ocean waters were transported away from the TC center, cooling and mixing in that process and SST cooled by more than 5°C over a region 70-200 mi<sup>2</sup>. This structure in the wake of Hilda provides evidence of wind-stress forced divergence of mass inducing upwelling (from ~60 m depth with Hilda), and horizontal turbulent mixing during the divergence of that mass away from the storm center. Buoy observations and three-dimensional numerical ocean model simulation of the ocean response to Hurricane Eloise (1975) were used to explore the physical mechanisms dominating the SST change and the influence of storm characteristics (e.g. translation speed) on the ocean response. Eloise passed over buoy EB-10 (in the north-central Gulf of Mexico) at 8.5 ms<sup>-1</sup>, well above the 5 ms<sup>-1</sup> 1949-2003 North Atlantic climatological mean found by Chen et al. (2006). The buoy observed SST decrease of 2°C was similar to the 3°C drop in the model results, and was 60 km right of the storm track. Entrainment of colder water was responsible for 85% of the irreversible flux into the mixed-layer (OML), while evaporation (exchange through the air-sea interface) composed the remaining 15%. Intense, slow-moving hurricanes produced the strongest SST response in the model TCs. The right of track bias is related to both the asymmetric wind stress and the asymmetry it induces in the OML velocity (stronger divergence of surface mass, stronger upwelling) and the superposition of surface wind velocity vector and

propagation vector. Overall the ocean response has been shown to derive from interaction between the TC surface winds and the upper ocean via wind-stress induced modification of OML velocities (e.g. upwelling, vertical mixing) and has strong dependence on the initial upper ocean structure (OML depth, thermocline gradient magnitude), propagation speed (e.g. strong ocean response for  $< 4 \text{ ms}^{-1}$  TC here), with weaker relationships between the ocean response and storm size (location of  $\frac{1}{2} U_{10 \text{ max}}$ ) and latitude location. More recent studies have incorporated our current understanding of TC energetics and air-sea interaction to challenge the criticality of the  $26^\circ\text{C}$  SST threshold with a notion of positive enthalpy flux conditions being more robust and useful a measure for TC intensity change favorability. Furthermore, this perspective supports the truly coupled relationship of atmosphere and ocean in intensity and intensity change.

Since Palmen (1948) first demonstrated the relationship between  $\text{SST} > 26^\circ\text{C}$  and hurricane formation, numerous other studies found a similar relationship between ocean surface temperature and the maintenance and intensification of TCs (e.g. Miller 1958; Perlboth 1967; Gray 1968; Dare & McBride 2011) and this threshold is oft-cited and interpreted as a critical value. Leipper & Volgenau (1972) used this threshold to compute upper ocean heat content, a diagnostic of thermal energy storage integrated from the sea surface to the depth of the  $26^\circ\text{C}$  isotherm, explicitly taking a negative value when SST is cooler than  $26^\circ\text{C}$ . Previous efforts to establish correlation between OHC and intensity changes have been met with mixed success (e.g. Shay et al. 2000; Hong et al. 2000; Price 2009) but the OHC only considers the ocean and the computed values have been found to exceed observed maximum enthalpy flux in the inner core of hurricanes by orders of magnitude (Cione & Uhlhorn 2003). Cione et al. (2013) and Cione (2015) used buoy

observations from the Tropical Cyclone Buoy Database (TCBD, Gilhousen 1987) from 62 TCs over 33 seasons to assess the variability and relative impact of near surface atmospheric ( $qa_{10m}$ ) and surface oceanic ( $qsst$ ) moisture contributions to latent heat flux. Results from this multi-hurricane study do reaffirm the observation by Palmen regarding hurricane formation and  $26^{\circ}\text{C}$  SST, however, this threshold is not found to be critical to their maintenance (15 of 245 TC cases at hurricane intensity despite  $SST < 26^{\circ}\text{C}$ ). The maximum observed inner-core surface dew point for all TC cases at any latitude was  $26.5^{\circ}\text{C}$ , hence when SST is greater than  $26^{\circ}\text{C}$  both  $\Delta T$  and  $\Delta q > 0$ . In other words, a positive enthalpy flux condition is guaranteed. By examining the thermodynamic structure from the buoy data, Cione et al. (2013) noted that although SST might be similar in the inner-core of strengthening and weakening TCs, intensifying TCs had  $\Delta q$  inner-core values 17-27% higher than those for weakening systems – possibly due to the transport of dry air via convective downdrafts. Vertical wind shear and ocean cooling were also addressed in this study as mechanisms for modifying  $\Delta q$ . Regardless of the mechanism and ignoring dynamic factors, small differences (e.g.  $\mathcal{O}(10^0)$  g kg $^{-1}$ ) in  $qsst$  or  $qa_{10m}$  can alter the moisture flux by 40-60% within  $6R/R_{max}$ . These studies recast traditional thinking that has overemphasized the value of SST when considering TC intensity and intensity change. Emanuel (1986) explicitly references the  $26^{\circ}\text{C}$  threshold in his concluding arguments, saying “the absence of TC development when sea water temperature is less than about  $26^{\circ}\text{C}$  is related to the circumstance that the depth of the conditionally neutral or unstable layer is *usually* too shallow... to allow a reasonable *thermodynamic efficiency*”. This statement addresses the inherently coupled nature of the atmosphere and ocean in TCs, and it is this awareness and communication that permit the

influence of both  $q_{SST}$  and  $qa_{10m}$  on the ‘positive enthalpy flux condition’ and ultimately TC intensity via air-sea interactions.

### ***1.2.2 Structure and intensity change via air-sea interaction***

Fundamental studies over the past fifty years have elucidated the origin and evolution of tropical cyclone rainband and inner-core structure (e.g. Malkus 1958; Shea & Gray 1973; Willoughby et al. 1982; Willoughby et al. 1984) and have established the crucial role of the ocean and air-sea interaction in providing the energy source and sink for TCs (e.g. Emanuel 1986; Rotunno & Emanuel 1987). Most previous air-sea interaction modeling studies have focused on the ocean impact on TC intensity (Schade & Emanuel 1999; Bender & Ginis 2000; Chan et al. 2001; Wu et al. 2007) without directly addressing how air-sea interaction affects the horizontal and vertical TC structure (i.e. precipitation, wind, temperature, moisture, pressure). Intensity change in tropical cyclones however, which remains an outstanding problem in TC prediction, is associated with both complex storm-environment interactions (i.e. vertical wind shear, environmental mean flow, dry air entrainment, etc.) *and* internal structure changes (Black et al. 2002; Rogers et al. 2003; Chen et al. 2006; Peng et al. 1999; Dunion & Velden 2004; Camp & Montgomery 2001). The Intensity Forecasting Experiment (IFEX, Rogers et al. 2006) initiated in 2005 and ongoing today has sought to address the slacking gains in TC model intensity prediction relative to track in recent decades. IFEX outlines 3 causes for the limited progress: 1) deficient real-time observations of structure and intensity from inner-core data, 2) numerical model limitations (i.e. resolution, representation of vortex and physical processes), and 3) gaps in our understanding of air-sea interaction and TC physical processes. At its inception, IFEX was supporting the

development of the now-operational coupled atmosphere-ocean Hurricane Weather Research and Forecasting model (HWRF, Surgi et al. 2006) and hence proceeded with three goals: collect observations throughout the TC life cycle in various environments, develop and improve measurement technologies for real-time observations of structure, intensity, and the environment, and improve understanding of the physical processes important to intensity change for all stages of the TC life cycle. The Hurricane Rainband and Intensity Change Experiment (RAINEX, Houze et al. 2006) was one of several field campaigns associated with IFEX. RAINEX was conceived to address internal structure changes and dynamics of the eyewall-rainband interactions linked to intensity changes (see Willoughby et al. 1984, Willoughby 1988). RAINEX was planned for August – September 2005 and observed three hurricanes in range of aircraft stationed in Florida at that time: Katrina, Rita, and Ophelia. Flight missions were coordinated for simultaneous observation of eye, eyewall, and rainband structures based on high-resolution numerical model forecasts conducted at the RAINEX Operations Center (ROC) at the University of Miami Rosenstiel School (RSMAS) using the 5<sup>th</sup> Generation Penn State/NCAR Mesoscale Model (MM5, Grell et al. 1994; Dudhia 1993). RAINEX was and is to date the only campaign to include 3 Doppler radar equipped aircraft (2 NOAA WP-3D (N42, N43), 1 NRL WP-3D). The NRL WP-3D was equipped with dual-beam Electra Doppler Radar (ELDORA; Hildebrand et al. 1996) capable of 0.4-km horizontal sampling resolution. Additionally, numerous GPS dropsondes (462 in Ophelia) were deployed from the NOAA WP-3D and NOAA Gulfstream-IV (G-IV, N49) aircraft to sample the boundary layer structure in the eye, inner-core, and outer environment. The extent of data gathered during RAINEX helps satisfy both the IFEX objectives and the objectives for

this work by having captured complex structure and intensity change in Hurricane Ophelia.

Several programs over the past fifteen years have provided excellent observations of air-sea interaction and TC structure (e.g. Coupled Boundary Layer Air-Sea Transfer (CBLAST)-Hurricane, Chen et al. 2007; RAINEX, Houze et al. 2006; Impact of Typhoons on the Ocean in the Pacific (ITOP), D'Asaro et al. 2014). With these programs providing much-needed observations and advancements in computer resources and model resolution, recent air-sea coupling modeling studies have shown air-sea interaction impacts both structure and intensity (Lee & Chen 2012; Lee & Chen 2014; Chen et al. 2013). Prior studies discussed in the previous section have demonstrated inclusion of high-resolution, detailed planetary boundary layer structure is important to TC energetics and to understanding how air-sea interaction impacts intensity (Emanuel 1986; Anthes & Chang 1978). It is through this PBL/HBL that air-sea flux is communicated from the ocean to the atmosphere, and how moist entropy and momentum are exchanged at the top of that layer in accordance with the heat and kinetic energy budget of the TC, particularly in the inner core. Lee and Chen (2012) investigated how air-sea interaction connects the upper ocean with storm structure through this important hurricane boundary layer using WP-3D aircraft radar and GPS dropsonde observations of Hurricane Frances (2004), which induced a strong cold wake and experienced structure changes. High-resolution numerical model simulations were conducted to analyze how the HBL structure responds to changes in surface winds and air-sea flux associated with the CBLAST observed structure changes. The authors found awareness of storm-induced cooling in the model TC due to air-sea coupling produced a weaker storm (compared to uncoupled

atmosphere-only) due to air-sea enthalpy flux reduction over the cold wake. HBL asymmetry as determined by model comparison to GPS dropsonde profiles of  $\theta_v$  and  $\theta_e$  was in better agreement between the coupled TCs and observations. This finding reaffirms interaction with the ocean (and presence of the cold wake) elicits a response in the HBL, which changes structurally as it adjusts to the new SST as described in Anthes and Chang (1978). A companion paper by Chen et al. (2013) presented related results pertaining to observations and air-sea coupled modeling of Hurricane Frances during CBLAST-Hurricane, specifically the impact of a new directional wind-wave coupling method on representation of model TC surface winds and capturing the structure changes associated with Frances' eyewall-replacement cycle. Air-sea coupling to wind and waves was found to capture the ‘double-eyewall’ and moat structures associated with TCs undergoing EWRC best, which the authors hypothesize is related to the representation of  $C_D$  and  $C_K$  air-sea momentum/drag and enthalpy flux transfer coefficients as a function of wind speed (as well as the coupling of wind and wave direction) yielding a better estimate of the observed surface winds. As EWRC features a horizontal secondary wind maximum (SHWM; Samsbury & Zipser 1995) with an associated ring of convection, coupling was again found to be necessary to model the structure changes associated with air-sea interaction. Additionally, this air-sea interaction has an impact in the inner-core (surface wind representation, surface stress estimation) and away from the storm center where the coupling influences inflow angles (moisture convergence/advection) into the HBL that is important to the TC evolution and structure.

These two studies have shown the need for full coupling in numerical models, both in permitting realistic HBL adjustment to a changing ocean (i.e. asymmetric HBL

structure due to the cold wake of Frances) and appropriate estimation of dynamic and thermodynamic processes (i.e. TC-ocean feedback constrained air-sea fluxes, surface wind representation, inflow angle) linked to specific structure and intensity changes (Frances' EWRC). Lee and Chen (2014) added to these by investigating the physical processes involved in structure and intensity changes associated with Typhoon Choi-Wan (2009), specifically changes in structure of the HBL and convection due to Choi-Wan's interaction with its induced cold wake (cools by  $> 3^{\circ}\text{C}$ ). Coupled atmosphere-ocean model results show a stable boundary layer (SBL) forms over the cold wake in the right-rear quadrant. Convection is subsequently weaker and shallower above and azimuthally downstream of the wake. The SBL also was found to constrain air parcels within itself, preventing parcels over and downstream of the wake from rising into rainbands. Reduced surface wind speeds result radial force imbalance in the SBL region that enhances eyewall inflow and offsets reduced enthalpy flux over and downstream of the cold wake itself. Trajectory analysis of BL air parcels compared between coupled (AO) and uncoupled (UA) model simulations revealed the initial mean  $\theta_e$  for near-surface air entering the eyewall from the SBL was 358K ( $\sim 2\text{K}$  lower than UA). Once these parcels were over warmer water,  $\theta_e$  was found to increase to  $> 365\text{K}$  before rising into the eyewall convection. Advection of lower- $\theta_e$  air possessing less moisture beneath the eyewall likely enhanced local enthalpy flux there, supporting the contribution of both near-surface atmosphere and near-surface ocean (via  $\Delta q$  as opposed simply to SST) to enthalpy flux and more generally the truly coupled nature of the atmosphere-ocean system as it pertains to TCs (see Cione, 2015). Although this recent study is specific to a particular TC, the interaction between the TC and cold wake resulted in an initial

modification to the HBL, change in the intensity and structure of convection, and weakened surface winds that corroborate findings in previous work. Furthermore, Choi-Wan demonstrates the complexity of the air-sea interactions, their consequences for TC structure and intensity, and the need for full air-sea coupling in numerical models.

Historic and recent observational and modeling studies have investigated TC energetics, intensity, intensity change, and structure change in the context of air-sea interaction. Specific storm parameters have not been explicitly targeted in previous work seeking to improve understanding of air-sea interaction processes broadly, with more emphasis being placed on appropriate coupling, physical representation of processes in models and so forth. Hurricane Ophelia however, was slow moving and the size of its wind field ranged from typical to unusually large following the inner core collapse alluded to in Chapter 1.1. A recent study by Halliwell, et al. (2015) used an idealized version of the pre-2013 HWRF model with 27-km parent and 9 and 3 km inner nests coupled to a uniform ocean with no land to study the isolated impact of ocean cooling on TC intensity as a function of storm parameters including propagation speed and size. This storm size reflects the TC structure as defined by the extent and distribution of surface winds, which hence are a vehicle for air-sea interaction important to both induced ocean cooling and air-sea enthalpy flux. Results from the experiments show large and slower-moving storms are more sensitive to the ocean, as well as ocean regions with thin warm layers or less upper ocean heat potential. This study is mentioned in the context of Ophelia's large wind field to emphasize the impact this larger (though weaker) storm had on the ocean following its expansion, and to suggest that the dependence of air-sea enthalpy flux and TC-ocean feedback on TC surface winds is particularly relevant and

intriguing when this storm is larger in the context of structure change, intensity change, and vortex resilience due to air-sea interaction.

### ***1.2.3 Hurricane Ophelia***

Ophelia was a long-lived tropical cyclone best known for having an erratic track and an atypically slow forward speed for much of its lifetime. Though the storm was far less costly than Katrina or Rita by damage (\$70 million, 2005 USD), costly preparation by government and emergency response agencies particularly in North Carolina prior to Ophelia's closest approach to land on September 14 proved largely unnecessary when the storm failed to make landfall and the strongest winds remained offshore. Figure 1.1a shows the observed best track from the National Hurricane Center.

Ophelia formed from a non-tropical low associated with a cold front that stalled within a broad low-pressure area between Florida and Bermuda over the subtropical northwest Atlantic. By 0600 UTC September 6, the pre-Ophelia low acquired a closed surface circulation and became Tropical Depression Sixteen (TD 16) between Grand Bahama and Andros Island. GOES-12 visible satellite with overlaid TRMM PR rain rate observations show TD 16 was composed of several mesoscale convective clusters adjacent to broader stratiform precipitation that consolidated and gradually organized while moving north parallel to the Florida coast September 6. The inner core of the cyclone became more well-defined early on September 7, and TD 16 strengthened into Tropical Storm Ophelia about 165 kilometers east of Cape Canaveral. The intensity evolution for Ophelia is shown in Figure 1.1b.

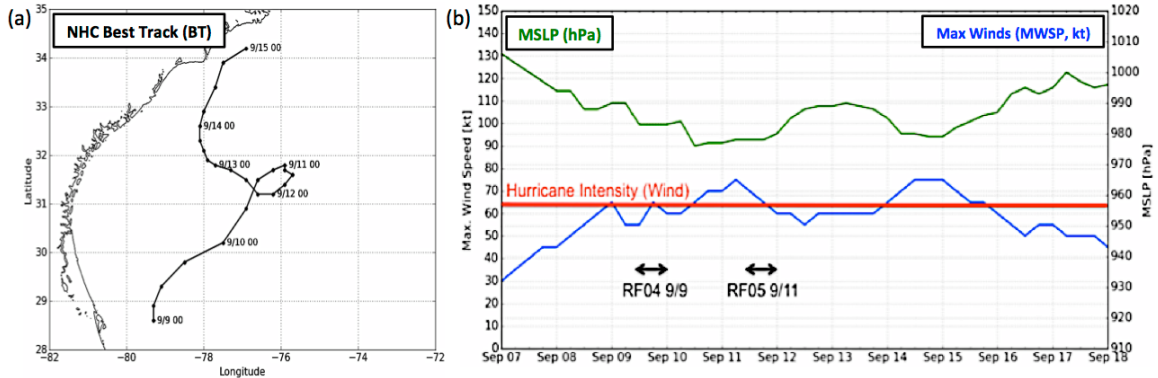


Figure 1.1 Ophelia’s NHC best-track (a) 6-hourly positions and (b) intensity given by maximum sustained winds (kt) and minimum sea-level pressure (hPa). Black arrows indicate the two RAINEX flight missions (RF04 and RF05) during which Ophelia was a tropical cyclone.

After becoming a tropical storm, Ophelia remained embedded within the broad ‘parent’ trough that included tropical cyclones Maria and Nate, and the tropospheric steering flow was extremely weak (Chen et al., 2006). Model track forecasts were split between two possibilities for Ophelia at this time. GFDL<sup>1</sup> and ECMWF<sup>2</sup> predicted a westward turn and landfall in Florida, however most global models were forecasting the storm to remain offshore of Florida and execute a clockwise loop. Favoring the first model solution though with low confidence, NHC chose to initiate tropical storm watches and warnings for the northeast Florida coast. Ophelia validated the second set of guidance and briefly strengthened to a hurricane by 0000 UTC September 9.

Ophelia remained structurally asymmetric throughout much of September 9, with the strongest convection observed during RAINEX RF04 displaced north and west of the storm center. Upper-level winds were unfavorable over the eastern half of the storm due to moderate (6–13 m/s, 200 – 850 hPa layer) south-southwesterly shear from an upper-

<sup>1</sup> Princeton Geophysical Fluid Dynamics Laboratory global forecast model

<sup>2</sup> European Centre for Medium-Range Weather Forecasting global forecast model

level trough centered over northern Quebec. At the same time, Ophelia was passing over relatively moderate sea surface temperatures (SST) of 27-28°C while drifting northward parallel to the Gulf Stream. Though it possessed an asymmetric structure due to shear, Ophelia remained within 10-kt of hurricane intensity throughout the day. Substantial intensity change was likely inhibited by the combination of (relatively weak) shear and warm (enough) upper ocean conditions beneath the storm. Similar stagnation of intensity change due to ‘offsetting’ of shear and SST has been previously observed (e.g. Hurricane Jimena (1991); Black et al. (2002)).

On September 10, Ophelia briefly accelerated northeastward accompanying a passing mid-tropospheric trough over the southeastern U.S. and was expected to intensify with decreasing shear and warmer SST over an eastern portion of the Gulf Stream. By 1800 UTC September 10, the storm intensified to Category 1 hurricane status and a second RAINEX flight (RF05) was organized for September 11. Numerical model guidance from the high-resolution NCAR Mesoscale Model Version 5 (MM5) predicted changes in Ophelia’s structure towards the afternoon and evening of September 11, namely a collapse of the inner core convection and counterclockwise azimuthal propagation of rainband convection wrapping around the center. Figure 1.2 shows GOES-12 infrared satellite snapshots from September 11 1115, 1845, and 2145 UTC and MM5 rain rate forecasts near the same time captured azimuthal propagation of convection and asymmetry in the precipitation structure associated with inner core collapse. This structure change occurred while Ophelia executed a broad anticyclonic loop between 1800 UTC September 10 and 0600 UTC September 12.

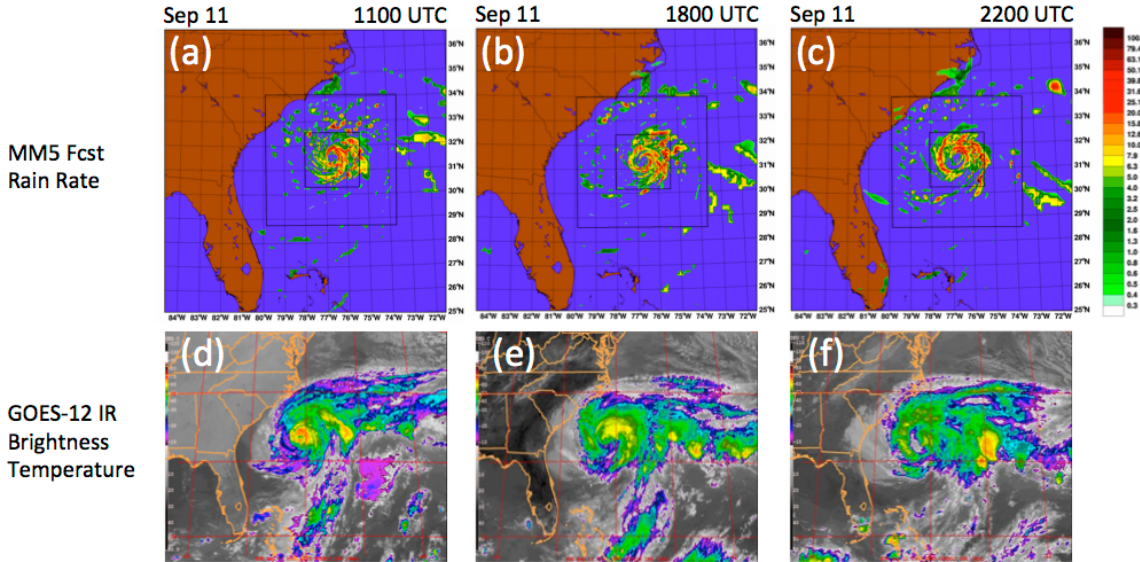


Figure 1.2 NCAR/Penn-State 5<sup>th</sup>-Generation Mesoscale Model (MM5) forecast rain rate (mm/hr) verified against GOES-12 infrared satellite brightness temperature imagery for (a,d) September 11 1100 UTC (b,e) September 11 1800 UTC, and (c,f) September 11 2200 UTC.

Moving slowly, Ophelia induced strong upper-ocean cooling beneath its circulation that remained near the storm's inner core. The upwelling and mixing cooled and thinned the ocean mixed layer (OML), decreasing SST near the storm by 2-3°C and coincided with Ophelia's longest period of weakening (from 70 to 55 knots). Progressive collapse of Ophelia's inner core precipitation is shown by TRMM TMI 85 GHz vertical polarization brightness temperature images from September 11 1510, 1648, and 1826 UTC in Figure 1.3. At the 85 GHz frequency, cold brightness temperatures denote strong convection.

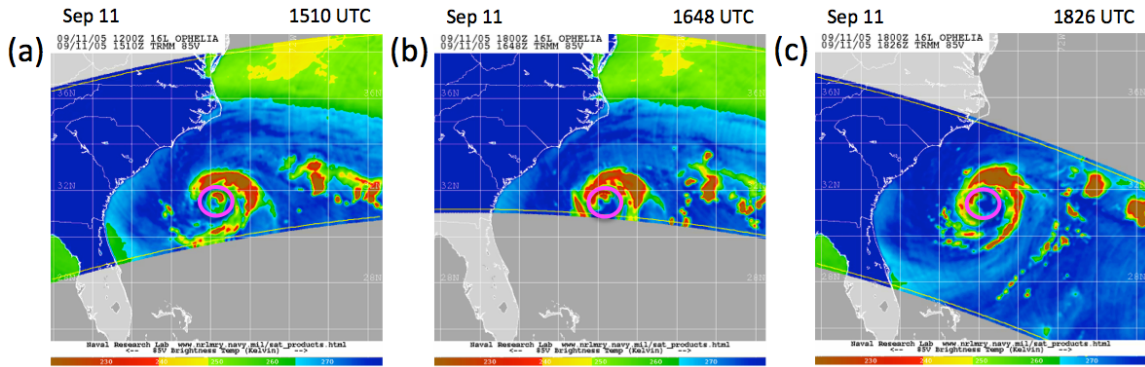


Figure 1.3 TRMM PR 85 GHz vertical polarization microwave brightness temperature (degrees Kelvin) for September 11 (a) 1510 (b) 1648, and (c) 1826 UTC. The magenta circle is roughly situated about the storm center.

Ophelia began a turn towards the west by 0600 UTC September 12, slowly moving away from its induced cold pool and towards a warmer region of the Gulf Stream near the coast of North Carolina. Now a tropical storm<sup>3</sup>, the strongest precipitation had expanded outward to greater than 75-kilometers from the center and the eye was almost completely vacant of precipitation. The strong outer rainband was discrete and convective, but radially narrow, with a nearby weaker rainband that was more stratiform in nature. Moving slowly northwestward, Ophelia's radius of maximum winds was large but did not encompass the intense convection of its outer rainband while approaching the Gulf Stream on September 12 and 13. At the same time, 24 – 26°C SST from Ophelia's cold pool expanded further west trailing behind the storm. Consequently, Ophelia's intensity remained nearly constant but below hurricane strength for the 36 hours following 0600 UTC September 12. Ahead of the storm, the discrete outer rainband

---

<sup>3</sup> NHC best track indicates a maximum sustained wind of 60 kt (tropical storm) at September 12 0600 UTC, while aircraft reconnaissance derived intensity gives the intensity as 65 kt (Category 1 hurricane).

began to reorganize and broaden slightly as it encountered 28-29°C SST at the periphery of the Gulf Stream.

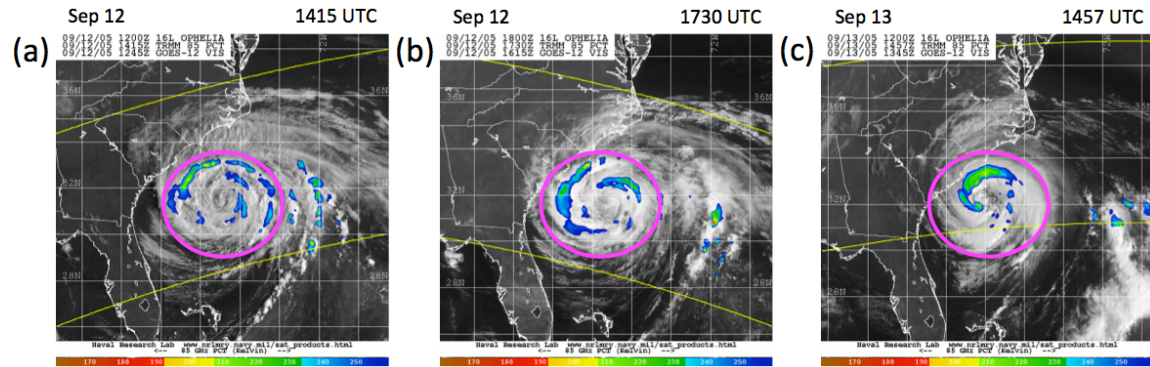


Figure 1.4 TRMM PR 85 GHz polarization corrected (PCT) microwave brightness temperature (degrees Kelvin) for September 12 (a) 1415 (b) 1730, and September 13 (c) 1457 UTC. The magenta circle is sized according to the convective outer rainband in (a), and is the same size and position in (b) and (c), to show propagation and consolidation of convection during the recovery of Ophelia's inner core.

By the final NHC advisory of September 12, model forecasts were in agreement that a ridge of high-pressure northwest of Ophelia would begin to diminish, and the storm would turn north towards the North Carolina coast roughly parallel with the Gulf Stream. Ophelia remained near hurricane intensity through the morning of September 13, though forecasters noted ‘it would take very little’ for Ophelia to reach hurricane status. Tropical storm warning, hurricane watch, and hurricane warning advisories had been issued extending from Charleston, SC through the North Carolina Outer Banks. Landfall was projected near Morehead City during the evening of September 14

Ophelia regained hurricane status over the Gulf Stream September 13 1800 UTC, while 110 miles (177 km) south of Wilmington, NC. The storm’s hurricane force winds extended outward 80 kilometers from the storm center, but the RMW would enter a period of contraction leading up to the projected landfall time about 24 hours later. Over

the preceding 6 hours, Ophelia's inner-core was situated over  $\sim 27\text{-}28^{\circ}\text{C}$  SST, and convection had become more organized and symmetric. The RMW and radius of maximum convection had nearly aligned (both about 50-kilometers from the storm center). Figure 1.5 shows the precipitation and wind maxima and the improved symmetry about a small, clear eye as observed from NASA AQUA-1 satellite and QuikSCAT scatterometer winds the afternoon of September 13. The southwest rainband would wrap further around the center to complete the eyewall and a clear moat would form between the eyewall and rainband by 2300 UTC.

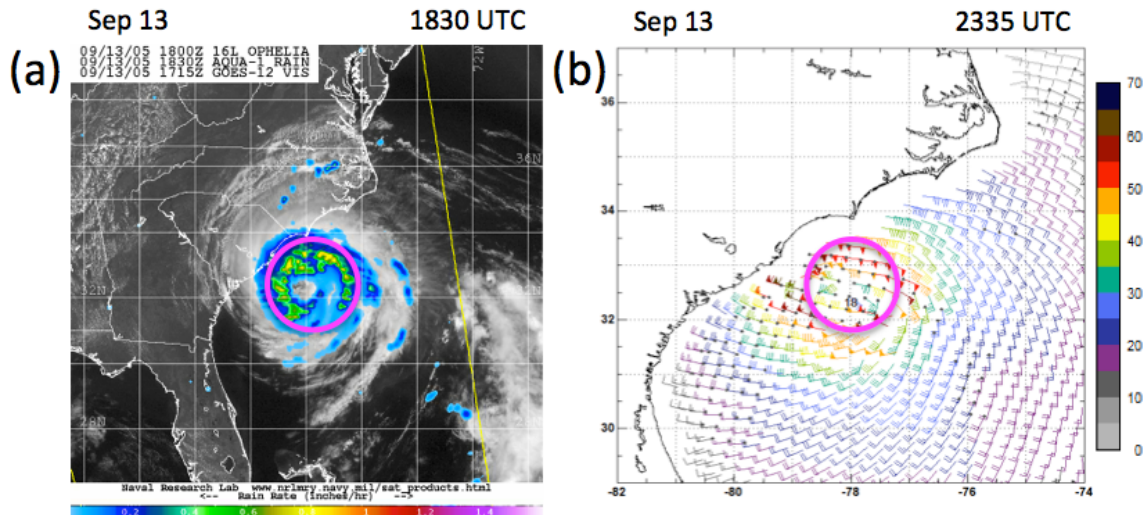


Figure 1.5 NASA AQUA-1 AMSR-E (a) 85 GHz PCT (degrees Kelvin) and (b) QuikSCAT Version 4 near-surface winds (knots) late on September 13. The magenta circle is situated at the outer radial edge of the strongest rain in (a), and is located at the same position and size in (b), to show the similar location of heavy rain and strong winds.

By the evening of September 14, Ophelia's northwest eyewall had passed within 90-kilometers of Cape Fear but the storm's center remained to the east-southeast without making landfall. Ophelia continued to slowly push eastward parallel to the North Carolina coast throughout the day September 15. Finally, a strong shortwave trough over the Great Lakes pushing eastward combined with a subtropical ridge to the south

provided large-scale steering to dislodge Ophelia on September 16. The storm accelerated toward New England and the Canadian Maritimes, becoming post-tropical on September 18. The NHC issued its final advisory on Ophelia south of Nova Scotia 0000 UTC September 18.

### **1.3 Science objectives**

Air-sea interaction has been shown to impact *both* TC structure *and* intensity in recent studies, but remains an elusive challenge for the prediction community even in fully coupled models. Since air-sea interaction may be critically important to structure and intensity changes in Hurricane Ophelia, this study will make use of a fully-coupled atmosphere-ocean model and unprecedented, multi-platform observations from RAINEX to address the following questions

- What are the key factors affecting Hurricane Ophelia's structure and intensity?
- How does air-sea coupling contribute to storm structure change that affects Ophelia's intensity in a complex TC environment?

## **Chapter 2: Model Description and Analysis Methodology**

### **2.1 The numerical model**

The numerical model used in this study is the Unified Wave Interface Coupled Model (UWIN-CM, Curcic 2015). UWIN-CM consists of two separable model components capable of instantaneous, full coupling using the Earth System Modeling Framework (ESMF, Hill et al. 2004). For the atmosphere, UWIN-CM uses the Weather Research and Forecasting (WRF, Skamarock & Klemp 2007) model version 3.7.1. WRF uses three nested domains of 12, 4, and 1.33-kilometer grid spacing. To capture Ophelia's lifecycle over an extended period while resolving the inner-core structure, a vortex-following nested grid developed by Chen and Tenerelli (2001) is used in the inner two domains. Domain size for the two inner nests is 157x157 and 301x301, respectively. We use 44  $\eta$ -coordinate vertical levels to adequately capture the storm structure, particularly in the boundary layer and low-level free troposphere.

The ocean model used in UWIN-CM is the Hybrid Coordinate Ocean Model (HYCOM, Wallcraft et al. 2009), version 2.2.98. A single fixed 1380x980 domain is used, with 4-kilometer horizontal grid spacing and 32 vertical levels. HYCOM is three-dimensional, hydrostatic, and uses three vertical coordinate systems. In open, stratified ocean isopycnal (constant density) surfaces are used for the vertical levels. For shallow coastal regions, vertical levels are  $\sigma$ /terrain-following. Finally, in the mixed-layer and other unstratified ocean, the vertical coordinate is depth (z).

UWIN-CM couples to the ocean using the ESMF, passing information between atmosphere and ocean on a common exchange grid. Coupling physics are handled using this framework and the common grid permits calculation of air-sea exchange (e.g. surface

fluxes). When implementing atmosphere and ocean domains together, WRF passes radiative transfer, heat flux, and precipitation rate to HYCOM while HYCOM passes SST to the atmosphere. Figure 2.1 shows an overview of the UWIN-CM domains.

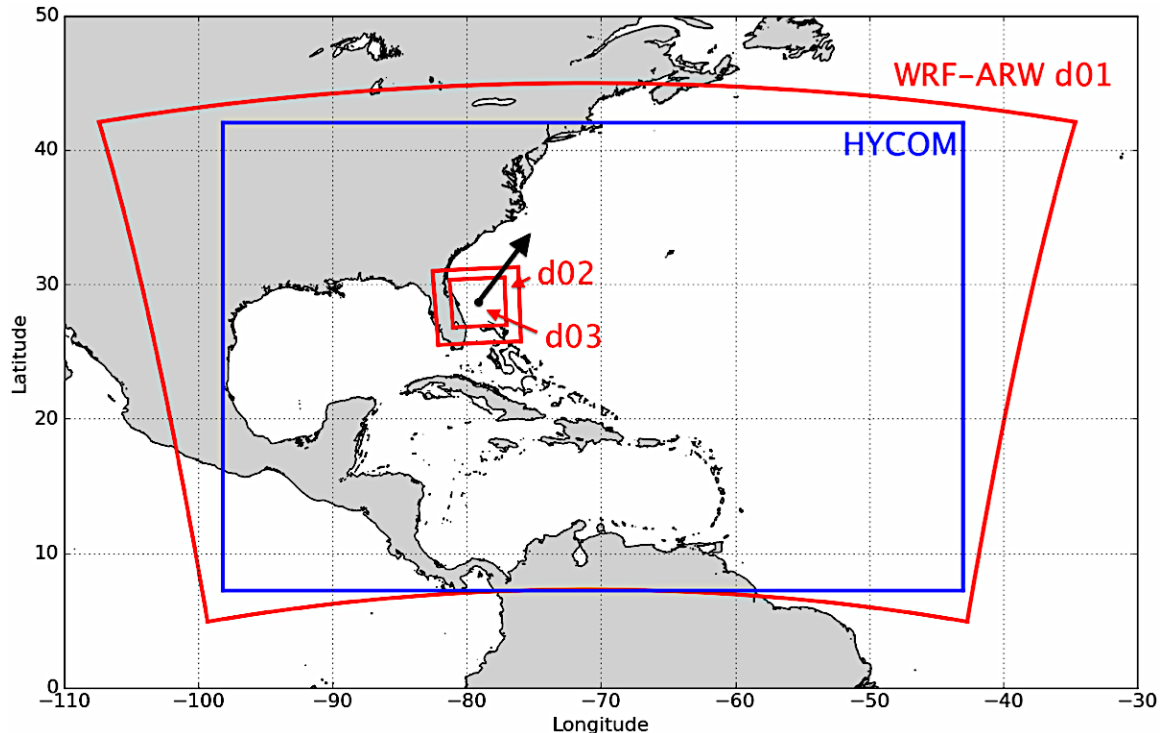


Figure 2.1 Schematic diagram of the UWIN-CM atmosphere and ocean component domains for Hurricane Ophelia.

UWIN-CM and its immediate predecessor, the University of Miami Coupled Model (UMCM) have been used to simulate several hurricanes in recent studies, most recently in work on ocean surface wave prediction in Hurricanes Ike and Sandy (Chen & Curcic 2016). Other studies have included model results for Hurricanes Bonnie (1998, Rogers et al. 2003), Georges (1998, Cangialosi & Chen 2004), Frances (2004, CBLAST-Hurricane, Chen et al. 2013) and Isaac (2008, Curcic et al. 2016). These studies have shown high-resolution, less than 2-kilometer grid spacing is critical to resolving inner core structure, and important to reproducing verifiable tropical cyclone evolution.

All model experiments in this study use the WRF Single-Moment (WSM) 6-class microphysics scheme, Rapid Radiative Transfer Model 2.1 (RRTMG) for radiation, and the Yonsei University (YSU, Hong et al. 2006) scheme for the planetary boundary layer physics. Convection is explicitly resolved on the inner two WRF nested grids, and parameterized on the parent 12-kilometer grid with the Kain-Fritsch cumulus scheme (Kain & Fritsch 1993).

Two UWIN-CM configurations are used in this study, uncoupled atmosphere-only (UA) and fully coupled atmosphere-ocean (AO). The control experiment uses the UA configuration, holding SST constant and prohibiting ocean evolution. In the fully coupled experiment, air-sea interaction is permitted between the atmosphere and a three-dimensional, evolving ocean. Both experiments were run for 144 model hours, September 9 0000 – September 15 0000 UTC. This period allows Ophelia to spin-up and captures the cold-wake and Gulf Stream interactions. The WRF component uses 6-hourly  $0.5^\circ$  National Center for Environmental Prediction (NCEP) final analysis (FNL) fields for the initial and boundary conditions. Model wind fields are modified with 0.003 coefficient nudging for the parent domain only. HYCOM uses  $0.08^\circ$  daily HYCOM global analysis fields for the initial and lateral boundary conditions. Model output from both experiments was vertically interpolated from the native WRF  $\eta$ -level grid to pressure and height levels using the NCEP Unified Post Processor (UPP), version 2.0.

## 2.2 Analysis methodology

Raw and post-processed model outputs were used to verify the simulated TCs against RAINEX and NHC observations, and analysis was performed to clarify the impact of ocean coupling and the role of air-sea interaction on Ophelia's structure and intensity. A storm-relative coordinate framework is conventionally the most appropriate spatial reference system for tropical cyclones, however model simulated storm tracks for Ophelia were quite sensitive during the anticyclonic loop and had difficulty maintaining a sufficiently steady heading. To account for this, we performed analysis using both Cartesian and storm-relative frameworks. For the storm-relative coordinate transformation, the model storm heading is calculated using the center position of the storm 3 hours prior and after the desired time. Using this heading, the data or variables are recast by rotation of the axis such that the storm's direction aligns with due north. Furthermore, model analyses provide a reference to the storm center in radius-azimuth space either in distance from storm center or with respect to multiples of the radius of maximum wind (RMW). Structural features identified or described in the analyses refer to either storm-relative quadrants (forward-left, forward-right, etc.) or cardinal sector (northwest, southeast, etc.) based on the type of coordinate framework employed.

### 2.2.1 Track and intensity verification

Model storm track, maximum sustained wind speed (MWSP), and minimum sea-level pressure (MSLP) are verified against NHC best track observations for the entire model period, September 9 – 15 0000 UTC. Model center position and intensity were computed from raw WRF output using a vortex-tracking algorithm developed by Chia-Ying Lee. The storm center is derived from the 850-hPa geopotential height minimum,

similar to the procedure used in the vortex-tracker routine of the vortex-following moving nest infrastructure developed by Tenerelli et al. (2001). MWSP is calculated using 10-meter winds, and MSLP is calculated using the surface pressure. Best track and model positions and intensities are given for each hour.

### ***2.2.2 Storm-relative flight-level and vertical transects***

Storm precipitation, vortex, and upper ocean structure were analyzed in two axis dimensions in this study, horizontally and vertically. RAINEX observations of horizontal radar reflectivity and horizontal winds reflected the altitude of the aircraft at the time of interest, which was typically near 3-kilometers. Post-processed WRF output of radar reflectivity and wind were used to create horizontal maps of the model TC structure evolution using this 3-kilometer flight-level approximation, with black circles showing radial distance from the storm center every 50-kilometers. Vertical transects were also produced, in the cross-track (west to east storm-relative) and along-track (south to north storm-relative) directions spanning 200-kilometers on either side of the storm center. Transect indices were determined using the nearest value for each in a series of linearly interpolated points between the ends of the line. Radar reflectivity transects include black contours of 20 (thin) and 40 (thick) dBZ to denote the location and vertical depth of moderate and intense convection. Wind transects include black contours denoting tropical storm force (34 kt, thin) and hurricane force (64 kt, thick) wind speeds.

HYCOM output archive files were post-processed for analysis of the sea surface temperature and upper ocean evolution. The post-processed output contains water temperature at 0-meters and from 0-1000 meters in successively coarser increments with depth. Sea surface temperature maps were created from the 0-meter water temperature

field, and include a black contour at  $26.5^{\circ}\text{C}$ . White areas denote land. Vertical transects of the upper ocean were constructed in a similar way to reflectivity, using the water temperature field between 0 and 200 meters depth. A magenta contour is overlaid on each transect to denote the along-transect mixed layer thickness (MLT, in meters) from the MLT output field. Where bathymetry is present, it is shaded in dark grey.

### ***2.2.3 Earth-relative spatial maps***

Spatial maps were constructed to supplement the storm-relative analyses that were affected by sensitivity in the model TC storm headings, particularly during the anti-cyclonic loop period. Maps were created for 3-kilometer radar reflectivity (dBZ), surface winds (kt), SST (degrees C), 0-100m averaged temperature (T100, degrees C), and surface ocean currents (cm/s). Each map spans  $27\text{-}35^{\circ}\text{N}$  and  $72\text{-}82^{\circ}\text{W}$ , encompassing the entire storm track for both simulations. The thick black line shows the model storm track from the initialization time (0000 UTC September 9) to the current time. The black arrow points in the direction the storm is moving (the heading), and the black circle indicates 200 km from storm center. A time-series comparing model and NHC best track maximum winds (MWSP, kt) accompanies spatial maps where needed to connect the storm and ocean structure evolution in the model back to observations. Model MWSP prior and at each model hour is shown in the dark blue (UA) and red (AO) lines. Best track MWSP interpolated to hourly values is shown with the black line. The vertical line indicates the current time, while the faded lines right of that line denote the future intensities.

#### ***2.2.4 Azimuthal average analyses***

Azimuthal averages were computed as profiles and 2D maps to comprehensively describe the evolution of the model TC environment and storm structure. Each azimuthal average quantity has along radius separation related to the model grid resolution of the domain (2km for d03, 4km for d02). Azimuthal averaged profiles were constructed for flight-level reflectivity, surface wind speed, specific humidity at SST ( $q_{SST}$ ), specific humidity at 10-meter height ( $qa10$ ), equivalent potential temperature ( $\theta_e$ ), and T100. Quadrant-specific azimuthal averaging was performed to show variations in radar reflectivity (and RMR), winds (and RMW), moisture disequilibrium components ( $q_{SST}$ ,  $qa10$ ), and equivalent potential temperature in different regions of the storm. 2D azimuthal average radius-height diagrams were created for radar reflectivity and wind speed for 0 – 18 km altitudes at 0.5 km intervals between 0 and 200 km from storm center. These are compared to composited observations from the RAINEX aircraft. For timeseries using azimuthal average quantities, radial distances every 50km from 0 to 200km are used to distinguish how the field evolves over the entire TC at distances near and far from storm center.

#### ***2.2.5 Model simulated buoy verification***

Buoy observations (NDBC 41002 and 41010) were compared to model output using a storm track relative analysis of SST and surface pressure. A simulated buoy position for the model fields was determined from the model track relative to the difference between the best track and the actual buoy. The nearest point to the simulated buoy position was used for verification. Two time-series were constructed using the observed and model data, one of 0.6-meter water temperature versus model SST and the

other of observed versus model surface pressure. Due to the storm relative framework, analyses are most useful September 9 0000 – 1800 UTC for 41010 and September 10 1800 - September 12 0600 UTC for 41002.

### **2.2.6 Timeseries and Hovmöller diagrams**

While maps and transects serve as effective analyses for understanding what (and in what way) structure and intensity changes occur in the model TCs, timeseries permit us to examine the relationship between enthalpy flux modification facilitated by air-sea interaction and the timing of the structure and intensity change. Model timeseries were chosen based on observed air-sea interactions and structure and intensity changes in the real Ophelia, subdivided into four stages of the storm's life between September 9 and 15 (see Chapter 3): an organizing stage, upwelling/cold-pool interaction stage during which the inner-core collapse occurs, the expansion of the storm at near-steady intensity, and the recovery stage of the storm while over the Gulf Stream. Latent heat flux, moisture disequilibrium, surface wind, and integrated kinetic energy (IKE) timeseries were created and compared against the storm intensity (MWSP) and size (RMW) at each model hour. To understand air-sea enthalpy flux changes relative to Ophelia's circulation size, we also created difference timeseries to show the evolution of latent flux and its components (i.e.  $\Delta q$ , surface wind speed) between 50 and 100 km from storm center. Additionally, 2D time-radius Hovmoller diagrams are presented in Chapter 5, to provide a summary of changes in TC structure (precipitation, wind), upper ocean environment, and surface moisture convergence relative to the RMW.

### ***2.2.7 Contoured-frequency by altitude diagrams***

Summary analyses of the vertical structure of model precipitation were provided by contoured-frequency by altitude diagrams (CFAD, Yuter and Houze, 1995b). Post-processed WRF radar reflectivity was vertically interpolated between 0 and 16 kilometers at 0.5-kilometer intervals. At each level, reflectivity values are binned into 9 bins from 0.25-40 dBZ. Two-dimensional histograms of reflectivity against altitude are created from the vertical stacking of each level's reflectivity distribution normalized by the number of values at that level. The shape, slope and magnitude of the frequencies describe the maturity, depth, precipitation features, and the vigor of vertical motions in the model storm akin to the observational CFADs. Model CFADs from four time periods were composited to create grouped CFADs like those constructed from observations.

Since model radar reflectivity has values at all vertical levels and the model precipitation is biased high (even in the coupled TC), we took the difference of the grouped CFADs ( $\text{AO} - \text{UA}$ ) in separate analyses to distinguish more clearly between the distributions and highlight the changing regions of precipitation structure, intensity, and frequency in the two model TCs. These grouped analyses showed the vertical structure evolution in the organizing, cold-pool interaction, expansion, and Gulf Stream recovery periods in a quantitative and representative way.

### ***2.2.8 Summary***

Model analyses focused on 1) evaluating the effects of storm coupling to a fully interactive ocean, and 2) air-sea enthalpy flux modification via TC-atmosphere-ocean interactions and its implications for Hurricane Ophelia's structure and intensity change. In particular, the analysis covers three stages of Ophelia's lifecycle that involve the ocean

specifically: the storm-induced cold pool interaction, the expansion of the RMW and strongest convection (storm size impact on the preexisting cold pool), and recovery during propagation over the Gulf Stream.

The process of storm-induced upwelling and mixing of colder ocean waters was shown with storm and earth-relative snapshots and azimuthal average profiles of T100. Quadrant-specific profiles of radar reflectivity, surface wind, and moisture disequilibrium quantities show the stabilization of the near-surface atmosphere and structure change as the cold pool evolves. Two-dimensional azimuthal average radius-height diagrams and flight-level horizontal transects of radar reflectivity and wind speed, as well as CFADS are used to verify observations and analyze the inner core collapse in the coupled TC.

Expansion of the storm after moving away from the cold pool was analyzed in terms of the horizontal distribution and spreading of cold T100, broadening and shallowing of the circulation, and the momentum transfer via wind stress to the ocean by the model TC surface winds. Analyses included storm-relative horizontal maps of T100 and surface currents to show the cold pool evolution both at the surface and over the upper ocean. A timeseries of IKE and RMW is also included to show the changes in the amount of kinetic energy transferred to the ocean as a function of the size of the storm surface circulation. Structure and intensity changes were shown with similar analyses as in the cold-pool interaction stage.

The final stage of analysis was focused on the model storm's recovery over the Gulf Stream. Structure and intensity changes were investigated similarly, using storm-relative horizontal and 2D azimuthal average radius-height diagrams to show the storm's location relative to warmer SST and deeper OML and capture the recovery of the

convection with the newly formed eye. Grouped CFAD and CFAD difference ( $\text{AO} - \text{UA}$ ) diagrams were used to show recovery of the vertical depth and distribution of reflectivity during this final stage. These diagrams, being 2D histograms, also show the storms were quantitatively different from one another throughout the simulations and reflect different storms in spite of numerical model precipitation bias.

### **Chapter 3: Structure and Intensity Evolution in Hurricane Ophelia (2005)**

As part of RAINEX, Hurricane Ophelia was extremely well observed by aircraft and satellites. Airborne radar and GPS dropsonde observations were particularly extensive for this storm, and are used in this study to describe changes in the structure of the convection, circulation, and boundary layer environment as a consequence of air-sea interactions. Aircraft flight-level wind measurements and surface wind estimates from airborne stepped-frequency microwave radiometer (SFMR) provide high-frequency sampling of the vortex circulation structure. Satellite data are used to show the upper-ocean temperature evolution and capture changes in the distribution of moderate and intense convection, particularly during the cold-pool and Gulf Stream interactions. Additional analysis product data from the Statistical Hurricane Intensity Prediction Scheme (SHIPS; DeMaria & Kaplan 1994) and NOAA Hurricane Research Division (HRD) H\*WIND archive are included to highlight observed changes in environmental wind shear and Ophelia's surface winds, both of which are relevant to the storm's structure and intensity. Collectively we use these observations to provide a detailed synthesis of the storm's structure changes and explain how interaction/exchanges between the storm and its atmosphere-ocean environment may have been crucial to facilitating these changes. Analyses produced with the observational data are used to examine the structure and intensity changes, and the physical mechanism(s) involved in the coupled storm-ocean modification. In this study, the investigation is separated into four stages of Ophelia's life to better understand the role of air-sea interaction in the context of the relationships between physical processes and structure-intensity change in each stage. An overview of the observational datasets, followed by a thorough account of

structure and intensity changes in each of the four life stages is presented in this chapter forthwith.

### 3.1 Observational datasets

#### 3.1.1 Airborne Radar

The NOAA Hurricane Research Division (HRD) three-dimensional (3D) Doppler analysis (DA; Marks & Houze 1984; Gamache et al. 2003) radar reflectivity, zonal wind, and meridional wind are used both in horizontal (3-kilometer altitude approximating flight-level) and vertical (along and cross track) slices to show the evolution of Hurricane Ophelia's eye, eyewall, and rainband features. Specifically, these observations elucidate structure and intensity changes in the hurricane by showing how the intensity, symmetry, vertical depth, and storm-relative location of precipitation and circulation structures change in time. Analyses were constructed from NOAA WP-3D N42 and N43 X-band tail radar (TA) data that was automatically quality-controlled (QC) and interpolated onto three-dimensional grids with 2-kilometer horizontal and 0.5-kilometer vertical resolution using a variational analysis technique described in Gamache et al. (2003). Observations from these analyses were available for the period September 9 0206 UTC – September 14 0010 UTC, including the period encompassing both the RAINEX RF04 and RF05 flight times. Though the data extends from 0 to 18-kilometers in 0.5-kilometer increments, coverage varies by altitude away from flight-level and may include errors incurred during the automatic QC process. This process includes navigational correction, de-aliasing, interpolation to Cartesian grid, and the actual 3D retrieval using variational analysis (see Testud et al. 1995, Reasor et al. 2009, and Gamache et al. 2003 for more details on these processing stages). A recent modeling study evaluating the quality of 3D DA with

synthetic data from the Hurricane Weather Research and Forecasting (HWRF) model found horizontal wind field errors to be small and storm structural representation in the analysis produced to compare reasonably well with the HWRF “truth” 3D wind field (Lorsolo et al. 2013).

### ***3.1.2 Flight-Level and SFMR***

Beginning in 2005, both NOAA WP-3D N42 and N43 aircraft were equipped with stepped-frequency microwave radiometers (SFMR). SFMRs are downward-looking hurricane reconnaissance instruments that use brightness temperature measurements at six frequencies (4.5, 5.1, 5.6, 6.3, 6.9, and 7.2 GHz) to measure emissivity at the ocean surface. Using a surface emissivity-wind relationship algorithm, these measurements can be used to estimate surface wind speed (Uhlhorn et al. 2007). Path-integrated surface rain rate is estimated using microwave brightness temperature measurements and a prescribed relationship between hydrometeor attenuation (scattering) and rain rate (Uhlhorn & Black 2003 Appendix A). SFMR surface wind speed estimates and flight-level airborne anemometer measurements of wind speed are used in this study. Data were available from September 9 1026 UTC – September 14 0037 UTC, used here in 30s increments. Flight-level and surface wind profiles describe the vertical tilt, shape, and symmetry of the eyewall during times characterized by different storm structures.

### ***3.1.3 Satellite***

Tropical Rainfall Measuring Mission (TRMM) satellite instrumentation provides several observations not confined to the RAINEX RF04 and RF05 flight periods. Specifically, Advanced Microwave Scanning Radiometer-EOS (AMSR-E) data from September 9 – 15 is included in this work. Sea surface temperature (SST) is derived from

microwave brightness temperature measurements from the TRMM AMSR-E radiometer in daily intervals from September 9 – 15 at  $0.25^\circ \times 0.25^\circ$  horizontal resolution. The SST is a merged product optimally interpolated onto a regular grid that has been quality controlled to remove diurnal warming and is representative of the temperature for 12-noon LST. Data is subset to focus on the region nearest to Hurricane Ophelia’s observed National Hurricane Center (NHC) best track and is used in this study to show the daily evolution of the sea surface environment relative to the storm’s position, particularly the observed storm-induced cold pool and the warm features of the Gulf Stream from September 9-14.

NOAA Hurricane Satellite (HURSAT) passive microwave data from the USAF Defense Meteorological Satellite Program Special Sensing Microwave Imager (DMSP SSMI), particularly 85 GHz horizontal and vertical brightness temperature swaths, distinguish the regions of strong to intense convection. This frequency is sensitive to emissivity and scattering of ice phase precipitation in intense convection. Microwave data were available from September 9 0139 - September 14 2323 UTC as individual swaths of  $301 \times 301$  gridded data with  $0.07^\circ \times 0.07^\circ$  horizontal resolution and are each centered on the storm position. For this work, horizontal and vertical polarizations are linearly combined into polarization-corrected (PCT) fields using equations from Toracinta et al. (2002) (Eq. 3.1, 3.2).

$$PCT_{85} = 1.8T_{85V} - 0.8T_{85H} \quad (3.1)$$

$$PCT_{37} = 3.2T_{37V} - 1.2T_{37H} \quad (3.2)$$

### **3.1.4 Buoy**

The RAINEX field campaign's primary observational focus was to simultaneously sample eyewall and rainband structures from radar and dropsondes, with little emphasis on ocean measurements. Due to Ophelia's track, in-situ ocean data is only available at two National Data Buoy Center (NDBC) buoy sites (41010 and 41002). NDBC 41010 is located 120 nm E of Cape Canaveral, FL, whereas NDBC 41002 is 225 nm S of Cape Hatteras, NC. 10-minute measurements of 0.6-meter depth water temperature and surface pressure from these buoys are used to show changes in upper ocean temperature and surface pressure simultaneously. In particular, NDBC 41010 observations provide the best observed account of near-storm SST during the time of the first RAINEX flight (RF04) on September 9, when Ophelia was in an organizing stage with minimal intensity change. NDBC 41002 was the only buoy near the observed storm-induced cold pool, therefore it documents cooling of near-storm SST and rising surface pressure during Ophelia's passage west of the buoy site while executing an anti-cyclonic loop, September 10 1800 UTC – September 12 0600 UTC.

### **3.1.5 GPS Dropsondes**

Along with unprecedented radar observations, the NOAA WP-3D N42, N43, and Gulfstream-IV (G-IV,N49) aircraft deployed a large number of global positioning satellite (GPS) dropsondes into Ophelia's eye, eyewall, and rainbands. A total of 232 dropsonde profiles were available from September 9 – 15, with 38 deployed by N42, 37 from N43, and the remainder by G-IV. The former two primarily sampled the inner core of the storm, while the latter sampled mainly the ambient environment. Each dropsonde provided flight-level to surface observations of pressure, air temperature (TA), relative

humidity (RH),  $u$ -wind,  $v$ -wind, overall wind-speed and geopotential height (Z). Derived equivalent potential temperature ( $\theta_e$ , EPT) was also included for each dropsonde.

The dropsonde profiles give a thorough account of the storm's changing boundary-layer stability and moisture content with 10-second temporal and 5-m vertical sampling resolution, specifically during the cold-pool and Gulf-Stream interactions. Tropical cyclone cold wakes have been shown to be associated with the formation of a stable boundary layer (SBL) investigated in previous work (Lee and Chen, 2014) using dropsonde profiles. The authors' discovery of non-local impacts on TC vertical structure (i.e. convection) coupled with the unique propagation of Ophelia over its' cold pool provide motivation and context for their use in this study. The set of all profiles separated by day of observation are further categorized into three bins by scaled distance from the radius of maximum wind (RMW) based on best-track derived storm center fixes linearly interpolated to 10-min intervals. Deployments less than or equal to 1 RMW are denoted 'eye' profiles, while those within 1-3 RMW are denoted 'inner core' profiles. Any dropsonde deployments between 3-5 RMW are designated 'outer core' profiles. Dropsondes deployed beyond 5 RMW are not included here in order to focus on the near-surface atmosphere internal to the storm and its peripheral regions only. These demarcations provide a storm-size consistent framework for examining changes in Ophelia's boundary-layer structure.

### **3.1.6 SHIPS Wind Shear Product**

The wind shear data in this study was taken from an archive of 1982-2015 Atlantic tropical cyclone developmental data including predictor outputs from the SHIPS model for each TC within those years. For Ophelia, this includes the shear magnitude in

6-hourly intervals between September 9 0000 UTC – September 15 0000 UTC. Shear is computed over the deep troposphere layer 200 – 850 hPa, averaged within an annulus 200 – 800 km from the storm center at each time.

### **3.1.7 H\*WIND Analysis**

The NOAA HRD H\*WIND surface wind analysis product was available for Ophelia in approximately 6-hour increments between September 9 0130 UTC – September 14 0130 UTC. Near-surface (10-m) wind components are provided in the files and used to show the evolution of Ophelia’s near-surface winds, storm size (via RMW), and integrated kinetic energy (IKE). Each analysis file was created from a composite of ship, buoy, coastal platform, reconnaissance aircraft (e.g. NOAA WP-3D), and remotely sensed (satellite-derived) surface wind observations that are then quality-controlled to 10-m height. The effective time-series of RMW, IKE, and  $\sim 0.05^\circ \times 0.05^\circ$  near-surface wind data provided with these analyses are particularly useful in this work to show how changes in Ophelia’s near-surface circulation structure (including size) have implications for the storm’s resiliency, precipitation structure, and interaction with the upper ocean. IKE was calculated as defined in Powell and Reinhold (2007).

### **3.2 Asymmetric near-hurricane prior to cold pool formation**

From 0000 UTC September 9 until approximately 1800 UTC September 10, Ophelia fluctuated between tropical storm and hurricane intensity four times. Although the structure of both the precipitation and circulation were markedly asymmetric during this time, Ophelia attained hurricane intensity by 1800 UTC September 10 and maintained this intensity for  $> 6$  hours continuously. Structure and intensity changes during this organizing stage were the product of both moderate vertical wind shear and moderately

warm SST beneath the storm. Figure 3.1a shows the University of Wisconsin/CIMSS GOES-12 wind shear product in a large-scale view from 20-120°W and 0-60°N valid September 9 1500 UTC, while 3.1b provides the TRMM AMSR-E merged daily SST and Ophelia's center position for September 9 1600 UTC.

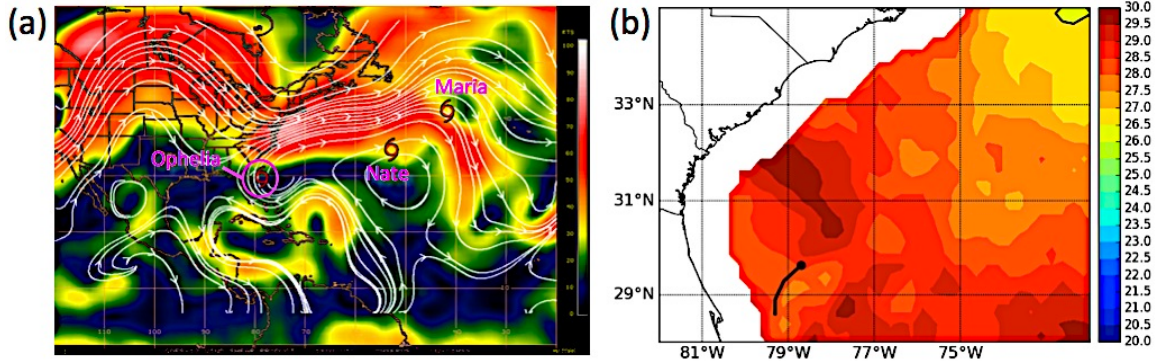


Figure 3.1 (a) University of Wisconsin/CIMSS wind shear product (200-850 hPa deep-layer in colors, kt) overlaid with 200 hPa white streamlines for September 9 1500 UTC. The storm center location of Ophelia, Nate, and Maria are indicated by the tropical storm symbols (b) TRMM AMSR-E merged daily SST overlaid with Ophelia's track since September 9 0000 UTC and position at September 9 1600 UTC.

Late on September 9, a large region of high shear was located to the north of Ophelia and Nate, maximizing downstream of an upper-level trough situated over the Canadian Maritimes. Meanwhile, as shown in Figure 3.1b, Ophelia was beneath moderately warm 27 – 28°C SST. Results from a study on vertical wind shear in eastern Pacific Hurricanes Olivia (1994) and Jimena (1991) by Black et al. (2002) support the hypothesis that efficiency loss due to vertical wind shear and the subsequent decrease in TC intensity may be (at least partially) offset by a strong oceanic energy source, particularly in strong hurricanes. Although Ophelia was not a major hurricane it did possess asymmetric structure, and Black et al. (2002) observed Jimena was able to maintain near-constant intensity while experiencing moderate shear (e.g. < 15.56 kt) while over > 28°C SST, despite having asymmetrically distributed convection in its inner core.

Over an 18h period beginning September 9 1800 UTC, the upper-level trough began moving eastward, with the region of the strongest shear lessening and shifting east. Distribution of the shear and its location relative to Ophelia is shown in Figure 3.2a. Each panel includes a spatial map of NCEP final analysis (FNL) shear along with the storm track, shear and storm motion vectors, and SHIPS developmental data deep-layer shear (DLS, 200 – 850 hPa) value. Timeseries of NHC MWSP (every 6h, kt) and SHIPS DLS are given in Figure 3.2b.

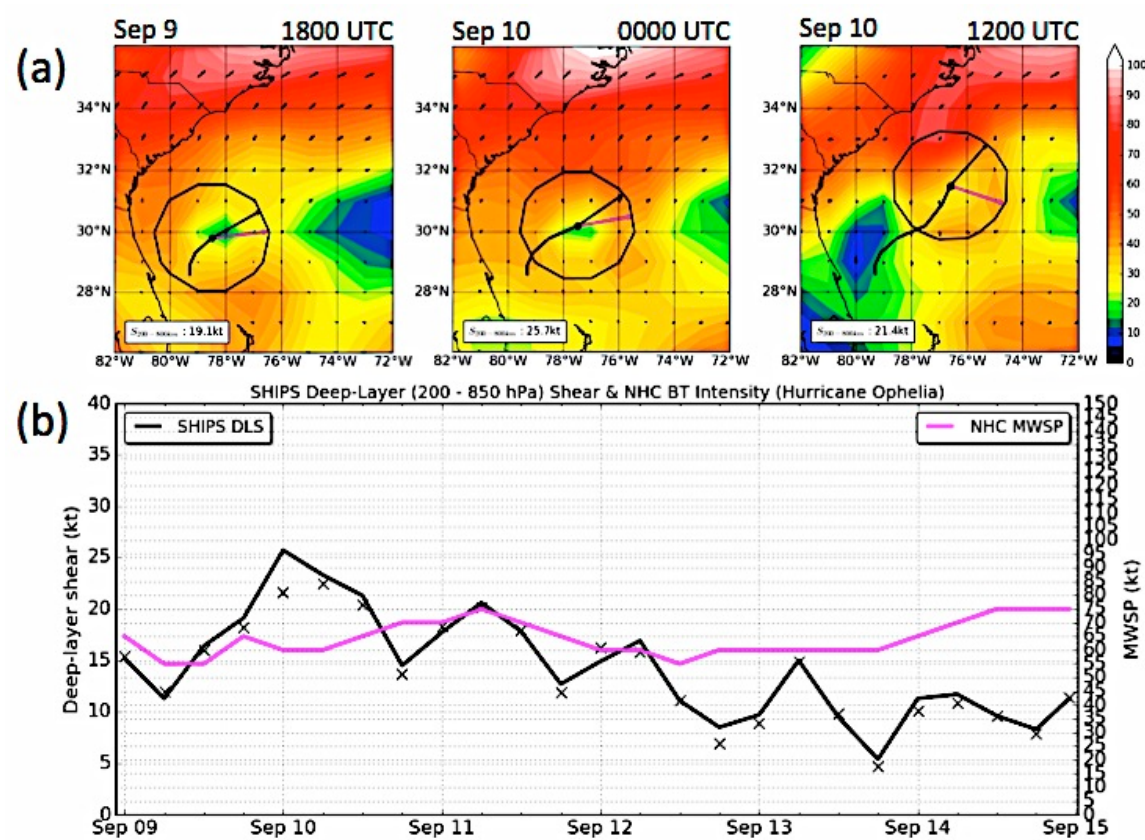


Figure 3.2 (a) NCEP final analysis (FNL, GFS + late observations) DLS maps for September 9 1800 UTC, September 10 0000 UTC, and September 10 1200 UTC (SHIPS uses real-time GFS). The black thick line denotes the storm track from September 9 0000 UTC through the time indicated. A black arrow shows the storm heading. The magenta arrow denotes the shear vector. The black circle indicates 200-km from storm center. Black quivers show the 200-hPa wind (b) Timeseries of 6-hourly SHIPS DLS (black x's), FNL DLS (black line), and 6-hourly MWSP. All values given in knots.

From Figure 3.2 it is evident that vertical wind shear is near or exceeds 20 kt between September 9 1800 UTC and September 10 1200 UTC, peaking September 10 0000 UTC. Ophelia's intensity weakened to tropical storm strength (60 kt) as shear exceeded 20 kt ( $\sim 10.3 \text{ ms}^{-1}$ ) and leveled off for 6h before beginning to intensify as shear falls below 20 kt around September 10 1200 UTC. Ophelia re-strengthened to a hurricane (MWSP 70 kt) by September 10 1800 UTC. After September 11 0600 UTC, SHIPS DLS does not again exceed 20 kt and exhibits gradual weakening day to day through September 15.

The juxtaposition of DLS and MWSP behavior demonstrate that the impact of vertical wind shear on Ophelia changes between the period prior to September 11 0600 UTC, and the period thereafter. During the first 48h in 3.2b, moderate to high shear limits intensity change; however, as shear continues to decrease Ophelia's MWSP either decreases or remains near steady through September 13 1800 UTC. Ophelia fails to intensify despite increasingly favorable large-scale atmosphere environment due to interaction with its induced cold pool September 11-12. Given the low DLS after September 11 0600 UTC, interaction with the ocean is likely critical to intensity changes after this time, including both the cold pool interaction, and recovery over the Gulf Stream.

Ophelia's asymmetric structure was captured by NOAA WP-3D aircraft radar during the RF04 RAINEX flight on September 9. The vertical wind shear direction shifted from south/southwesterly to westerly/northwesterly September 9 – 10 (see Figure 3.2a), and the most prominent precipitation feature was a large rainband extending anti-cyclonically from forward-left toward the rear-right quadrant characterized by 30-35 dBZ radar reflectivity returns at flight-level. The NOAA WP-3D tail radar (TA) 3D Doppler

Analysis (3D DA) flight-level (3km) composite for September 9 1258 UTC – 1446 UTC is shown in Figure 3.3. For each composited variable, the data reflects several flight legs combined into a single, representative pass that is presented in storm-relative space. Panels (b) and (d) give the azimuthal average of reflectivity and wind ( $V_t$  solid,  $V_r$  dashed) respectively, as well as the coverage percentage (ratio of good data points/total data points).

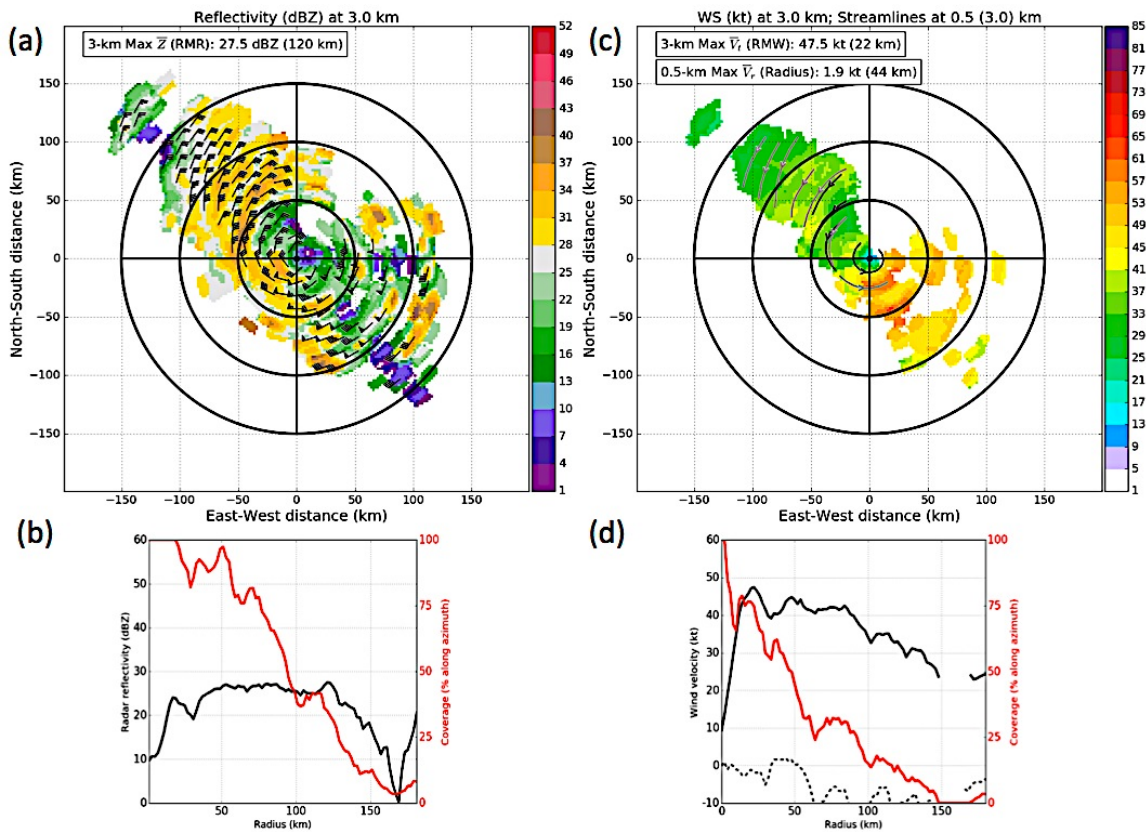


Figure 3.3 (a) NOAA HRD 3D Doppler Analysis (3D DA) composite flight-level radar reflectivity (dBZ) for September 9 1258 UTC – 1446 UTC. Azimuthal average flight-level RMR and value at that radius are indicated at top left. Black wind bars give the flight level wind (kt) (b) Azimuthal average radar reflectivity profile (dBZ, black) and composite coverage along each azimuth (%, red) (c) Same as (a) except for flight-level wind speed. Black (grey) streamlines are at 0.5km (3 km) altitude. (d) Same as (b) except for tangential wind speed (kt, solid black) and radial wind speed (kt, dashed black).

The flight-level reflectivity composite in 3.3a shows the aforementioned dominant rainband extending radially inward toward a small low-dBZ eye region. Azimuthal averaging of the reflectivity identifies the radius of maximum reflectivity (RMR) as 120km (with 27.5 dBZ value), although the data coverage is less than 25% at this radius (Figure 3.3b). Based on Figure 3.3a-b, it is more likely that the true RMR was masked due to missing data and the asymmetry of the storm at this time. Furthermore, the true RMR is likely near 50km, where coverage is near 100% simultaneous with a crescent shaped segment of moderate reflectivity. The flight-level wind speed composite in Figure 3.3c possesses a small but well-defined eye and places the strongest observed winds in the rear-right quadrant. The outermost of two ‘bands’ of strong winds is near 50km and near the location of the tip of the broad rainband seen in 3.3a. Azimuthally averaged tangential velocity identifies the RMW as 22km from storm center with approximate maximum winds of 48 kt (tropical storm force), which is a reasonable estimate given the nearly 75% coverage (Figure 3.3d). Vertical cross-sections taken west-east cross track (Figure 3.4a-b) and south-north along track (Figure 3.4c-d) through the composites show Ophelia was asymmetric throughout the depth of the storm, particularly in the cross-track direction here due to shear. Furthermore, the storm was relatively shallow when comparing the extent of the strongest reflectivity (e.g. 30+ dBZ returns) and winds (~6-8 km) to the entire depth (~12-14 km).

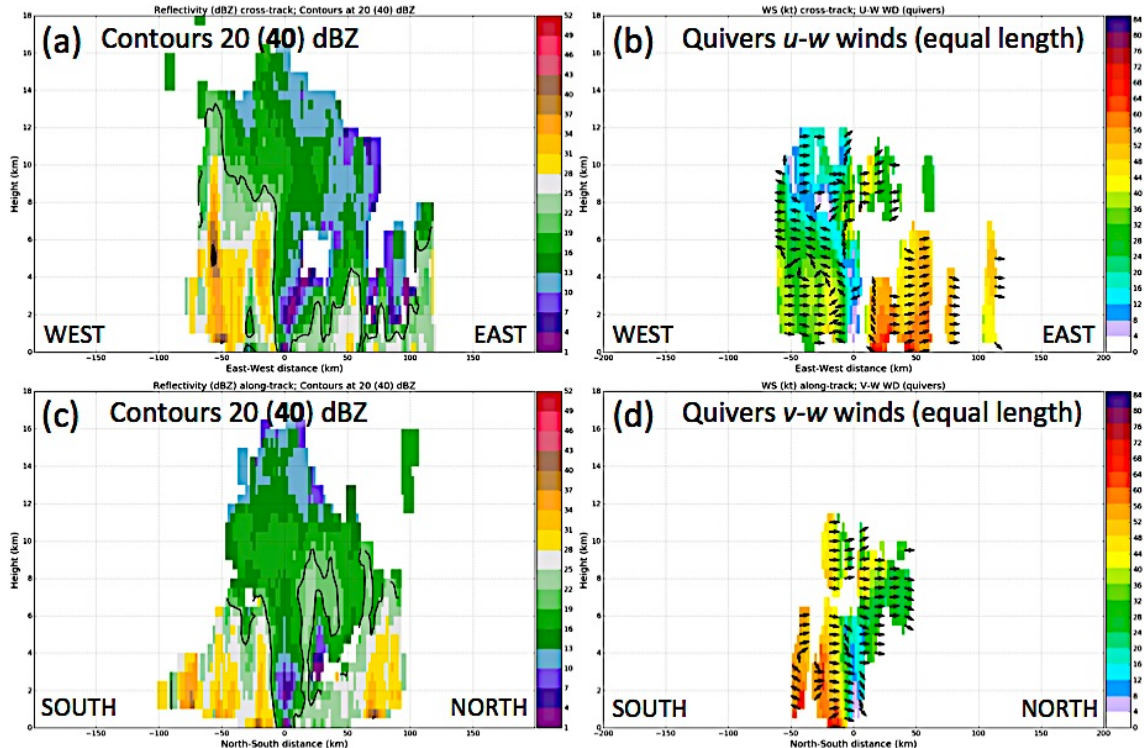


Figure 3.4 Vertical transects of (a,c) radar reflectivity and (b,d) horizontal wind taken through the composites in Figure 3.3. Slices in (a) and (b) are taken across-track, whereas (c) and (d) are taken along-track. Contours in (a) and (c) denote 20 (light to moderate) and 40 (strong to intense) dBZ. In (b) and (d), quivers depict the indicated 2D wind structure.

Convergence and upward motion as described by the wind quivers in 3.4b,d varies in the two transect directions, but is within 50km of the storm center where it occurs. Upper-level winds are largely westerly and southerly, consistent with the large-scale environmental winds and the shear (which was increasing over the composite time). Two radially thin towers of moderate to strong returns are seen ~20 and ~50 km from storm center in Figure 3.4a,c. Low-level winds converge, transition to upward and then westward between 1-5km depth collocated with the radially outward sloping tower of moderate reflectivity observed 20km from storm center (compare Figure 3.4a,b). This feature would wrap around the storm center and become part of Ophelia's eyewall once the storm regained hurricane intensity on September 10. The second tower, about 30km

outside the first contained the strongest returns. The dark contour at about 5km and generally horizontal orientation of the wind suggest this is a stratiform bright-band, although we do not discount the presence of vertical motion given the structure of the reflectivity returns with the feature. Stratiform precipitation lies between the two towers, and is particularly evident in the shallower north and east regions. The adjacent location of convection and stratiform precipitation, radially outward slope of the two tower features and potential bright band collectively support Ophelia having a traditional, MCS-like (though asymmetric) precipitation structure. Despite having a well-defined eye at flight-level, the transects in Figure 3.4b,d provide coarse evidence of the impact of wind shear disrupting the vertical structure of the vortex as the low-wind region is nearly upright at the surface, but then appears to deviate with height. Airborne anemometer and SFMR measurements through Ophelia's center provided real-time high-frequency winds at the surface (estimated) and flight-level to elucidate the tilt and asymmetry of the vortex more clearly. The profile for September 9 1300 UTC – 1350 UTC is given in Figure 3.5. Times were selected to isolate a complete pass across the storm as best as possible.

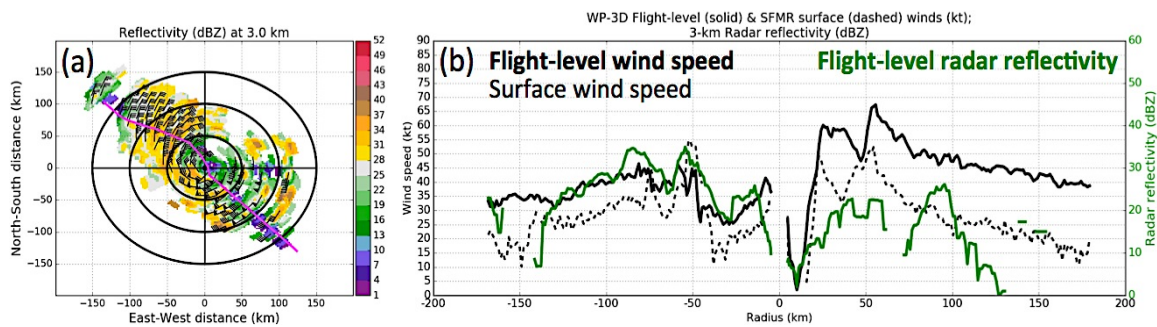


Figure 3.5 (a) NOAA HRD 3D DA flight-level radar reflectivity composite as in Figure 3.3a, overlaid with the aircraft flight path September 9 1300 UTC – 1350 UTC (b) Profile of aircraft flight-level wind (kt, solid black), SFMR surface wind estimate (kt, dashed black), and flight-level radar reflectivity from the composite (dBZ, green).

Flight-level radar reflectivity (as in Figure 3.3a) is provided as a reference, with the flight path of the NOAA WP-3D aircraft overlaid in panel (a), with wind and corresponding radar reflectivity profile along the path in panel (b). Presented in radius from storm center, the asymmetry in the vortex from forward-left to rear-right is apparent. Maximum flight-level wind speed, attained near 50km from center on each side of the vortex, differs by 20 kt. Wind and reflectivity in the forward-left quadrant are more or less aligned, with two peaks near 25 and 35 dBZ (within 50 km from center) corresponding to the along-path signature of the rainband. On the opposite segment in the rear right quadrant however, flight-level wind speed is 10-20 kt stronger than the surface wind estimate within 100 km of storm center and the flight level profile is somewhat tilted. The local minimum in flight-level wind speed near 50 km from center is approximately 20 km radially outward from the corresponding surface minimum. Furthermore, the radar reflectivity profile is not consistent with either the flight-level or surface wind maxima. Passing through the entire storm, these profiles clearly indicate Ophelia's circulation was asymmetric, tilted, and lacked the resiliency\* of a more coherent TC vortex due to wind shear, hindering intensification but having limited consequences for the maintenance of precipitation structure associated with a developing TC.

Satellite and buoy observations of SST, along with data from airborne GPS dropsondes deployed on September 9 provide insight to the ocean's influence in supporting healthy TC precipitation structure, both in terms of near-storm SST and temperature and moisture differences between the sea surface and boundary-layer atmosphere that are relevant to air-sea enthalpy flux. TRMM AMSR-E merged daily SST and surface-1.5km vertical profiles of air temperature (TAIR, deg C) and equivalent

potential temperature (EPT, deg K) for the dropsondes deployed by NOAA WP-3D N42, N43, and G-IV (N49) aircraft on September 9 are shown in Figure 3.6. SST-relative and RMW-relative position for the 30 dropsondes within 5-RMW of the storm center for each deployment time are included in panels (b) and (c).

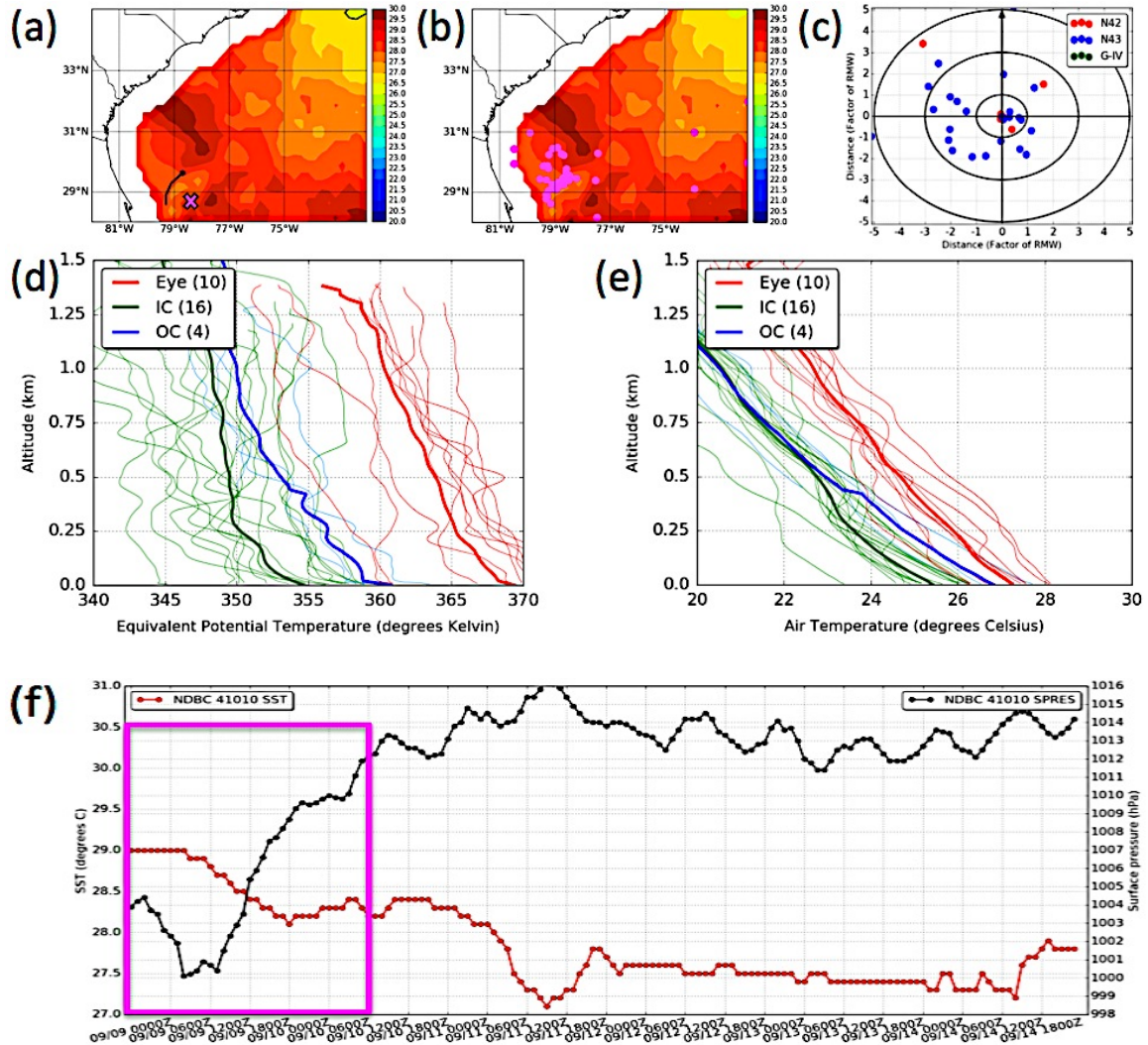


Figure 3.6 (a) TRMM AMSR-E merged daily SST for September 9 since September 9 0000 UTC and center position at September 9 1600 UTC. The magenta 'x' indicates the position of the buoy NDBC 41010 (b) Same as (a), except overlaid with the latitude-longitude positions of the September 9 dropsondes (magenta) (c) Storm-relative location of the September 9 dropsondes by RMW (d) 0-1.5km equivalent potential temperature (EPT, deg K) profiles from the September 9 dropsondes (e) Same as (d) except for air temperature (TAIR, deg C) (f) 0.6m water temperature (red) and surface pressure (black) measured by NDBC 41010, September 9 – 15.

Figure 3.6a shows Ophelia's track (since September 9 0000 UTC) and location of buoy NDBC 41010. Ophelia's center at September 9 1600 UTC is located at the black dot. Comparing the storm center location with the SST-relative dropsonde locations in panel (b), the satellite derived SST near Ophelia was warm ( $\sim 27 - 28^\circ\text{C}$ ). Mean surface air temperature from the 16 inner-core (1-3 RMW) profiles was  $25.4^\circ\text{C}$ , cool enough to favorably support evaporation (sensible heat flux to the atmosphere). Additionally, the mean air temperature from the 10 eye ( $< 1 \text{ RMW}$ ) profiles was consistently warmer than the inner (IC) and outer core (OC) ( $\sim 27^\circ\text{C}$  at the surface;  $> 1.5^\circ\text{C}$  than IC and OC above 0.5km, Figure 3.6e). Subsidence warming is a common feature in the eye that is a signature of the TC 'warm core'. Equivalent potential temperature profiles shown in panel (d) convey information about both the temperature and moisture content of air parcels sampled by these dropsondes. Mean IC EPT has a near-surface maximum of 355K, diminishing to a vertically uniform (well-mixed) boundary-layer profile around 350K. The eye profile average is substantially warmer throughout the 0-1.5km layer, with a surface value near 370K. Since EPT describes the temperature air parcels would have if all latent heat were released (via condensation) and the parcel were lowered adiabatically to the surface but the TC eye is typically warm and dry, this warm profile supports the presence of a healthy thermodynamic TC structure. Based on observations of the environment and structure during this stage of Ophelia's life, while it is clear wind shear plays an important role in disrupting the storm circulation (thereby intensification), the support of positive enthalpy flux promoted at the very least the maintenance of organized precipitation structure.

### 3.3 Shallowing, asymmetric structure traversing cold pool

Originally forecast to intensify over warm waters of an eastern segment of the Gulf Stream to its north/northeast, Ophelia was investigated in a second reconnaissance flight (RF05) as part of RAINEX/IFEX September 11 – 12. Tropospheric steering flow remained weak and the storm executed a slow, anticyclonic loop from September 10 1800 UTC through September 12 0600 UTC. While making the loop, Ophelia induced strong cooling of the upper ocean beneath itself via upwelling and vertical mixing. Turning southward by September 11 0600 UTC and west/northwestward beginning September 12 0000 UTC, the storm propagated over its cold pool while the cool SST remained near the inner core. Due to this interaction, Ophelia’s structure became unusually shallow and asymmetric. Additionally, RAINEX observations captured a collapse of the inner core, and evolution of precipitation and circulation structure similar to the eyewall replacement cycle (EWRC, Willoughby et al. 1982; Willoughby 1988) experienced by Hurricane Rita (2005, Houze et al. 2006) and other stronger TCs. Weakening continuously from 75 kt September 11 0600 UTC to 60 kt through September 12 0600 UTC, the structure changes experienced by Ophelia during interaction with its cold pool accompany the longest and most rapid decrease in intensity experienced by the storm. Figure 3.7 shows the TRMM AMSR-E merged daily SST for September 11 and 12 in panels (a) and (b) respectively. Between (a) and (b), Ophelia cools SST between 0.5 – 2°C. The black contour in 3.7a-b denotes 26.5°C.

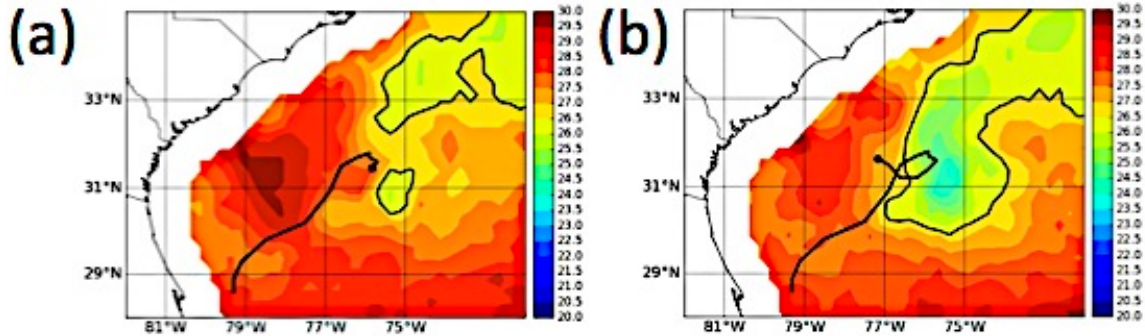


Figure 3.7 TRMM AMSR-E merged daily SST overlaid with Ophelia's storm track since September 9 0000 UTC for (a) September 11 (center position 1600 UTC) (b) September 12 (center position at 1600 UTC). The black solid contour denotes 26.5°C.

As described in Houze et al. (2006), a pillar objective of the RAINEX field campaign was to observe the interaction of eyewall and rainband internal structures. These structures have been described thoroughly in previous studies (Willoughby et al. 1984; Willoughby 1988). Though the exact mechanisms remain unclear, the eyewall replacement cycle (EWRC) is one such eyewall-rainband interaction event whereby intensity changes due to evolving internal structure (see Willoughby et al. 1982; Black and Willoughby 1992). Prior to EWRC, the TC eyewall and rainbands are distinct features and the rainbands spiral inward and connect with a single eyewall. Development of a secondary horizontal wind maximum (SHWM) within a principal or outer rainband has been found to be associated with formation of the outer eyewall in EWRC, during which the rainband transitions toward eyewall-like structure (Samsury and Zipser, 1995). Once the secondary eyewall becomes axisymmetric about the inner eyewall, the inner eyewall is cut-off from nonlocal advection of moisture in the low-level inflow region and collapses. The 3D DA flight-level composite for September 11 1616 UTC – 1812 UTC depicting Ophelia's inner core as the storm was propagating over its cold pool is given in Figure 3.8.

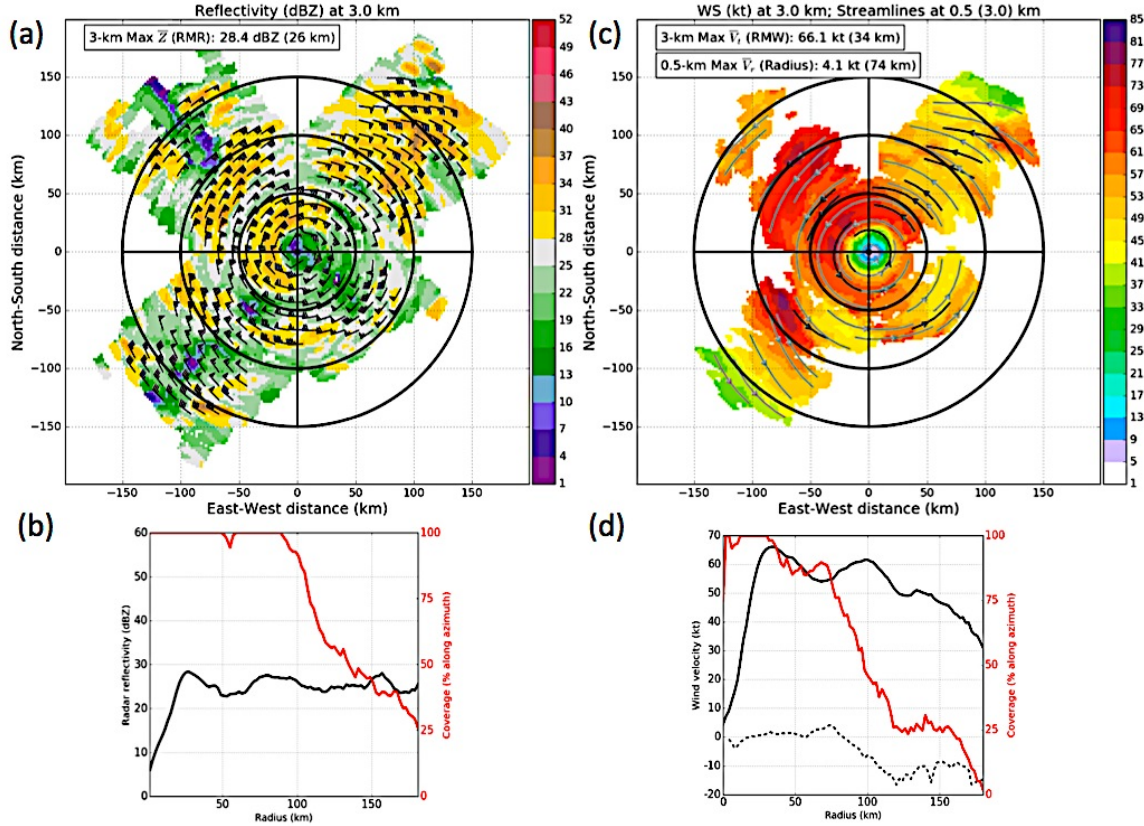


Figure 3.8 (a) NOAA HRD 3D Doppler Analysis (3D DA) composite flight-level radar reflectivity (dBZ) for September 11 1616 UTC – 1812 UTC. Azimuthal average flight-level RMR and value at that radius are indicated at top left. Black wind barbs give the flight level wind (kt) (b) Azimuthal average radar reflectivity profile (dBZ, black) and composite coverage along each azimuth (%, red) (c) Same as (a) except for flight-level wind speed. Black (grey) streamlines are at 0.5km (3 km) altitude. (d) Same as (b) except for tangential wind speed (kt, solid black) and radial wind speed (kt, dashed black).

Several different structure changes and features can be seen at first glance in Figure 3.8. Most obviously, the strongest precipitation and winds are asymmetrically distributed about the storm. Comparing (a) and (c), the weaker reflectivity returns and wind speed are collocated, suggesting the primary and secondary circulation are aligned. This also implies that the asymmetric structure signified by these regions of weaker precipitation and winds has been facilitated by a disruption in the TC's primary energy source (the ocean) that then translates to air-sea enthalpy flux, support for convection, and ultimately

the spin-up of the tangential velocity (stronger winds). A second, subtler feature becomes clear when considering the entire composite. Although Ophelia's structure is asymmetric, it appears substantially more axisymmetric in this stage. Furthermore, from visual inspection the storm appears to possess both a crescent-shaped, partially eroded inner eyewall inside 50km as well as a nearly complete second ring of axisymmetric precipitation near 100km (Figure 3.8a). A similar structure is seen in the flight-level wind speed composite in panel (c), with two horizontal wind maxima – one inside 50km, and a second narrower feature just inside 100km. Additionally, both sets of double-maxima are separated by regions of weaker precipitation and wind (a moat) in between. To quantify the robustness of these features, the azimuthal average profiles are compared with data coverage in panels (b) and (d) in the same manner as for Figure 3.3. Azimuthally averaged RMR and RMW were found to be 26km and 34km respectively for this composite. These maxima are consistent with the partially collapsed inner core eyewall, and both radii have  $> 85\%$  coverage. The azimuthally averaged profiles also show a secondary RMR at about 80km and secondary RMW just inside 100km with near 100 % and 50 % coverage respectively.

While the flight-level composites show Ophelia has axisymmetric concentric rings consistent with the early stages of EWRC, the inner eyewall feature was partially collapsed and hence asymmetric at this time. Vertical transects for this September 11 1616 UTC – September 1812 UTC composite are shown in Figure 3.9. Pronounced asymmetry can be seen best in the cross-track in panel (a). Ophelia's precipitation structure had also weakened and become remarkably shallow (25-35 dBZ maxima reaching 4-6km at best). The location of the weaker rain and winds were found

expectedly where the vertical structure was the most shallow, as those portions of the storm (mainly rear-right of center) were above the induced cold pool. As Ophelia changed direction executing its loop, the extent of the cold pool would change and impact the other inner core quadrants.

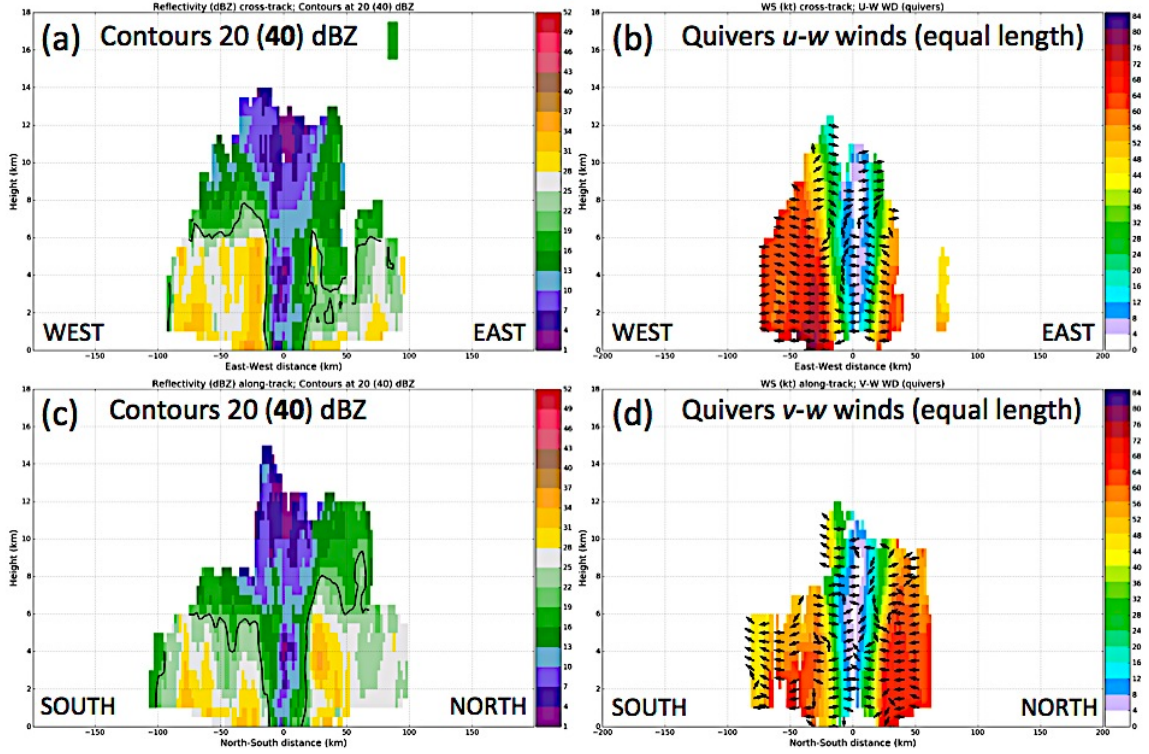


Figure 3.9 Vertical transects of (a,c) radar reflectivity and (b,d) horizontal wind taken through the composites in Figure 3.8. Slices in (a) and (b) are taken across-track, whereas (c) and (d) are taken along-track. Contours in (a) and (c) denote 20 (light to moderate) and 40 (strong to intense) dBZ. In (b) and (d), quivers depict the indicated 2D wind structure.

Low-reflectivity and low-wind regions gradually sloping outward with height can be seen in both transects. The upright and symmetric slope of these features corroborates flight-level observations that Ophelia possesses a well-established, coherent vortex despite interacting with its cold pool. Furthermore, near and above hurricane force winds are present at the surface on the western (in panel b) and northern (in panel d) side of the storm. These stronger winds enhance the TC-ocean feedbacks involved with air-sea

enthalpy flux and TC wind-driven mixing of the upper ocean, regardless of the initial ocean state (although this is important). Convection in Ophelia's inner core has been severely compromised by the cooled ocean environment beneath and near it. Bold contours indicating the location of 40+ dBZ radar reflectivity are absent in both transects. The most convincing convective feature is a tower of moderate radar reflectivity with a core of 30-35 dBZ returns near 4km height located near the azimuthal average RMR at ~25-30 km. This convective tower is situated near the northern eyewall RMW. Throughout the remainder of the storm, transects reveal the precipitation is stratiform in nature. Winds are predominantly horizontal in association with the stratiform rain, sloping slightly upward and outward on the western and southern portions of the storm. A reduced reflectivity region between precipitation structures at ~25km and ~75-80km that appears similar to a 'moat' can be seen in the vertical structure also. Local reduction of radar reflectivity is 5-10 dBZ in these 'moats' on both sides of the storm center in the cross-track transect (panel a) and on the south side of the storm center in the along-track transect (panel c). While Ophelia's shallow and asymmetric vertical structure is captured well in the composites, gaps near surface and away from the storm center, and the 2km spatial resolution of the data obscures finer structure, particularly of the winds. Airborne flight-level wind and SFMR surface wind estimate observations measured during the September 11 (RF05) RAINEX flight provides a more resolved picture of the circulation structure and the presence of SHWM associated with early-stage EWRC. The profile for September 11 1610 UTC – 1700 UTC is given in Figure 3.10.

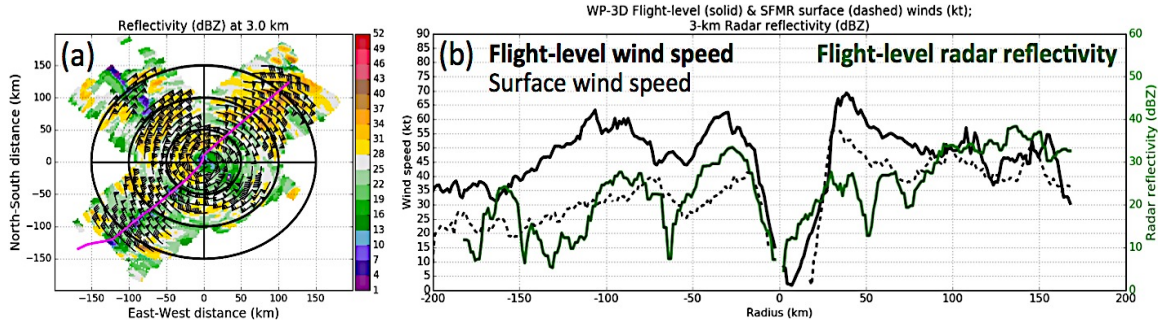


Figure 3.10 (a) NOAA HRD 3D DA flight-level radar reflectivity composite as in Figure 3.3a, overlaid with the aircraft flight path September 11 1610 UTC – 1700 UTC (b) Profile of aircraft flight-level wind (kt, solid black), SFMR surface wind estimate (kt, dashed black), and flight-level radar reflectivity from the composite (dBZ, green).

The magenta line in 3.10a again gives the flight path of the aircraft, which passes directly through the storm center during this leg. Maximum flight-level wind speed is 65-70 kt on either side of the vortex center, approximately 30-40km from the storm center. Two second flight-level wind maxima are observed beyond this radii on each side, one 80-90km along the path in the rear-left quadrant and the other located just outside 100km in the forward-right quadrant. SFMR surface wind estimates also appear to have this double RMW structure, however the entire profile is shifted more radially inward (closer to storm center). The primary surface RMW are at 25-30km from storm center, with secondary peaks at 75km and 90km southwest and northeast of storm center respectively. Radially outward sloping of winds is a typical feature of the eyewall related to TC angular momentum conservation, and is observed with the primary (partially collapsed) eyewall and a second ring of precipitation and strong winds that displays eyewall-like structure. The along-path profile of flight-level radar reflectivity has maxima just inside the two flight-level RMWs in the rear-left quadrant and two in the forward-right quadrant. Local minima in the reflectivity consistent with ‘moats’ are seen ~80km from storm center in both of the sampled quadrants. The exact structure is less clear than the wind

profiles as this reflectivity comes from the 3D DA composite, however, the precipitation and circulation are reasonably aligned within 100km of storm center. Interaction between slow-moving, near-hurricane Ophelia and the upper ocean induces a cold pool over which the storm propagates. The storm's vertical structure becomes asymmetric and shallow due to this interaction, however the inner core eyewall begins to collapse as well. Air-sea interaction hence initiates an atypical style of EWRC in Ophelia.

Ophelia's cold pool was well captured by both satellite (see Figure 3.7) and buoy observations on September 11 and 12 as the storm executes the anticyclonic loop. GPS dropsondes deployed on September 11 sampled the boundary-layer atmosphere, Six (6) in the eye, thirteen (13) in the inner core (IC), and five (5) in the outer core (OC). The deployment times for these dropsondes are between September 11 1616 UTC – 2204 UTC. In a previous study by Lee and Chen (2014), Typhoon Choi-Wan (2009) induced a wake over its rear-right quadrant that cooled SST by  $> 3^{\circ}\text{C}$ . A stable boundary layer (SBL) formed over and azimuthally downstream of the wake and was investigated by the authors using tracer and trajectory analysis of air parcels in the boundary-layer using a high-resolution coupled atmosphere-ocean model. This stability occurs as a result of reduced air-sea enthalpy flux (cooler SST, less evaporation) and was found to suppress convection in Choi-Wan in the rear-right quadrant and azimuthally downstream. Since Ophelia also induces a substantial cold pool, September 11 dropsonde profiles can help distinguish formation of a stable boundary layer and its impact on precipitation structure in Ophelia. Cooler, drier near-surface air from the cold pool, which spreads and encompasses the entire inner core as Ophelia's heading changes September 11 – 12, may also contribute to enhanced air-sea enthalpy flux away from the storm center by reducing

near-surface moisture at distant radii. This air-sea interaction induced modification to the surface moisture flux disequilibrium would be antithetical to the reduction that occurs due to SST cooling in the inner core. The TRMM AMSR-E merged daily SST and surface-1.5km vertical profiles of TAIR and EPT are given in Figure 3.11. SST-relative and RMW-relative positions are also included. Panel (f) shows the 0.6m SST and surface pressure measured by buoy NDBC 41002 (location given by magenta 'x' in panel (a)).

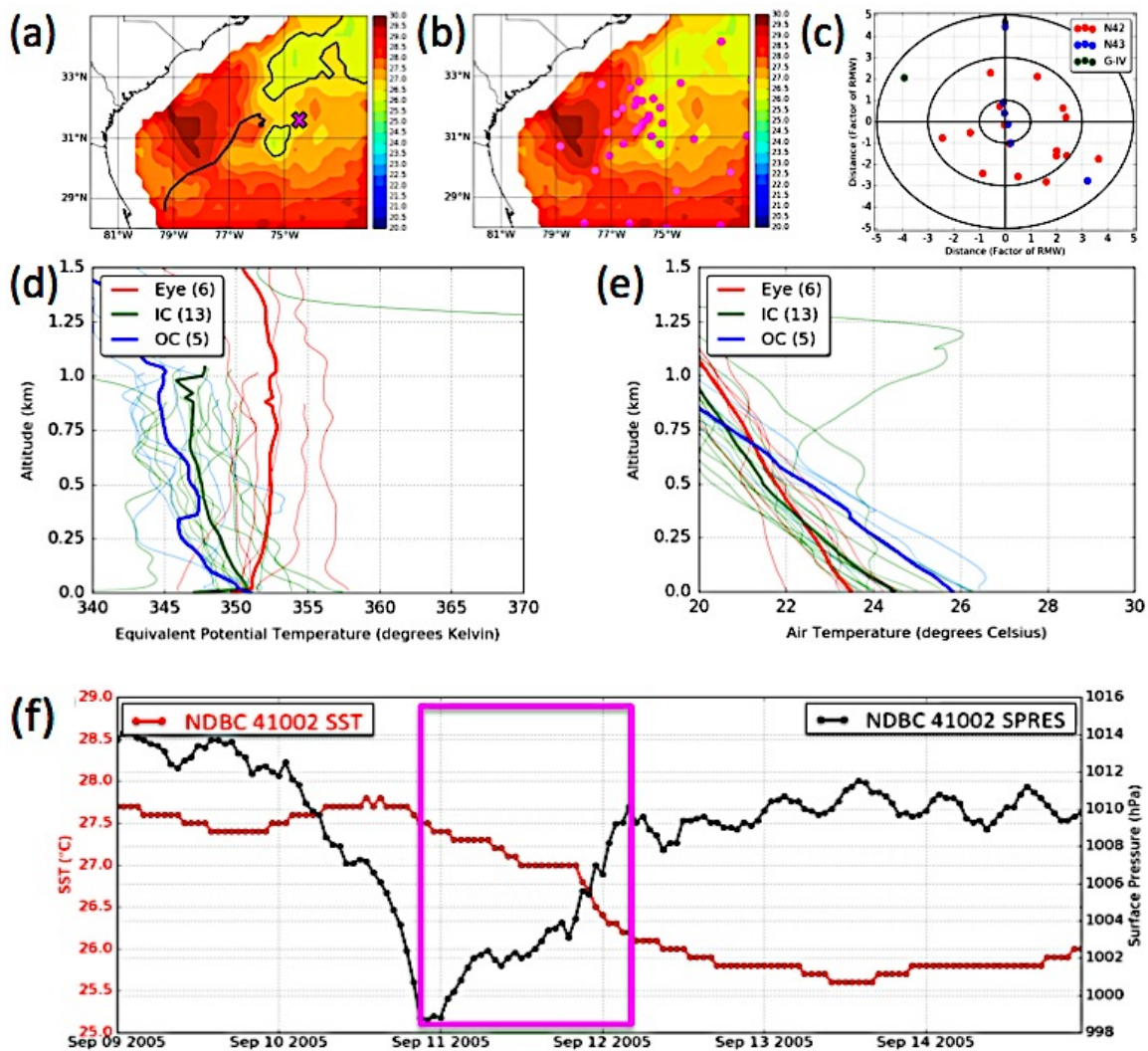


Figure 3.11 (a) TRMM AMSR-E merged daily SST for September 11 with Ophelia's track since September 9 0000 UTC and center position at September 11 1600 UTC. The magenta 'x' indicates the position of the buoy NDBC 41002 (b) Same as (a), except overlaid with the latitude-longitude positions of the September 11 dropsondes (magenta) (c) Storm-relative location of the September 11 dropsondes by RMW (d) 0-1.5km

equivalent potential temperature (EPT, deg K) profiles from the September 11 dropsondes (e) Same as (d) except for air temperature (TAIR, deg C) (f) 0.6m water temperature (red) and surface pressure (black) measured by NDBC 41002, September 9 – 15.

Ophelia's center position at September 11 1600 UTC is denoted by the black dot. All of the IC deployments occur after this time (1616 UTC – 2204 UTC), however this position is chosen to match the approximate noon-LST time of the underlying merged daily SST. Note the cold pool intensifies (cooler SSTs) and spreads moving towards September 12 0600 UTC (see Figure 3.7b). Based on this and the longer memory of the ocean to temperature changes, the true SST underlying the dropsondes approximately ranges between 24 and 25.5°C. Mean surface air temperature from the 13 IC profiles was 24.5°C. The range of IC SST and observed average surface air temperature favor weak air-sea enthalpy flux at best (or near neutral conditions if the lower bound of SST is taken). Mean surface temperature of the eye profiles (23.5°C) is actually less than the inner core, however the slope decreases less radically with height as compared to the IC profiles. Comparing mean EPT with dropsondes from September 9 (see Figure 3.6d), the IC average is 8-9K cooler (drier and/or cooler surface air). The boundary layer appears well mixed however, still almost 10K cooler than the mean EPT when Ophelia was in its organizing stage over warmer SST. The reduced air-sea temperature disequilibrium (as indicated by SST vs. mean air temperature) and inversion in the near-surface EPT of the inner core profiles suggest an SBL does form within this part of the storm late on September 11 (the time of dropsonde deployments). Despite its distance from the storm center throughout the south and westward portions of the anticyclonic loop, buoy observations in 3.11f show the filling of pressure and near-surface ocean cooling

associated with induced cold pool formation and evolution during the passage. The rate of change of both quantities achieves its maximum slope between September 11 1800 UTC and September 12 0600 UTC (highlighted by the magenta box), when Ophelia propagates south and then northwestward over previously upwelled cooler SST. RAINEX observations demonstrate clearly that Ophelia's induced cold pool, facilitated by air-sea interaction, was responsible for both structure and intensity changes. These structure changes included both more typical (e.g. weakening and shallowing of precipitation due to reduced enthalpy fluxes) and also less common (e.g. inner core collapse/initiated EWRC) response to this complex TC air-sea interaction event.

### **3.4 Expanded, shallow storm with peripheral discrete convective rainband**

Ophelia completed an anticyclonic loop around September 12 0600 UTC, and turned toward northwestward while moving away from its cold pool. During this time, the storm was large and possessed an extremely shallow inner core region. The inner eyewall had completely collapsed, and convection was absent within ~75km of the storm center. While the storm was moving away from the cold pool, it straddled warm (undisturbed Gulf Stream waters) and cold (induced cold pool) upper ocean environments (see Figure 3.7b). A flight-level 3D DA composite of aircraft observations from September 12 2000 UTC – 2338 UTC showing the vacuous inner core region and expanded circulation is presented in Figure 3.12.

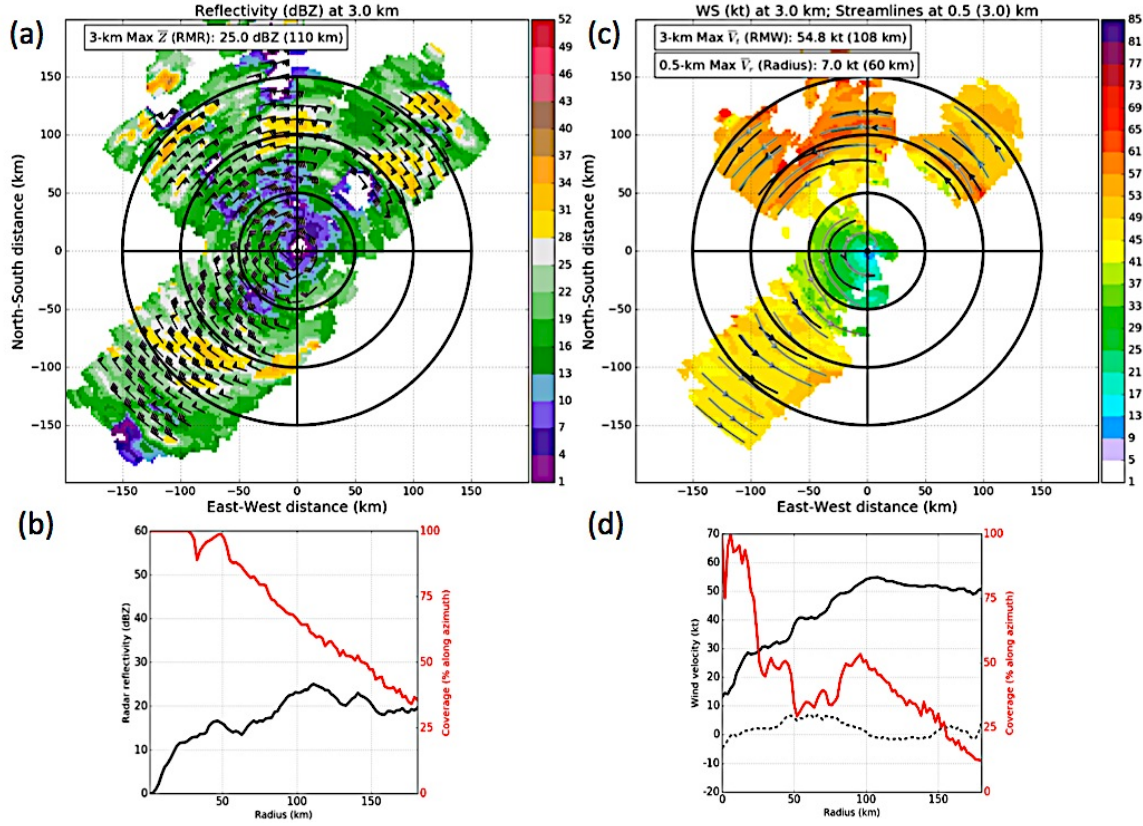


Figure 3.12 (a) NOAA HRD 3D Doppler Analysis (3D DA) composite flight-level radar reflectivity (dBZ) for September 12 2000 UTC – 2338 UTC. Azimuthal average flight-level RMR and value at that radius are indicated at top left. Black wind barbs give the flight level wind (kt) (b) Azimuthal average radar reflectivity profile (dBZ, black) and composite coverage along each azimuth (%, red) (c) Same as (a) except for flight-level wind speed. Black (grey) streamlines are at 0.5km (3 km) altitude. (d) Same as (b) except for tangential wind speed (kt, solid black) and radial wind speed (kt, dashed black).

Azimuthally averaged flight-level RMR and RMW for the composites in 3.12a,c covering the late afternoon of September 12 were found to be 110km and 108km, respectively. Along azimuth coverage was limited for both radii (~50-60% for each based on panels (b) and (d)), however the collocated stronger reflectivity returns and winds (e.g. in the forward quadrants) provide further confidence to the value of the averaged quantities. In addition to being a very large tropical storm (NHC MWSP 60kt; azimuthal average 3-km MWSP 55 kt), the precipitation structure featured a partially complete ring of 30 – 35 dBZ reflectivity returns that can be traced anti-cyclonically about the storm

center from forward right through the rear right quadrant. This structure, though far from the storm center, appears similar to the eyewall-rainband complex that dominated Ophelia's organizing phase on September 9 – 10. Streamlines of the winds at 0.5km depicted in panel (c) show near-surface inflow in the rear-left quadrant and intensification of the flight-level wind moving from forward-right to forward-left. Radial velocity direction also shifts from slightly radially outward to nearly geostrophic along this path. The increased wind speeds in Ophelia's forward quadrants (see Figure 3.12c) correlate well with the location of precipitation at this time. Given Ophelia's size (~200km diameter), the forward quadrants were situated over 28+ °C SST of the Gulf Stream whereas the rear quadrants were near or partially over 26.5 – 27.5°C SST near the cold pool boundary. Vertical transects taken through the composite shown in Figure 3.13 captured the extremely shallow depth of precipitation structure inside 100km from storm center and demonstrate the structural implications of enhanced air-sea enthalpy flux encountered by the forward quadrants of the storm at this time.

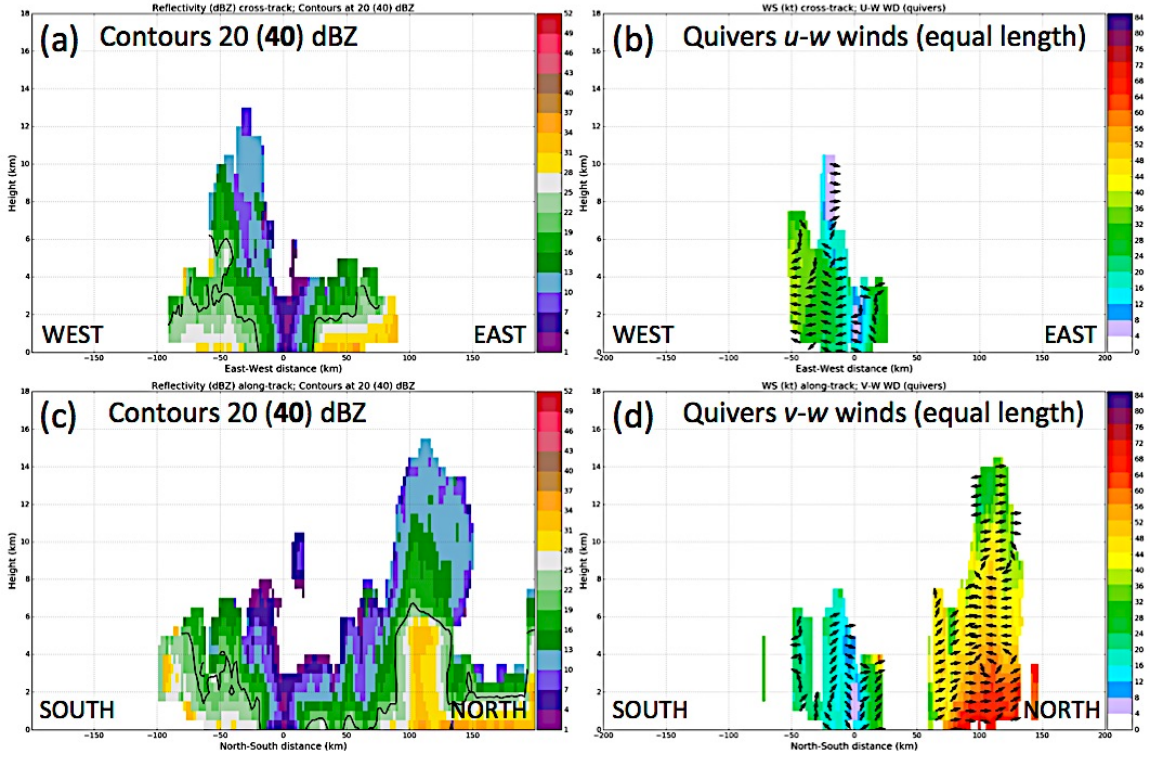


Figure 3.13 Vertical transects of (a,c) radar reflectivity and (b,d) horizontal wind taken through the composites in Figure 3.12. Slices in (a) and (b) are taken across-track, whereas (c) and (d) are taken along-track. Contours in (a) and (c) denote 20 (light to moderate) and 40 (strong to intense) dBZ. In (b) and (d), quivers depict the indicated 2D winds.

In Figure 3.13a,b the west-east transect shows extremely shallow radar reflectivity spread along  $\sim 75$ km to either side of the storm center. Maximum reflectivity values of near 30 dBZ associated with this stratiform precipitation are confined to lower than 3km. Vertical motions are limited, and winds were directed radially outward west of the storm center along this slice. The aforementioned impact of Ophelia's inner core region being subjected to opposite ocean environments can be seen from 3.13c,d that shows the south-north (along track) slice. Surface air parcels are situated above cooler SST and less air-sea enthalpy flux toward the left of the slice, whereas they encounter a more favorable energy source towards the right of the slice. A 6km-deep tower of moderate reflectivity returns is situated just outside 100km. Compared with the precipitation structure at this

distance south of the storm center, this feature is deeper, stronger, and more continuous. Near the surface ~60-75km north of the storm center, air parcels rise and converge along a vertical line between 4-8km. The narrow vertical structure with continuous 30 +dBZ radar reflectivity values ending in anvil-like feature near 6km reaffirm that this feature is convective. Ophelia's precipitation structure from the composite is dominated by a single radially inward rainband that likely was serving as the eyewall with the inner core of the storm vacant. Flight-level and SFMR surface wind measurements from a NOAA WP-3D flight leg September 12 2000 UTC – 2050 UTC pass through the radially inward southwestern and northeastern rainband segments. Traversing the entire storm, the profiles of wind and flight-level radar reflectivity shown in Figure 3.14 help discern whether this outer rainband was dynamically serving as an eyewall or not, regardless of Ophelia's tropical storm maximum wind intensity at this time.

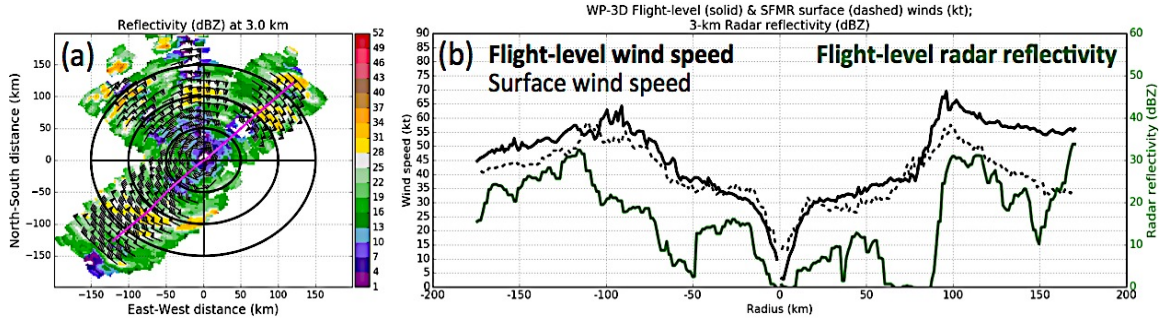


Figure 3.14 (a) NOAA HRD 3D DA flight-level radar reflectivity composite as in Figure 3.3a, overlaid with the aircraft flight path September 12 2000 UTC – 2050 UTC (b) Profile of aircraft flight-level wind (kt, solid black), SFMR surface wind estimate (kt, dashed black), and flight-level radar reflectivity from the composite (dBZ, green).

In panel (b) of Figure 3.14, the flight-level and surface wind profiles are shown to be nearly overlapping for most of the flight path indicated by the magenta line in 3.14a. Inside the RMW on either side (near 100km), wind speed quickly decreases (~30-40 kt over ~25-40km along radius and the vortex has a bowl-like structure. Flight-level radar

reflectivity along the flight path demonstrates the weakness of the inner core region (< 20 dBZ within 100km) and support for precipitation and convection at more distant radii. Both RMRs occur outside of the flight level and surface RMW, with the radar reflectivity profile matching the structure of the SFMR surface winds more closely than the winds at flight-level. Collectively, the combination of a less axisymmetric precipitation structure, extremely weak inner core, and adjacent along-path flight-level radar reflectivity and surface wind speed maxima indicate Ophelia's discrete outer rainband structure was likely being supported by near-surface convergence of nonlocal moisture.

Despite surviving the cold pool interaction, Ophelia remained a tropical storm (60 kt MWSP) for 36h continuously beginning September 12 0600 UTC. Ophelia's large circulation and its interaction with the upper ocean provide a dynamic and thermodynamic explanation for the storm's failure to intensify from September 12 0600 UTC – September 13 1800 UTC. In an early study by Shapiro and Willoughby (1982), spin-up of tangential winds directly interior of the RMW was found to occur as a result of convection near the RMW. More recently, Hong et al. (2012) showed the rate of change of the tangential wind speed favors intensification when the heating source (e.g. convection) is inside the RMW. Observational work using Doppler radar has corroborated the tendency for convective bursts within the RMW of intensifying TCs (Rogers et al. 2013; Corbosiero et al. 2005). As a large TC with a weak inner core, Ophelia's strongest wind speeds were far from the storm center. Similar to a rotating figure skater attempting to pull heavy weights towards their body from a fully extended position, this structure promotes resilience in the vortex (contraction is hard). Within this larger RMW is an inertially stable region, buffered from large-scale environmental

factors (e.g. vertical wind shear, dry air, etc.) that may impact the storm's intensity. From Figures 3.12 and 3.14 however, convection is absent within the RMW due to previous interaction with the cold pool, and the RMR is situated outside the surface RMW on both sides of the vortex (see Figure 3.14b). Aside from upwelling in slow-moving TCs, wind-stress induced shear mixing of the upper ocean was found to be the dominant cause of SST cooling induced as a forced response to hurricane passage over the ocean (both mechanisms account for ~85-90% of cooling; e.g. Price, 1981). Hence, even though Ophelia is not a hurricane during this stage the wind field is large and can exert wind stress over a large area of the ocean surface. To quantify the role of the expanded storm's winds on the upper ocean, RMW and an integrated kinetic energy (IKE; Powell & Reinhold 2007) quantity were computed from the HRD H\*WIND analysis product surface winds approximately every 6h from September 9 0130 UTC – September 14 2230 UTC. Storm-relative snapshots between September 12 1330 UTC and September 13 1930 UTC are shown in Figure 3.15. A timeseries showing the simultaneous evolution of RMW (km) and IKE (TJ,  $10^9$  kJ) is shown in Figure 3.16.

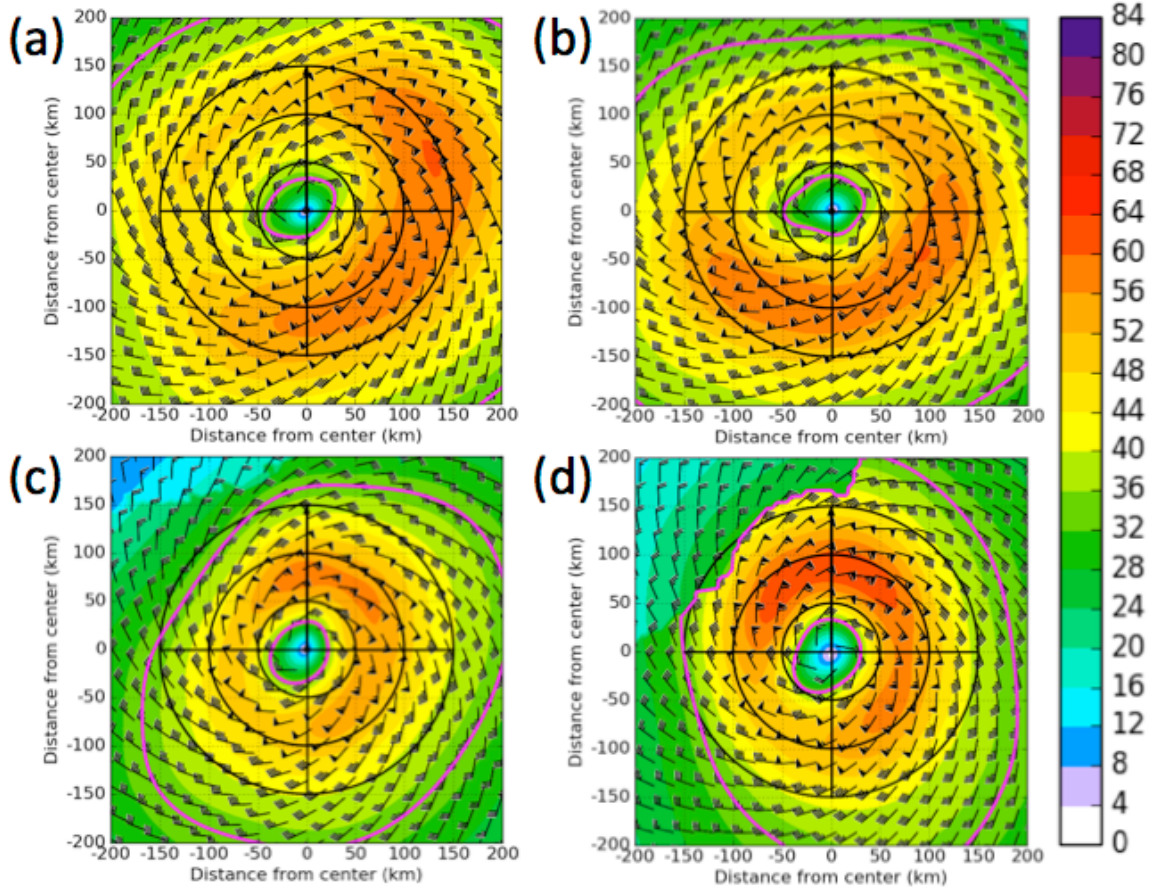


Figure 3.15 HRD H\*WIND analysis surface wind (kt, colors and barbs) in storm-relative space for September 12 (a) 1330 UTC (b) 1930 UTC and September 13 (c) 0730 UTC (d) 1930 UTC. The magenta contour denotes 34kt (tropical storm force) winds.

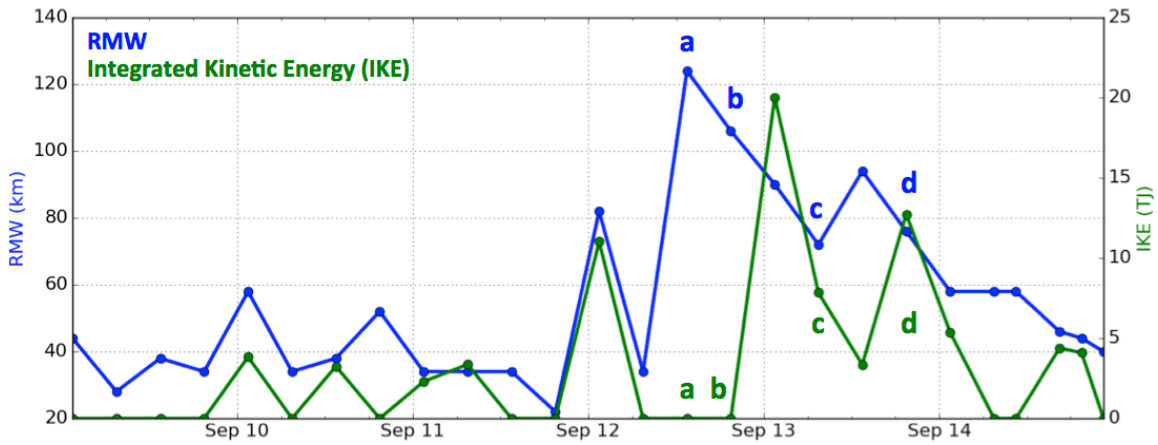


Figure 3.16 Timeseries of H\*WIND-derived radius of maximum wind (RMW) (km, blue) and integrated kinetic energy (TJ, green) as in Powell and Reinhold (2007) for September 9 – 15. Letters correspond to the times in Figure 3.15.

Integrated kinetic energy (IKE) was computed using polynomial least-squares regression fits relating TC wind radii to IKE as determined in Powell and Reinhold (2007; PR07). The method of PR07 accounts for storm size and maximum wind speed in the computations as follows:

$$IKE_{25-40} = -23.3 + 0.05R_{18} + 0.245R_{26} \quad (3.1a)$$

$$IKE_{41-54} = -25.7 + 0.4V_{MS} - 0.022(V_{MS} - 56.9)^2 + 0.085R_{33} + 0.097R_{max} \quad (3.1b)$$

$$IKE_{55} = -28.96 + 0.43V_{MS} + 0.036(V_{MS} - 64.9)^2 + 0.024R_{33} \quad (3.1c)$$

where Equation 3.1a is the IKE corresponding to the 25-40 ms<sup>-1</sup> range, 3.1b is the IKE corresponding to the 41-54 ms<sup>-1</sup> range, and 3.1c is the IKE corresponding to the 55+ ms<sup>-1</sup> range. V<sub>MS</sub> is the maximum wind speed, and subscripted R quantities (e.g. R<sub>18</sub>) correspond to the radius of the indicated wind speed (ms<sup>-1</sup>). Values less than zero are given value of 0 IKE. All three quantities are summed together and weighted according to the range of wind speeds (i.e. 25-40, 41-54, and 55+) as given in Equation 3.2 below:

$$IKE = 1IKE_{25-40} + 6IKE_{41-54} + 30IKE_{55} \quad (3.2)$$

Computed in this manner, the integrated quantity of kinetic energy describes the energy dissipated from the TC surface circulation and the subsequent impact on the upper ocean temperature structure as a function of the maximum surface wind speed of the TC, and the radial extent of winds of different intensity. Snapshots of Ophelia's surface wind as deduced from the H\*WIND analysis are provided for four times in Figure 3.15, with panel (a) depicting the enlarged circulation on September 12 1330 UTC and panel (d) depicting the surface winds on September 13 1930 UTC, shortly after Ophelia re-strengthened to hurricane intensity over the Gulf Stream. The timeseries of RMW and IKE in Figure 3.16 shows that between September 12 0600 UTC and September 13 1800

UTC, when Ophelia re-strengthens to hurricane intensity, changes in IKE lag by 6-12h behind the RMW. Additionally, IKE remains nonzero and achieves two local maxima (19 and 12.5 TJ) between September 12 1930 UTC and September 14 0130 UTC, during which time Ophelia had a large wind field (e.g. September 12 1930 UTC – September 13 0730 UTC) or was intensifying (e.g. September 13 1330 – September 14 0430 UTC). These two influences on the IKE can be seen in the 4-panel evolution of surface winds in Figure 3.15 as the large but initially weaker wind field contracts and then intensifies late on September 13. From aircraft and satellite observations of Ophelia’s structure and upper ocean environment, complete collapse of the inner core and expansion of the RMR beyond the RMW occur in response to previous strong cooling and reduced inner core air-sea enthalpy flux. Furthermore, occurrence of the global maximum in IKE after the largest expansion of the RMW but prior to Ophelia regaining hurricane intensity demonstrates the size of the circulation may have more bearing on the TC impact on the ocean than the maximum wind speed. A recent idealized study by Halliwell et al. (2015) found large, slow storms to be more sensitive to the ocean heat potential (TCHP) changes from SST cooling. Since the TC and ocean are coupled in nature and exert feedbacks, a converse argument follows sensibly that the ocean will be more sensitive to a greater region of TC wind stress forcing that it experiences over a longer period of time (due to TC speed). Slow propagation of an enlarged Ophelia may be responsible for the satellite observed expansion of 25.5 – 26.5°C SST from the cold pool behind its track after September 12 0600 UTC (see Figure 3.17), due to wind stress induced upper ocean mixing.

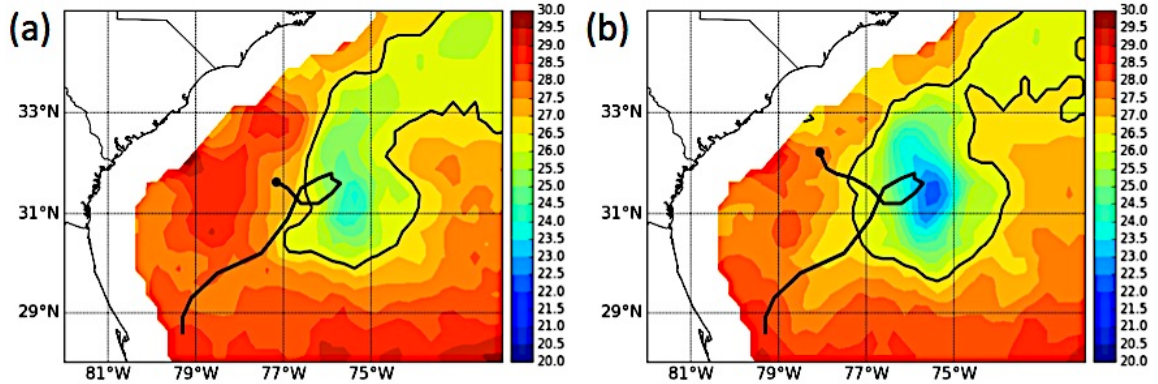


Figure 3.17 TRMM AMSR-E merged daily SST overlaid with Ophelia’s storm track since September 9 0000 UTC for (a) September 12 (center position 1600 UTC) (b) September 13 (center position at 1600 UTC). The black solid contour denotes 26.5°C.

### 3.5 New symmetric eye forms and convection reinvigorates over the Gulf Stream

In the previous two sections, RAINEX observations described air-sea interaction induced structure and intensity changes in Ophelia – collapse of the inner core and expansion of the storm afterwards. These structure changes were consistent with an eyewall replacement cycle. Morphed microwave (MIMIC; Wimmers & Velden 2007) brightness temperature imagery from the University of Wisconsin/CIMSS archive given in Figure 3.18 shows the evolution of Ophelia’s secondary eyewall feature from September 12 1200 UTC – September 13 1200 UTC. This feature transitions from large and axisymmetric to a more rainband like structure before contracting and becoming more intense. Hence, in this section we describe recovery of mature TC structure and consolidation of Ophelia’s convection into a new eyewall over the Gulf Stream.

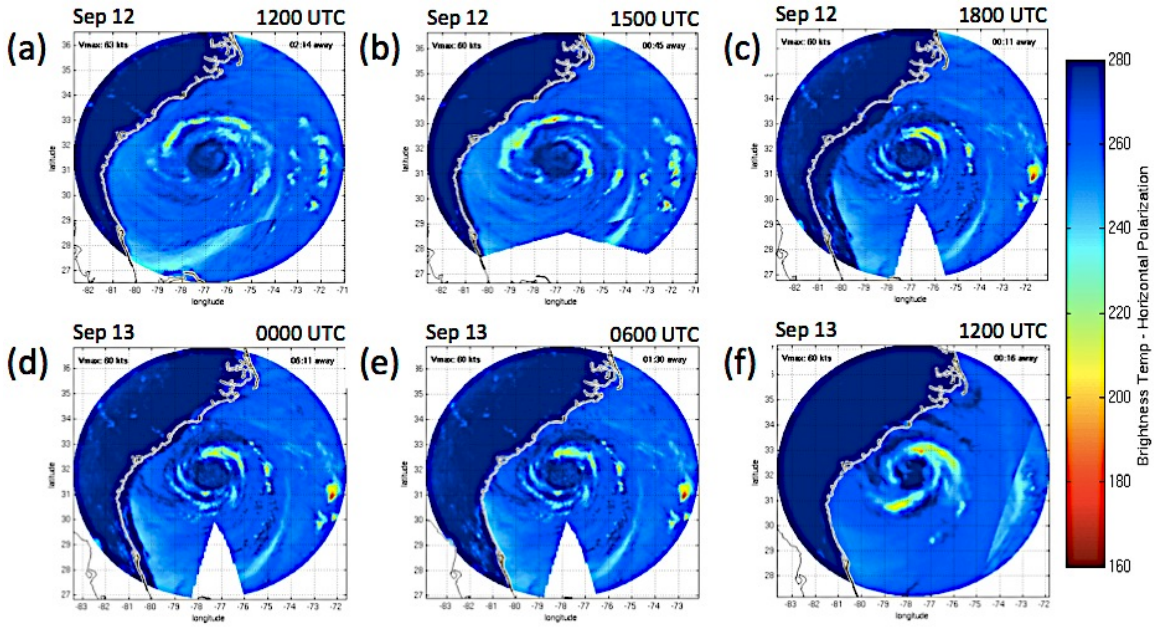


Figure 3.18 University of Wisconsin/CIMSS Morphed Microwave (MIMIC; Wimmers and Velden, 2007) microwave brightness temperature imagery September 12 1200 UTC – September 13 1200 UTC for the indicated times in (a) – (f).

Flight-level 3D DA radar reflectivity and wind composites for September 13 2000 UTC - September 14 0010 UTC provided in Figure 3.19 capture the return of inner core precipitation and improved organization in the storm structure as a whole. By this time, according to NHC best track MWSP, Ophelia was a hurricane. A large band of 60-70 kt winds nearly 50km wide is seen in the forward left and rear left quadrants of the storm (see Figure 3.19c). Several narrow bands of strong winds were also observed in the forward right quadrant beyond 100km, but are distinctly separated from the large band closer to the storm center. Both regions of strong winds are associated with precipitation structures featuring moderate to intense convective 30-40 dBZ reflectivity returns. The azimuthal averaged flight-level RMW and RMR are 88km and 68km respectively, with 45 and 80% coverage (see panels (b) and (d)). Relative position of the RMR inside the RMW at this time is favorable for intensification, and indeed Ophelia had reached

hurricane status September 13 1800 UTC. These composites show two notable signatures indicating Ophelia was evolving into a mature TC late on September 13: very weak/absent radar reflectivity and winds at storm center, and distinctly separate eyewall and rainband structures. Low reflectivity and wind regions separate the eyewall from the rainbands at  $\sim$ 100km and  $\sim$ 150km distance in the forward right quadrant. Vertical transects in Figure 3.20 show Ophelia's improved symmetry and depth as well as the outward sloping structure of the new eyewall.

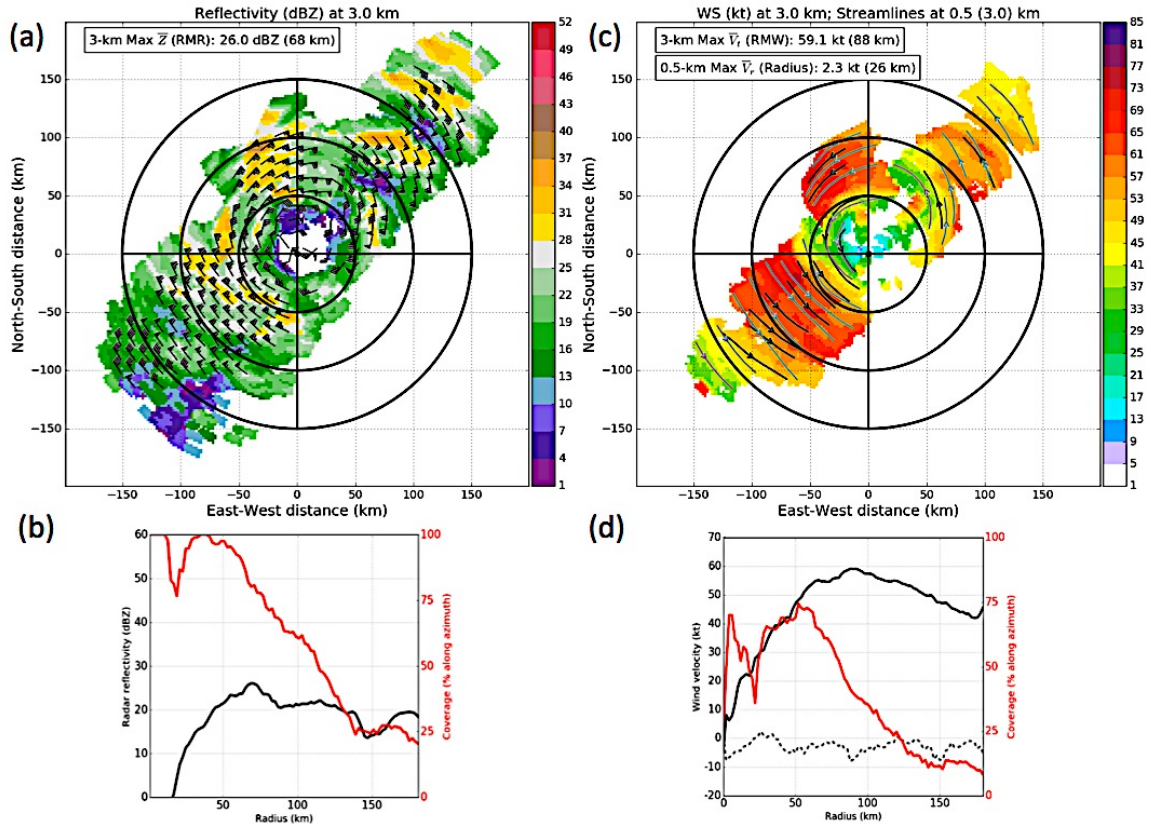


Figure 3.19 (a) NOAA HRD 3D Doppler Analysis (3D DA) composite flight-level radar reflectivity (dBZ) for September 13 2000 UTC – September 14 0010 UTC. Azimuthal average flight-level RMR and value at that radius are indicated at top left. Black wind bars give the flight level wind (kt) (b) Azimuthal average radar reflectivity profile (dBZ, black) and composite coverage along each azimuth (% along azimuth, red) (c) Same as (a) except for flight-level wind speed. Black (grey) streamlines are at 0.5km (3 km) altitude. (d) Same as (b) except for tangential wind speed (kt, solid black) and radial wind speed (kt, dashed black).

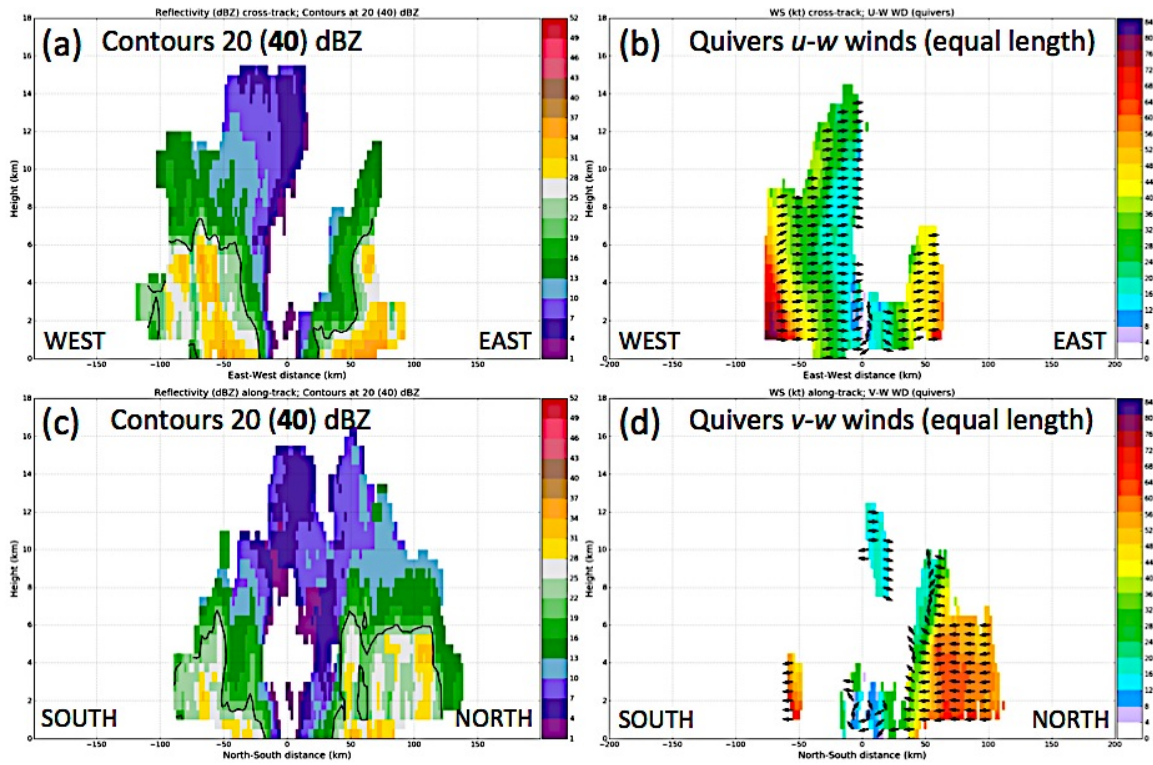


Figure 3.20 Vertical transects of (a,c) radar reflectivity and (b,d) horizontal wind taken through the composites in Figure 3.19. Slices in (a) and (b) are taken across-track, whereas (c) and (d) are taken along-track. Contours in (a) and (c) denote 20 (light to moderate) and 40 (strong to intense) dBZ. In (b) and (d), quivers depict the indicated 2D winds.

Similar to the organizing stage, Ophelia's vertical structure was relatively deep (~12-14km) with weaker reflectivity and winds above 6-8km. Maximum radar reflectivity returns were 30-35 dBZ and situated 50-70km from the storm center, sloping outward with height in most cases with a total depth between 5-6km. The precipitation includes both convection and adjacent stratiform rain, as was observed in the large rainband that preceded Ophelia's eyewall forming on September 10. Due to gaps in the wind vertical slices it is difficult to trace surface convergence or upward motion throughout the depth of the circulation, however, there are strong cross-eyewall gradients along both directions in the wind speed on each side of a gradually outward-sloping eye. Furthermore, inflow on the northern side of the storm turns upward between 4km and 8km depth along the

inner edge of the eyewall (near ~50km from storm center). Organization of the precipitation from 50 – 125km north of center suggests an interior convective tower and flanking region of continuous stratiform rain consistent with typical/mature TC structure. TRMM AMSR-E merged daily SST from September 13 depicted a narrow strip of 27+ °C waters nearly parallel to the coast of South and North Carolina (see Figure 3.21). This region of warm SST corresponds with an undisturbed western portion of the Gulf Stream. Ophelia turned north-northwest and then north, propagating parallel to the Gulf Stream beginning September 13 1200 UTC. From CIMSS MIMIC and 3D DA aircraft composites, Ophelia’s precipitation and circulation structure were observed to contract/consolidate and intensify as the storm moved fully over the warm, deep Gulf Stream with the inner core sufficiently distanced from the previously induced cold pool.

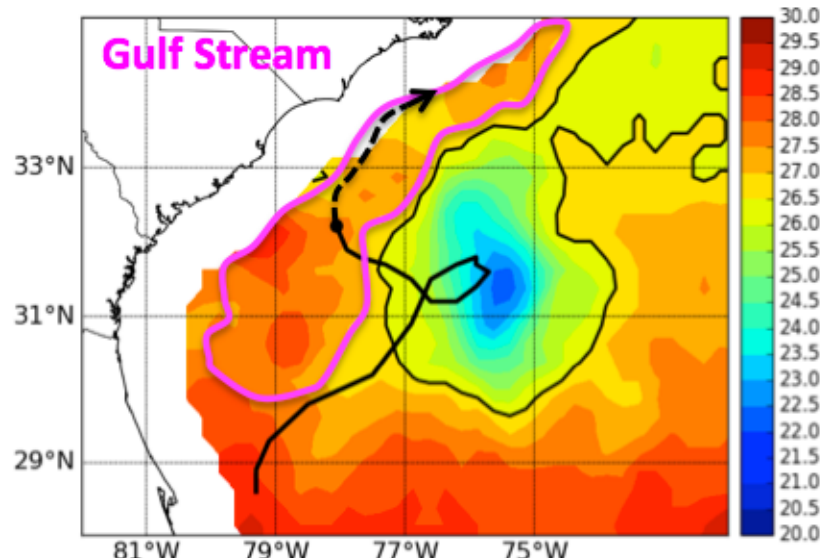


Figure 3.21 TRMM AMSR-E merged daily SST overlaid with Ophelia’s storm track since September 9 0000 UTC for September 13 (center position 1600 UTC). The black solid contour denotes 26.5°C. The magenta contour outlines the undisturbed Gulf Stream west and northwest of Ophelia’s cold pool. The dashed arrow extending beyond the black dot follows Ophelia’s future storm track through September 15 0000 UTC.

To emphasize the location of intense convection relative to a changing RMW, two panels depicting the NOAA HURSAT 85 GHz polarization corrected (PCT) microwave brightness temperature (BRT, degrees K) are shown in Figure 3.22. Polarization corrected brightness temperature at this frequency is sensitive to ice-phase hydrometeors present in strong and intense convection, with colder brightness temperatures corresponding to deeper and stronger precipitation. Panel (a) shows the PCT BRT for September 12 1230 UTC, when the RMW was  $> 100$  km from storm center and Ophelia was situated between its cold pool and Gulf Stream. Panel (b) shows PCT BRT 36h later, once the storm had fully moved over the Gulf Stream. The surface RMW had contracted to  $\sim 70$ km and intense convection associated with the newly forming eyewall is seen near and inside this radius. The RMW remains small and the maximum wind speed levels off by September 14 1200 UTC while moving parallel to the North Carolina coast, effectively completing Ophelia's recovery and the air-sea interaction facilitated eyewall replacement cycle.

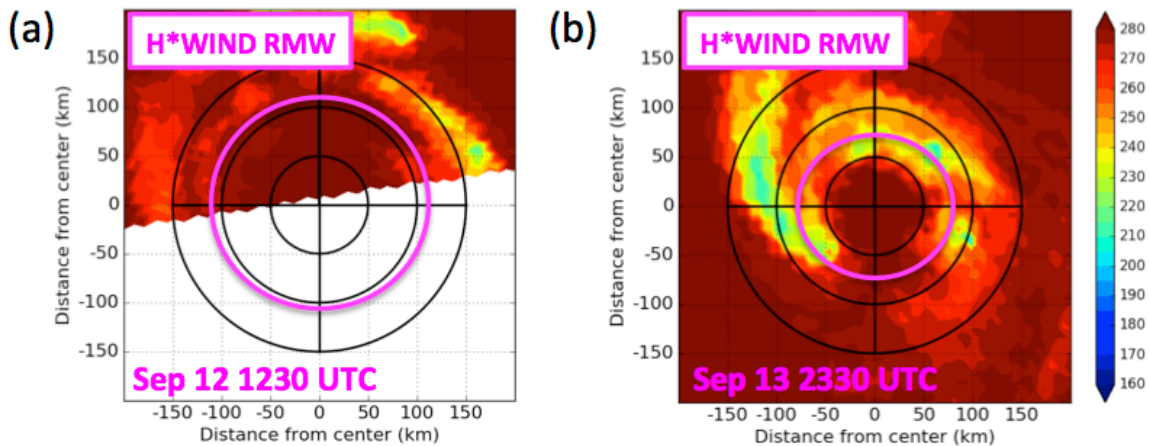


Figure 3.22 NOAA HURSAT 85 GHz polarization corrected (PCT) microwave brightness temperature (BRT, deg K) indicating moderate to intense convection at (a) September 12 1230 UTC (b) September 13 2330 UTC. The H\*WIND-derived RMW is indicated by the magenta circle.

### 3.6 Summary

Hurricane Ophelia was a complex tropical cyclone with substantial structure changes throughout its life cycle. Intensity by comparison was remarkably less variable. Four stages in Ophelia's life cycle were described by observations based on the physical processes involved in the structure and intensity changes. Grouped by stage, we use contoured-frequency by altitude (CFAD, Yuter & Houze 1995b) diagrams of 3D DA radar reflectivity to summarize the storm's structure at each stage.

In Stage 1, Ophelia's intensity oscillated between tropical storm and hurricane strength. Vertical wind shear caused asymmetry but the precipitation was moderately strong, deep, and coherent. Stage 1 CFAD was constructed from 3D DA observations from 0200-0400 and 1400-1700 UTC September 9 when Ophelia was near hurricane intensity (Figure 3.23). The profile has frequency peaks at 8 (12) kilometers consistent with observed echo top height for moderate (weak) reflectivity returns. A sharp horizontal gradient is evident near 5-kilometers consistent with the presence of stratiform bright band and the profile slopes towards 30-35 dBZ returns. Coexistence of convective and stratiform precipitation features and the diagonal slope reflect an organizing storm with mesoscale convective structures.

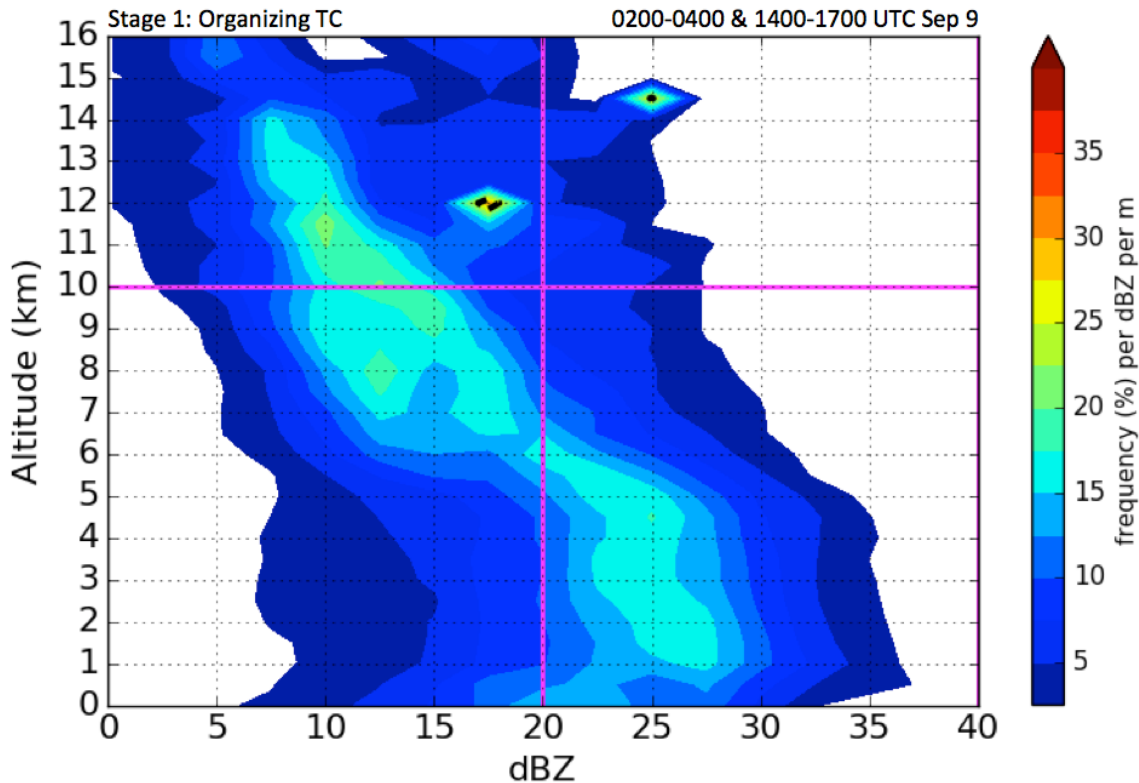


Figure 3.23 NOAA HRD 3D DA contoured-frequency by altitude diagram for radar reflectivity during Stage 1, when Ophelia was near hurricane intensity. Radar reflectivity (dBZ) is given on the x-axis, altitude is given in on the y-axis. Colors reflect frequency (%) per dBZ per meter. The black dashed contour indicates 25% per dBZ per meter.

Storm-induced upwelling was the dominant physical process in Stage 2. During this stage, Ophelia experienced the most weakening in its wind intensity. Interacting with its' cold wake, the storm structure was asymmetric and shallow. Precipitation structure was diverse, but was primarily stratiform within the inner core. The Stage 2 CFAD grouped observations from 1800 – 2207 UTC September 11 during the cold-pool interaction and collapse of the storm's inner core. This profile is shown in Figure 3.29. The weakest reflectivity maxima are notably shallower than Stage 1, reaching 9 – 10 kilometers, and there are no strong reflectivity returns ( $\geq 35$  dBZ). Low-level frequency maxima are uniform between 1 – 5 kilometers but weaker (20 – 25 dBZ) and the profile spread extends much further toward 0 dBZ than in Stage 1. Ophelia's cold-pool

interaction drastically altered the storm structure and was responsible for the largest decrease in wind intensity observed.

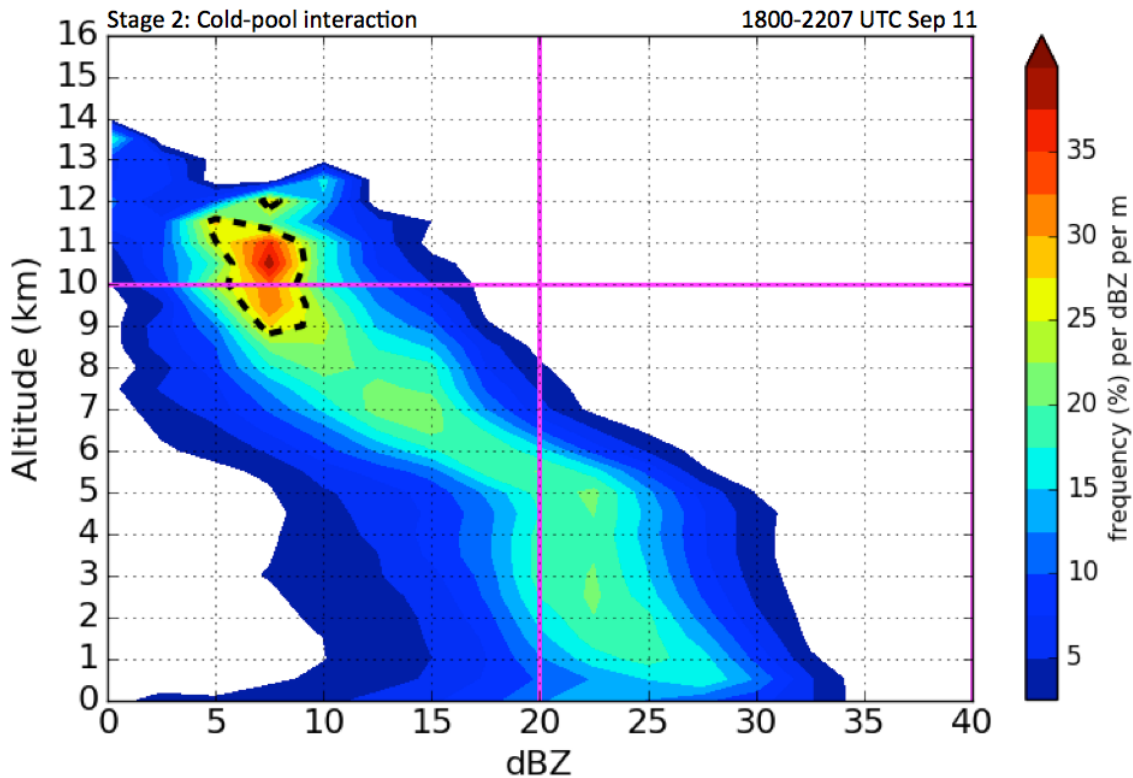


Figure 3.24 Same as 3.23, but for Stage 2, when Ophelia was interacting with its' cold pool.

During Stage 3, Ophelia's inner-core has fully collapsed and the circulation expands. Wind intensity is approximately constant, near 60 knots throughout a 36-hour period between 0600 UTC September 12 – 1800 UTC September 13. Stage 3 includes the CFADs from September 11 2300 – September 12 2300 UTC (Figure 3.25). Moderate convective returns have 10% frequency or less below 2-kilometers, and there are no 40+ dBZ returns. Low-level reflectivity frequency slants rightward from 20 to 25 dBZ between 1-2 kilometers, consistent with stronger precipitation being present but very shallow. Weak returns compose the majority of this profile, and maximize in frequency near 8 kilometers at 10 dBZ.

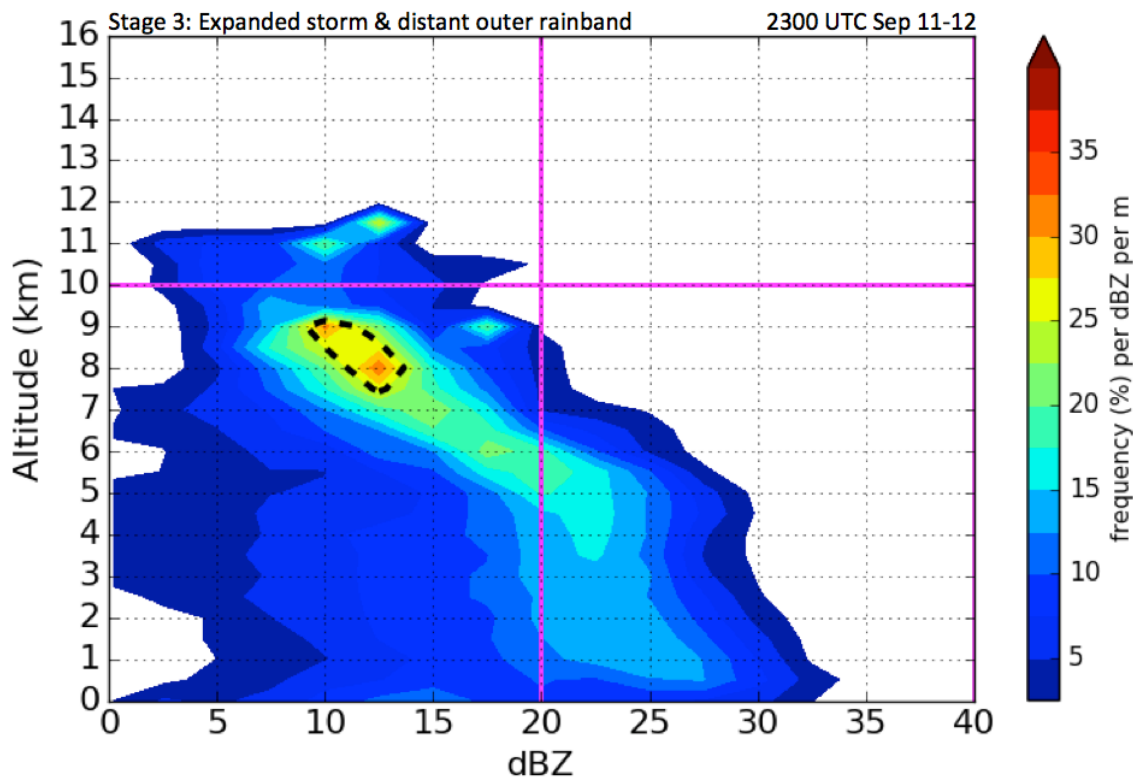


Figure 3.25 Same as 3.23, but for Stage 3, when Ophelia was in a structural transition phase, with an expanded circulation and distant outer rainband.

Finally, in Stage 4 the storm recovers. CFADs from September 13 2000-2300 UTC are grouped to make the profile in Figure 3.31. Similar to Stage 1, the slope is diagonal, with larger reflectivity values at lower altitudes. Reflectivity frequencies are substantially more compact here than the prior two stages. Nearly 35-dBZ returns reach 5-kilometers, while the entire profile extends to ~12-13 kilometers. Reflectivity frequency bulges rightward between 4-5 kilometers, similar to the stratiform bright band signature from the Stage 1 CFAD. Once again, convective and stratiform returns cohabit in a mature profile.

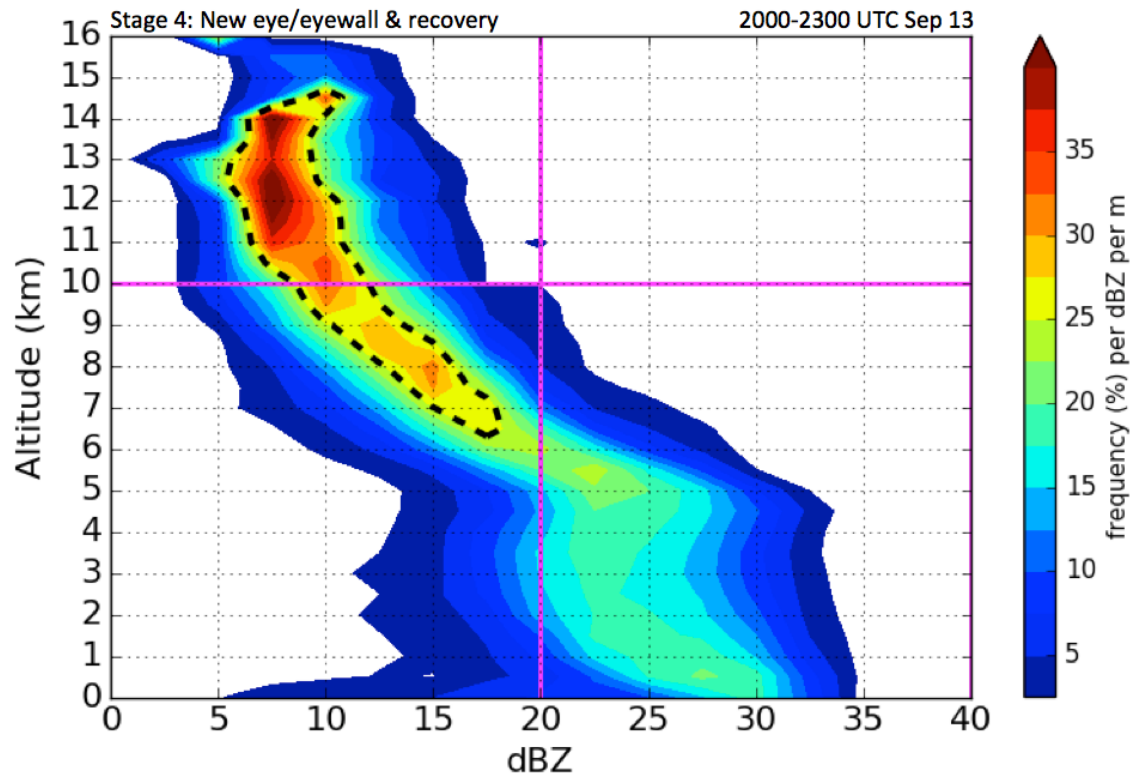


Figure 3.26 Same as 3.23, but for Stage 4, when Ophelia recovers over the Gulf Stream.

## Chapter 4: Impact and Role of Air-Sea Interaction in Hurricane Ophelia (2005)

### 4.1 Model verification

#### 4.1.1 Track and intensity

A comparison of model simulated storm tracks with best track positions from the National Hurricane Center (NHC) is shown in Figure 4.1. Both model simulations were initialized without vortex relocation at the NCEP final analysis (FNL) position for September 9 0000 UTC.

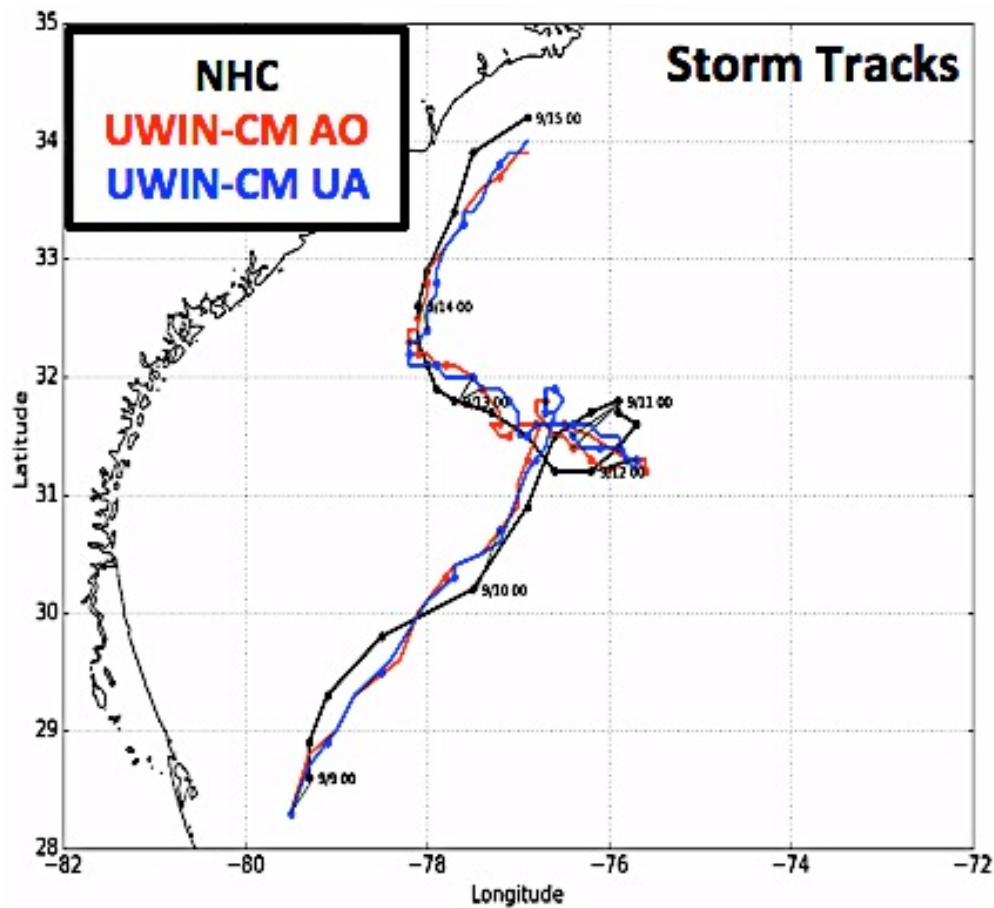


Figure 4.1 NHC best track (black) and UWIN-CM UA (blue), AO (red) simulation storm tracks shown every 6h from September 9 – 15.

The model storm track positions and forward speed were quite similar to each other throughout the six-day period of the simulation. Both storms accelerated eastward early

on, followed by a correction crossing the observed position towards the north between 1800 UTC September 9 and 0000 UTC September 10. For the next 12 hours, both storms moved northeastward almost parallel and slightly west to the observed storm. By 1200 UTC September 10, model storm tracks hesitated and made a small loop before turning to the east-northeast, beginning the anti-cyclonic loop phase. Best track shows the loop is broad (~ 85-kilometers), however the model storms execute a substantially tighter loop moving towards the east-southeast for 18 hours before turning back towards the west-northwest. Model timing compares reasonably with the duration of the observed loop, with both storms generally decelerating toward 0000 UTC September 11 and then accelerating once turning toward the west approximately 24h later. The simulated storms turn parallel to the Gulf Stream late on September 13, lagging behind best track until accelerating toward the northeast 1200 UTC September 14.

Although the track is similar between the two simulations, the model noticeably over-intensifies the simulated storms. Figure 4.2 shows maximum wind speed (MWSP, kt) compared with NHC best track intensity. Between model simulations, the intensities are very similar through September 10 1200 UTC. After this time however, the atmosphere-ocean coupled (AO) simulation intensity evolution was much closer to best track. Weakening begins in AO around September 11 0000 UTC, and this trend continues for 24h in response to interaction with its storm-induced cold pool. By contrast, UA intensifies by 20 kt over the same period. A second period of strengthening begins in UA September 12 1200 UTC, with maximum wind speed increasing by more than 30 kt over the following 24h (rapid intensification per NHC definition; RI). After moving away from the cold pool, the AO storm recovery is delayed until September 13 0000 UTC,

after which AO turned northward parallel to the Gulf Stream. Recovery began 18h too early and was more intense than the real Ophelia (25 kt in AO vs. 15 kt from best track), however the coupling to the ocean in AO still provides the more realistic simulation of Ophelia's intensity.

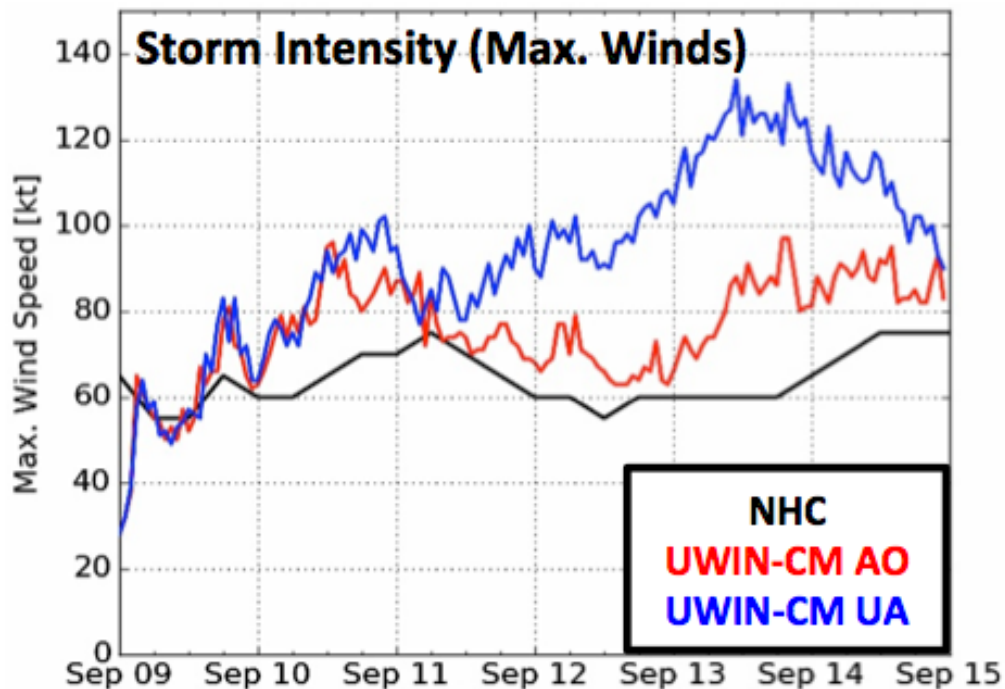


Figure 4.2 NHC best track (black) and UWIN-CM UA (blue), AO (red) simulation maximum wind speed intensity shown every 6h from September 9 – 15.

#### ***4.1.2 Storm environment and structure***

Storm structure at any given time – that is, the structure of the circulation (winds) and precipitation, are often a reflection of the intensity a storm possesses. As mentioned in Chapter 1, intensity changes frequently occur in association with changes to the storm structure. Best track observations show Ophelia's intensity did not change by a large magnitude throughout its life. For example, between September 9 0000 UTC - September 15 0000 UTC, the difference between the maximum and minimum MWSP was 20 kt (vs. Katrina (100 kt), August 27 – 30, 2005). RAINEX observations have shown Ophelia's

structure however, changed substantially over that same period (see Chapter 3). Evolution of the model simulated TC structure can be traced to the state of the atmosphere-ocean environment and any subsequent internal changes to the storms. In this section, we describe changes in the large-scale environment vertical wind shear and sea-surface temperature (SST) observed by RAINEX and compare them to the model simulation environment. Model structure changes are evaluated in the four life stages described in Chapter 3, with particular emphasis on the impact of coupling and relative importance of an interactive ocean in each stage.

Model deep-layer (200 – 850 hPa) vertical wind shear (DLS) was calculated over a 200–800 km annulus from storm center similar to SHIPS. A timeseries of the SHIPS DLS (from archive in ‘x’s and real-time GFS analyses, every 6h) along with the UWIN-CM DLS from September 9 0000 UTC – September 15 0000 UTC are given in Figure 4.3.

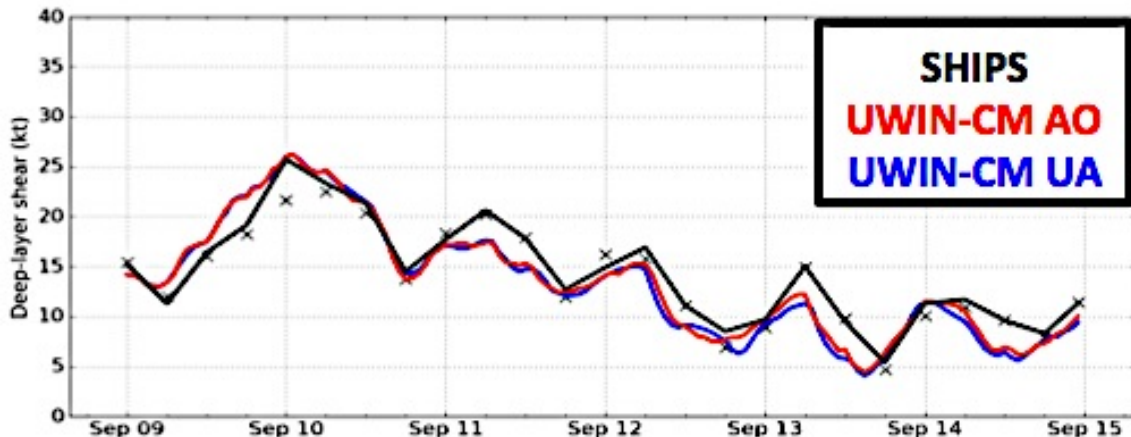


Figure 4.3 SHIPS (black) and UWIN-CM UA (blue), AO (red) simulation deep-layer (200 – 850 hPa) wind shear using the 200 – 800 km annulus from storm center. SHIPS shear was provided every 6h in both developmental (archive) data and from the FNL (real-time GFS) analysis, September 9 - 15.

From Figure 4.3, SHIPS and UWIN-CM DLS agree quite well throughout the simulation period for both uncoupled atmosphere (UA) and atmosphere-ocean coupled (AO)

experiments. During Ophelia's asymmetric, organizing stage (September 9 0000 UTC – September 10 1800 UTC) shear was generally moderate (~12-25 kt). Shear magnitude exceeded 20 kt for an 18-24h period beginning September 9 1200 UTC. From September 11 0000 UTC onward, the maximum shear magnitude steadily decreased. Based on this timeseries, UWIN-CM produces a similar large-scale atmospheric state regardless of coupling, and the atmosphere becomes increasingly favorable for intensification in time. Model intensity does not however, reflect that occurs in both simulations. In fact, AO MWSP falls by 15 kt even though DLS decreases from 22 to 14 kt September 10 1200 UTC – September 10 1800 UTC (Figure 4.2). Weakening intensity despite lessening shear implicates the ocean environment has unfavorably changed in the AO simulation. In both model simulations, UWIN-CM uses HYCOM SST at the initial model time. A critical distinction when coupling is permitted (AO) is the evolution of that initial SST, whereas in the UA simulation SST is fixed in time and the ocean is a passive component to the model environment. Figure 4.4 shows the evolution of TRMM AMSR-E merged daily SST and UWIN-CM SST from September 9 0000 UTC to September 10 1800 UTC as snapshots. In-situ 0.6m water temperature measurements from NDBC 41010, nearby Ophelia's center September 9 0000 UTC – 1800 UTC, are given in panel (c).

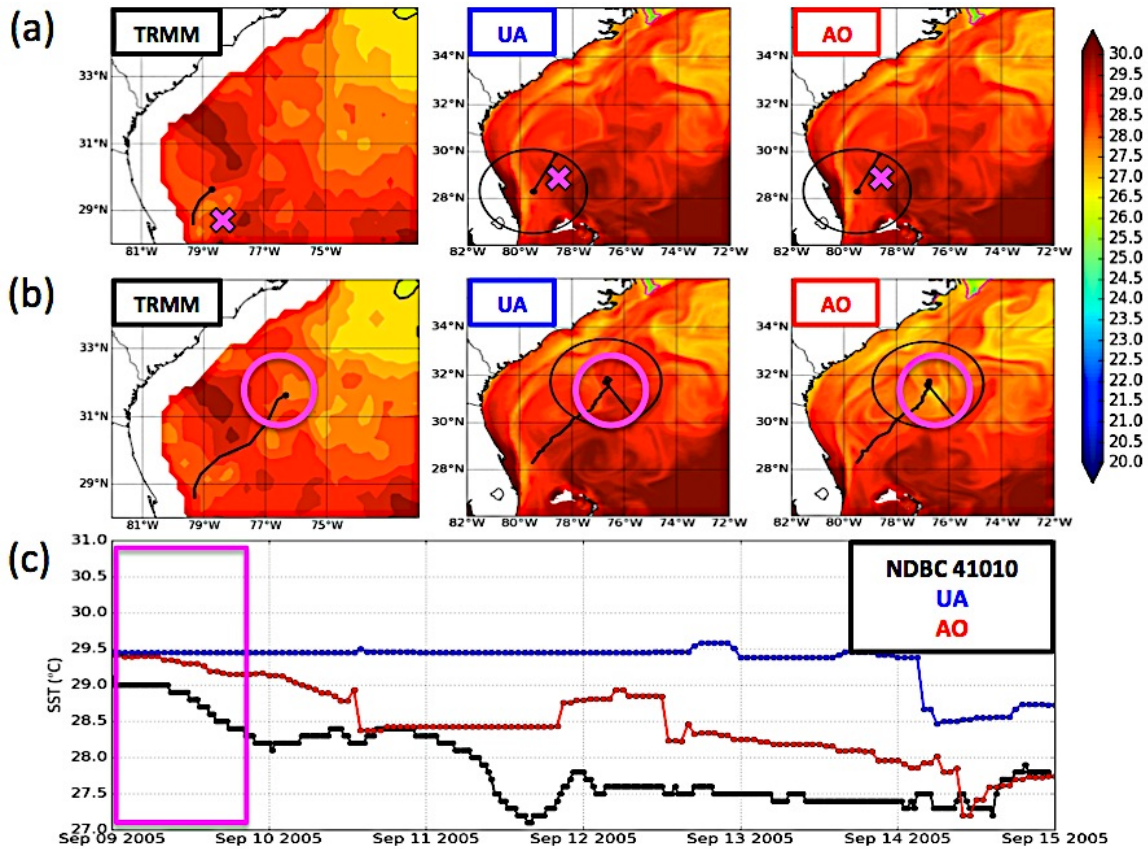


Figure 4.4 (a) TRMM, UWIN-CM UA, and UWIN-CM AO SST (deg C) with NDBC 41010 position indicated by the magenta ‘x’ (b) as in (a) but for September 10 1800 UTC (c) NDBC 41010 storm-relative SST from the buoy (black), UWIN-CM UA (blue), and UWIN-CM AO (red).

Over the same period the real and model simulated storms were subjected to moderate wind shear, they were propagating over moderately warm 28-29°C SST. Buoy near-surface temperatures were similar, 28.25 – 29°C over the 18h period (magenta box in 4.4c). The timeseries of buoy measurements clearly demonstrates the initial UWIN-CM SST was 0.5°C too warm, though the coupling does result in a reasonable rate of cooling in the AO model simulated buoy SST. By September 10 1800 UTC, SST near Ophelia’s center was cooler (~27°C) as the storm began to induce a cold pool. This feature is denoted for comparison by the magenta circles in Figure 4.4. At the time the ocean is

starting to cool in the AO simulation, the time-constant SST in the UA simulation shows SST near the storm center exceeds 28°C. As both model simulated storms have very similar track, speed, and shear, the presence of persistent warm SST in UA is likely responsible for the disparity in model simulated storm intensity beginning September 10 1800 UTC. Model simulated structure is compared to NOAA WP-3D aircraft observations in Figure 4.5. The observed composites include the September 9 1258 UTC – 1353 UTC and 1412 – 1440 UTC legs from RAINEX RF04. Model comparisons use September 9 1300 UTC and 1400 UTC output. Both sets of composites are storm-relative.

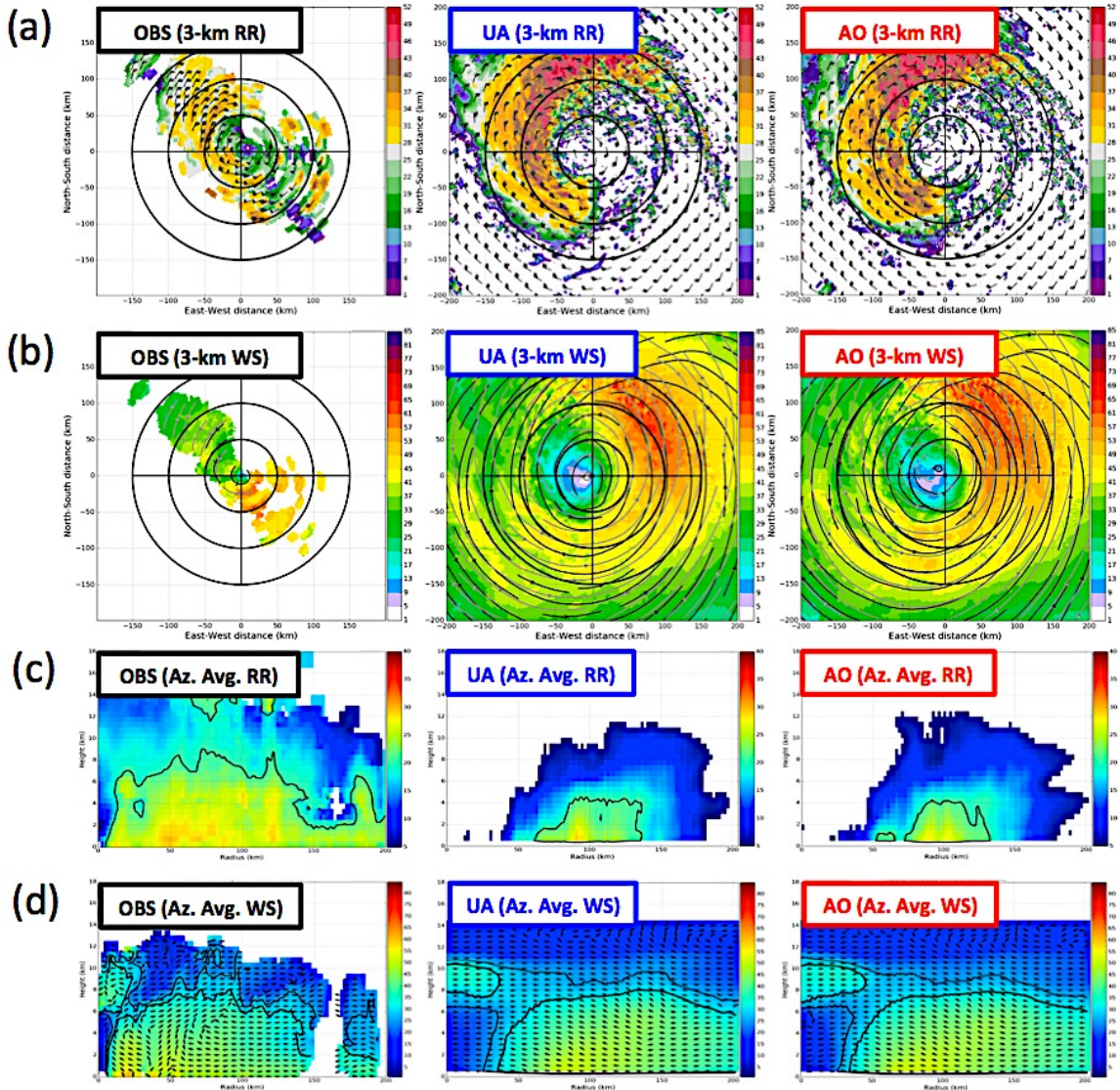


Figure 4.5 (a) NOAA WP-3D 3D Doppler Analysis flight-level composite (Sep 9 1258 UTC – 1440 UTC) and UWIN-CM storm-relative composite (1300 UTC – 1400 UTC) radar reflectivity (b) same as (a) but for wind speed (c) corresponding observed and model 2D azimuthal average radius-height radar reflectivity and (d) wind speed. In rows (a) and (b), black circles show distance every 50km. Flight-level wind barbs are overlaid on reflectivity figures, 0.5 (black) and 3km (grey) streamlines are overlaid on wind figures. For the 2D azimuthal average diagrams, reflectivity is contoured at 20 and 40 dBZ. Wind speed is contoured at 25 and 30 kt. Quivers show the radial-vertical velocity with length normalized to unity.

In general, the placement of structural features in the model-simulated storms is similar by quadrant to Ophelia's actual structure. The asymmetric and incoherent structure of the

observed storm was reasonably represented in the model simulations. A large rainband composed of adjacent convection and stratiform precipitation, with stronger precipitation in the forward-left and rear-left quadrants is evident, and the strongest winds occur on the opposite side of the storm albeit about a clearly distinguishable low-wind center. Precipitation is too intense (45+ dBZ) and too broad (40+ dBZ spanning 40-50 km wide) in the rainband in both model-simulated storms. Although the model simulated storms had been integrated for only ~13h at this time, there are some small differences in their structure. The AO simulation captures a thin extension of the rainband into the rear-right quadrant. This feature was observed to be the predecessor to an eyewall briefly acquired by Ophelia late on September 9, and was absent in UA. Furthermore, the UA simulation has a more symmetric eye with the wind minima nearer to the storm-relative center position. Azimuthal average radar reflectivity and wind speed comparisons are given in panels (c) and (d). The observed and model-simulated circulations across the entirety of the storm have similar depth (30-kt up to 7-8 km), but show less organized vertical motion than the observed composite. Absence of this vertical motion in the azimuthal average is likely a consequence of the averaging itself, as the model simulated storms have comparatively much less convection in their rear-right and forward-right quadrants. The differences in precipitation structure between model simulations are far more obvious. In both the observed storm and AO simulation, reflectivity returns reach to relatively deep heights (~12 + km) but are weak above 6-8 km. Additionally, UA simulation echo top height gradually increases outward from the storm center, producing a stadium-like shape consistent with a more symmetric TC.

By September 11 0600 UTC, the model storm intensities had diverged from one another. While the UA storm began the first of two periods of intensification, AO was weakening due to interaction with its' induced cold pool. Figure 4.6 shows the TRMM AMSR-E merged daily SST and UWIN-CM SST for September 11 1800 UTC and September 12 0300 UTC. Based on the pre-cold pool SST (see Figure 4.4), SST cools by a range of 2.5 - 4 (1 - 3) °C beneath the observed (AO) storm through September 12 0300 UTC.

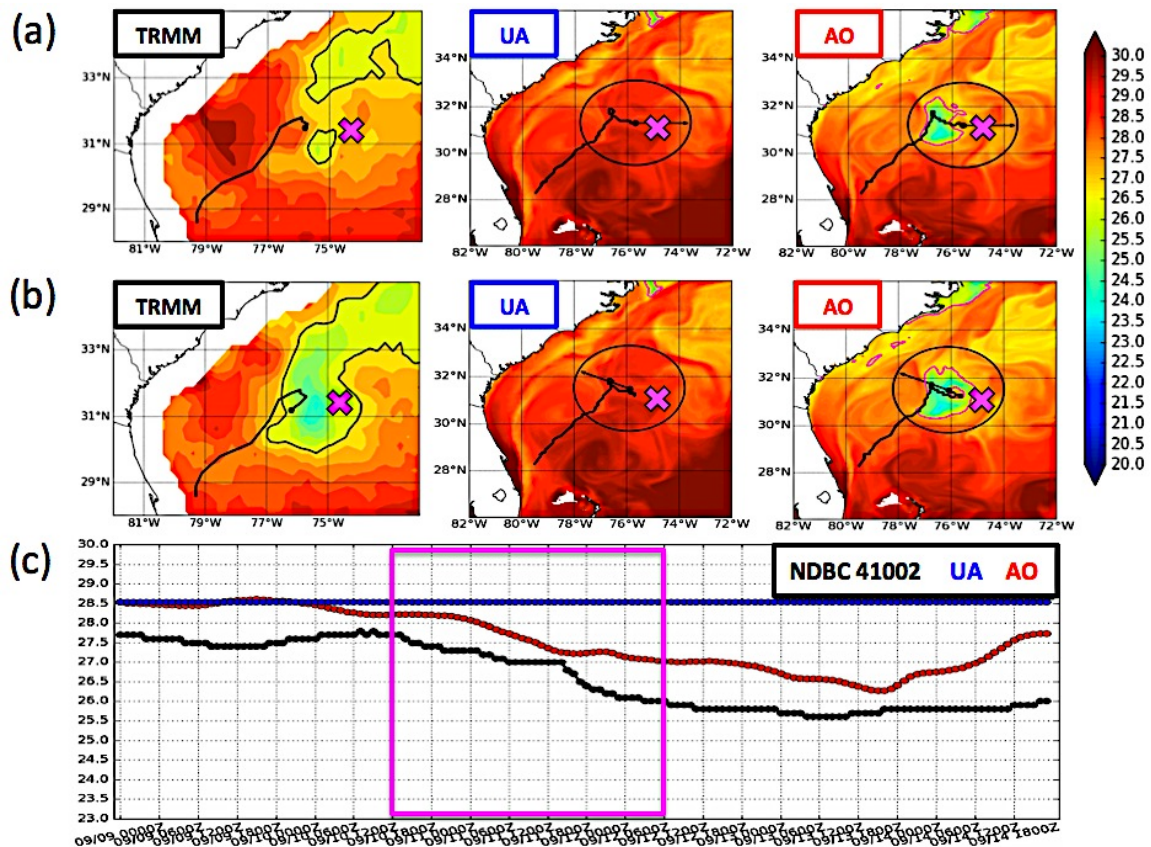


Figure 4.6 (a) TRMM, UWIN-CM UA, and UWIN-CM AO SST (deg C) with NDBC 41002 position indicated by the magenta 'x' (b) as in (a) but for September 12 0300 UTC (c) NDBC 41002 storm-relative SST from the buoy (black), UWIN-CM UA (blue), and UWIN-CM AO (red). The black line shows the storm track to the indicated time. The black dot is situated at the storm center. The black circle denotes 200km radius.

In Figure 4.6, the magenta ‘x’ shows the position of NDBC 41002. This buoy was situated on the eastern periphery of the observed and AO simulation cold pool. NDBC 41002 near-surface water measurements show cooling of  $\sim 1.5^{\circ}\text{C}$  occurs directly over the buoy site. Comparing the model simulated buoy temperatures, a warm bias is again observed with the ocean initially  $\sim 0.9^{\circ}\text{C}$  warmer than the NDBC buoy measurement for September 9 0000 UTC. The cooling rate in the coupled (AO) ocean is however, agrees very well with the observed cooling rate during Ophelia’s interaction with the cold pool (September 10 1800 UTC – September 12 0600 UTC) while passing west of the buoy.

While Ophelia induced and propagated over its cold pool, RAINEX RF05 aircraft Doppler radar observed pronounced asymmetry and weakening of precipitation in the inner core region within  $\sim 75$  km from storm center. Flight-level observed radar reflectivity and winds show an asymmetric eyewall feature encircled by a second ring of strong winds and banded precipitation near 100 km from Ophelia’s center. Model simulated structure is compared to these aircraft observations in Figure 4.7 to elucidate whether a double eyewall structure consistent with early-stage EWRC occurs. Observed composites include the September 11 1617 UTC – 1703 UTC and 1736 – 1818 UTC legs from RAINEX RF05. Model comparisons use September 11 1600 UTC and 1700 UTC output.

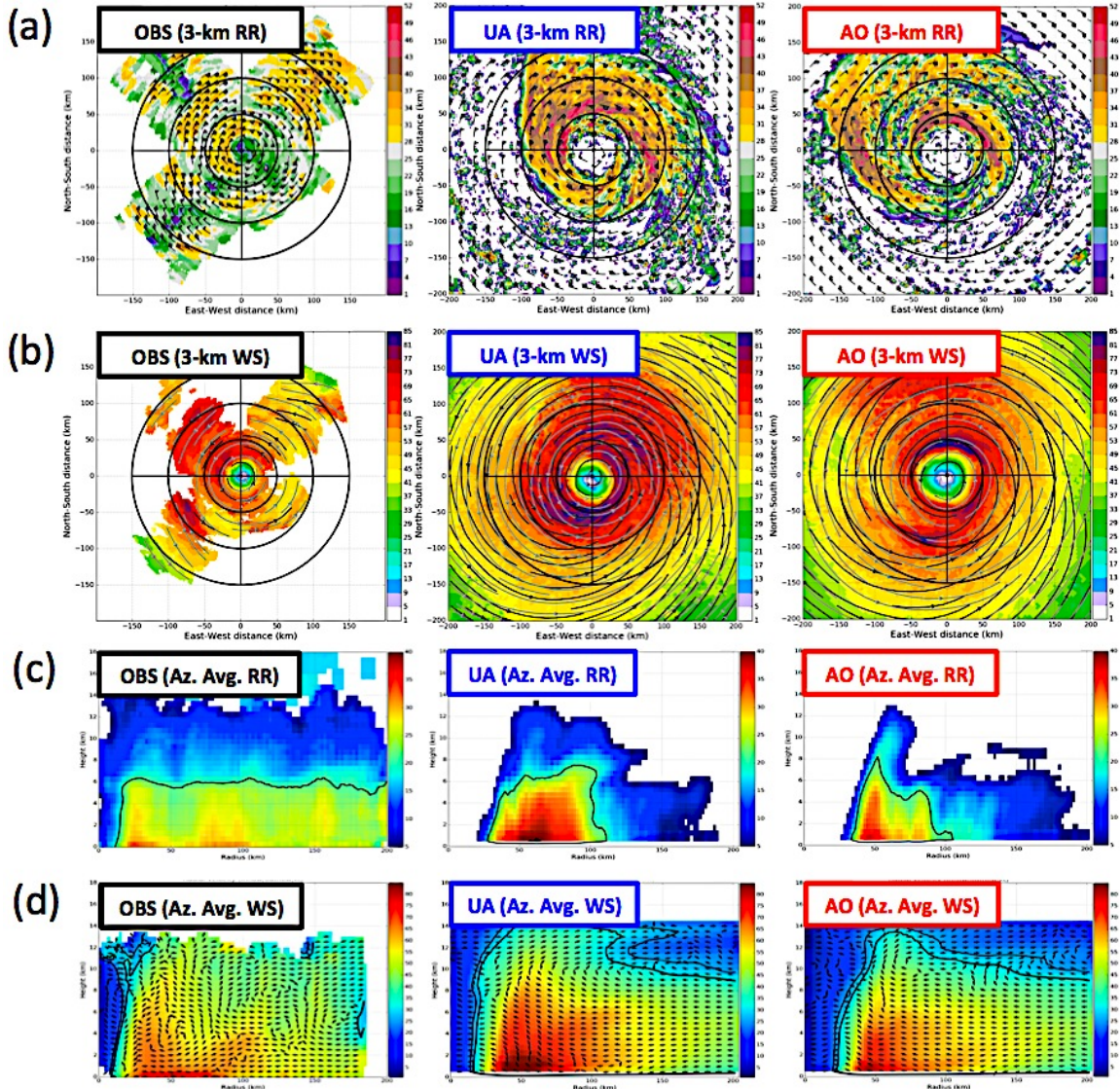


Figure 4.7 (a) NOAA WP-3D 3D Doppler Analysis flight-level composite (Sep 11 1616 UTC – 1812 UTC) and UWIN-CM storm-relative composite (1600 UTC – 1700 UTC) radar reflectivity (b) same as (a) but for wind speed (c) corresponding observed and model 2D azimuthal average radius-height radar reflectivity and (d) wind speed. In rows (a) and (b), black circles show distance every 50km. Flight-level wind barbs are overlaid on reflectivity figures, 0.5 (black) and 3km (grey) streamlines are overlaid on wind figures. For the 2D azimuthal average diagrams, reflectivity is contoured at 20 and 40 dBZ. Wind speed is contoured at 25 and 30 kt. Quivers show the radial-vertical velocity with length normalized to unity.

Flight-level radar reflectivity in the UA simulation shows a strong, radially compact precipitation structure composed of a single eyewall-rainband feature with 35-50 dBZ returns anti-cyclonically wrapping around a symmetric rain-free storm center. Having

reasonably captured the cold pool and being coupled to an interactive ocean, precipitation in the AO simulation is azimuthally asymmetric and more rapidly weakens away from the 50-km radar of maximum reflectivity (RMR) than does UA. Furthermore, radar reflectivity is substantially weaker (15-25 dBZ) over a majority of the AO rear-right quadrant. This lower-reflectivity region, about 25-30 km wide, can be traced anti-cyclonically around the storm center and is separating the inner and outer precipitation features. Flight-level wind shows a similar gap in the AO simulation, with a thin ring of 40 – 60 kt winds approximately 100 km from storm center separating two regions of 65 – 80 kt winds. While both UA and AO model storms have a well-defined, symmetric low-wind center (vertical wind shear < 20 kt, see Figure 4.3), precipitation and vortex structures are more aligned by quadrant and radius in the AO simulation. Specifically, the double maxima in precipitation and wind speed are approximately collocated (flight-level RMWs at 48, 116 km; RMRs at 48, 120 km). Azimuthal average transects show the vertical structure of precipitation across the entirety of the model simulated TCs was distinctly different between UA and AO. In the observed storm, extent of 20-dBZ returns has shallowed to 6 km and two regions of stronger reflectivity can be seen near 25 and 80 km that are separated by a low-reflectivity region. The AO azimuthal average reflectivity transect is similarly shallow (20 dBZ reaching 4-6 km except directly at inner RMR) captures these features well, although the model storm has a larger eye and overintensifies the precipitation relative to aircraft Doppler observations. By contrast, a double maxima in precipitation is not observed in the UA transect, and the region of high reflectivity returns is broad and too intense (> 10 dBZ stronger than maximum return in AO). As seen in UA on September 9, the depth of strongest reflectivity again increases in

height outward from the storm center. In the time between flights on September 9 (1258 UTC - 1440 UTC) and September 11 (1616 UTC – 1812 UTC), the UA simulated TC becomes considerably more symmetric, cross-eyewall precipitation and wind gradients sharpen, and the azimuthal average flight-level maximum wind speed increases by 25 kt (~12.5 m/s), consistent with overintensification of UA MWSP on September 11. Over the same period, although the AO simulated storm has strengthened by 15 kt, coupling to an interactive ocean produces a shallower, weaker, more asymmetric TC. The collapsing inner core and secondary horizontal rain and wind maxima seen by the RAINEX/IFEX aircraft associated with incipient EWRC (see e.g. Willoughby, 1982) are captured only by the AO simulation.

On September 12 by 0600 UTC, Ophelia had turned northwest toward the Gulf Stream and was situated between a warm ocean ahead and cool ocean behind in the axis of the storm's heading. The position and intensity of the Gulf Stream and cold pool as observed by TRMM AMSR-E merged daily SST and produced by UWIN-CM are shown in Figure 4.8.

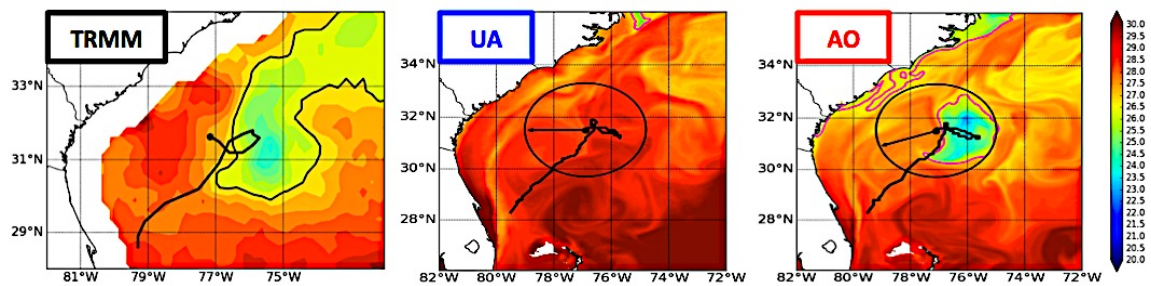


Figure 4.8 (a) TRMM, UWIN-CM UA, and UWIN-CM AO SST (deg C) for September 12 0600 UTC. The black contour in TRMM (magenta in AO) indicates 26.5°C. The black line shows the storm track to the indicated time. The black dot is situated at the storm center. The black circle denotes 200km radius.

Structure of the cold pool behind Ophelia compares well between satellite and the AO simulated ocean, each having minimum SST in the range 23 – 24°C. Ahead of the storms lies warm undisturbed Gulf Stream SSTs from TRMM (AO) of 27.5 – 28.5 (27.5 – 28) °C. Meanwhile, the UA simulated ocean possesses > 28°C SSTs over a large region near the storm's position. Between September 12 0600 UTC and September 12 1800 UTC, the UA simulated TC begins the second of two intensification periods that occurred after September 11 0000 UTC. Over the 24h after September 12 1200 UTC, the UA TC undergoes a rapid intensification (RI) event (NHC definition) during which the storm contracts. Inversely, the AO TC has expanded following interaction with the cold pool. Figure 4.9 shows the model simulated storm structure compared against aircraft observations late on September 12. Observed composites include the September 12 2006 UTC – 2046 UTC, 2132 UTC – 2212 UTC, and 2248 – 2326 UTC legs from RAINEX RF05. Model comparisons use September 12 2000 UTC - 2200 UTC output.

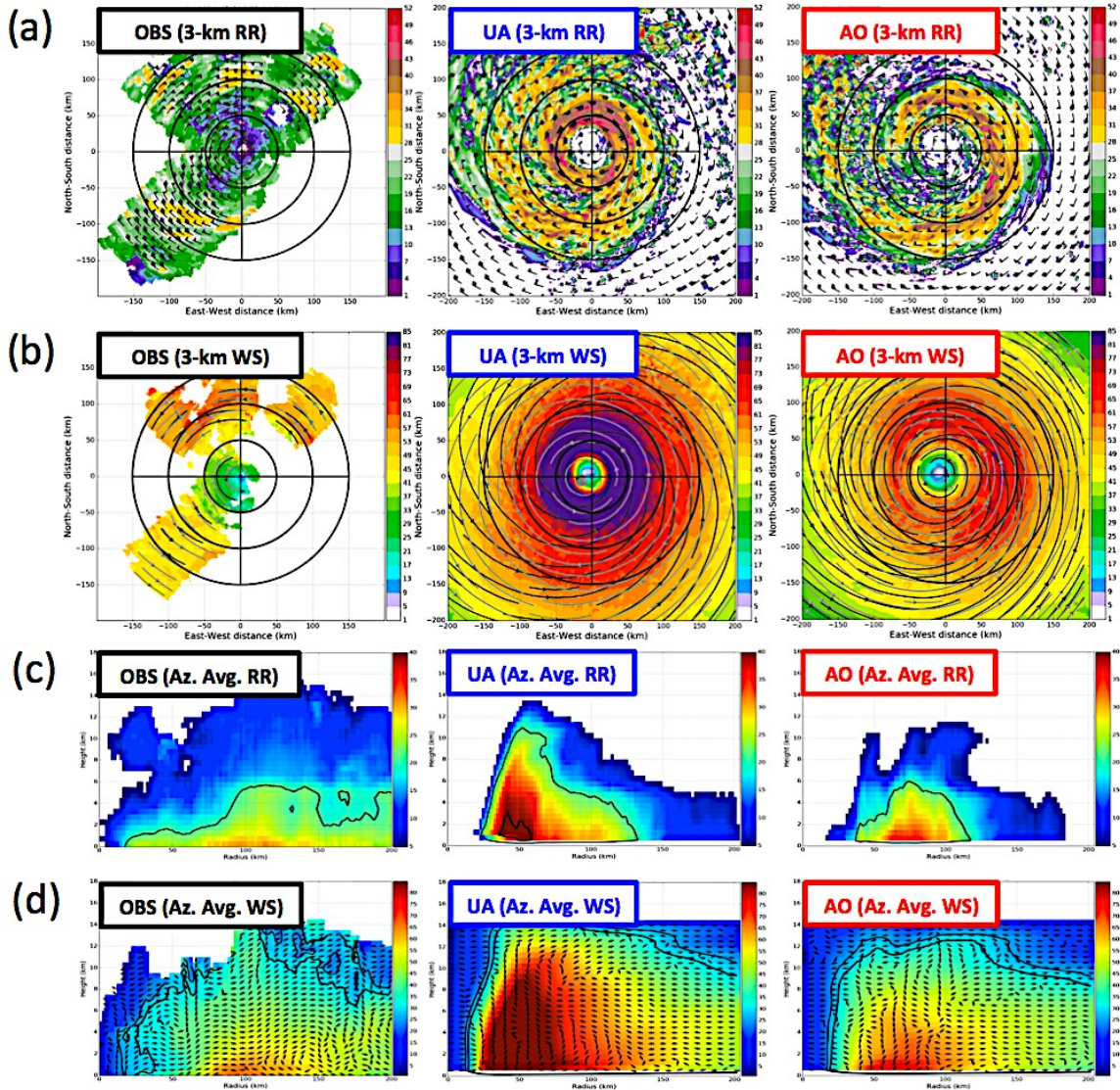


Figure 4.9 (a) NOAA WP-3D 3D Doppler Analysis flight-level composite (Sep 12 2006 UTC – 2338 UTC) and UWIN-CM storm-relative composite (2000 UTC – 2200 UTC) radar reflectivity (b) same as (a) but for wind speed (c) corresponding observed and model 2D azimuthal average radius-height radar reflectivity and (d) wind speed. In rows (a) and (b), black circles show distance every 50km. Flight-level wind barbs are overlaid on reflectivity figures, 0.5 (black) and 3km (grey) streamlines are overlaid on wind figures. For the 2D azimuthal average diagrams, reflectivity is contoured at 20 and 40 dBZ. Wind speed is contoured at 25 and 30 kt. Quivers show the radial-vertical velocity with length normalized to unity.

Based on the observed structure seen by the aircraft on September 11 and 12 (left columns in 4.7, 4.9), Ophelia's RMW had expanded from 48 to 108 km while at the same time the storm shallowed further over the ~24h between those two series of flights.

Convection was completely absent within 75 km of storm center and maximum wind speeds in the inner core were 30 – 45 kt (~15 - 30 kt lower than during September 11 1616 UTC – 1812 UTC flight legs). Further collapse of inner core precipitation (though incomplete) and weaker wind speeds inside 75 km is captured in the AO simulated storm. The radially inward rear-left rainband segment and clusters of discrete convection over the forward quadrants observed to be the strongest precipitation features in the weaker, larger storm in this stage are also evident in the coupled (AO) TC. As a gross juxtaposition, the UA simulated storm has a symmetric and extremely strong wind field within 75 km and sharp cross-eyewall gradients in all quadrants. A similarly symmetric ring of convection (40 – 50 dBZ returns) is situated near the RMW (50 km). Intense reflectivity returns signifying convection can also be seen within this radius, as is commonly observed in intensifying real-world TCs (Rogers et al. 2013; Corbosiero et al. 2005). Azimuthal average radar reflectivity and wind speed though more intense than the real storm, show the substantial difference in vertical structure and depth clearly in rows (c) and (d). The AO simulated storm structure is shallow (20 dBZ returns reach 2-6 km, though stronger thresholds are considerably shallower), with the RMR at 80 km just outside the flight-level RMW (76 km). Within this RMW, there are no azimuthal average reflectivity returns that exceed 3 km height. Differences in the size of the AO and observed storm and location of the RMW are in part a consequence of the re-intensification over the Gulf Stream occurring 18h prematurely. In spite of model differences, absence of convection within the inertially stable region enclosed by the RMW and its relative position inside the RMR do not favor intensification and are seen in both the real Ophelia and the AO model simulation in response to TC-ocean

interaction. Ophelia achieves its maximum intensity in both model simulations while moving over the Gulf Stream on September 13. The UA TC, which has intensified almost continuously throughout the six-day simulation period, reaches 130 kt intensity by September 13 1800 UTC. Comparatively the AO TC attains maximum winds of 95 kt after recovering from the structure changes and weakening facilitated by interaction with its self-induced cold pool. The TRMM AMSR-E merged daily SST and UWIN-CM SST are given below in Figure 4.10 for September 13 1200 UTC. All storms are beneath 27 – 28°C SST during this stage.

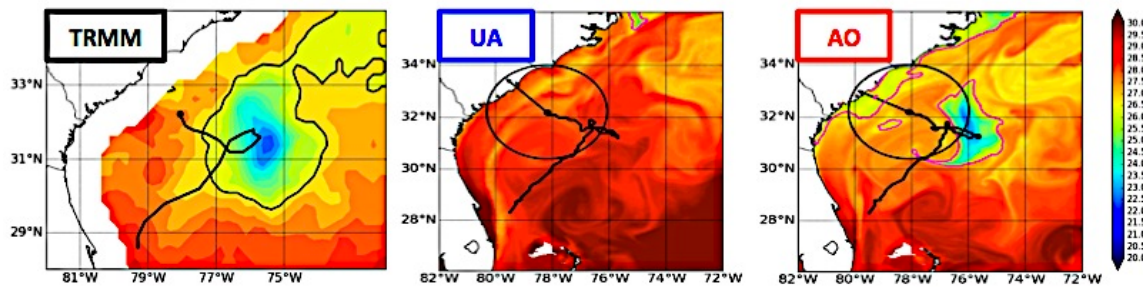


Figure 4.10 (a) TRMM, UWIN-CM UA, and UWIN-CM AO SST (deg C) for September 13 1200 UTC. The black contour in TRMM (magenta in AO) indicates 26.5°C. The black line shows the storm track to the indicated time. The black dot is situated at the storm center. The black circle denotes 200km radius.

Once again over warm SST as in the organizing phase, and with low DLS in the environment (< 12 kt, see Figure 4.3), Ophelia's structure recovered. Distinct eyewall and rainband precipitation features and strong cross-eyewall wind gradients associated with the recovery are shown in Figure 4.11 along with model structure comparisons. Observed composites include September 13 2000 UTC – 2056 UTC, 2110 UTC – 2207 UTC, and 2207 – 2300 UTC flight legs. Model comparisons use September 13 2000 UTC - 2300 UTC output.

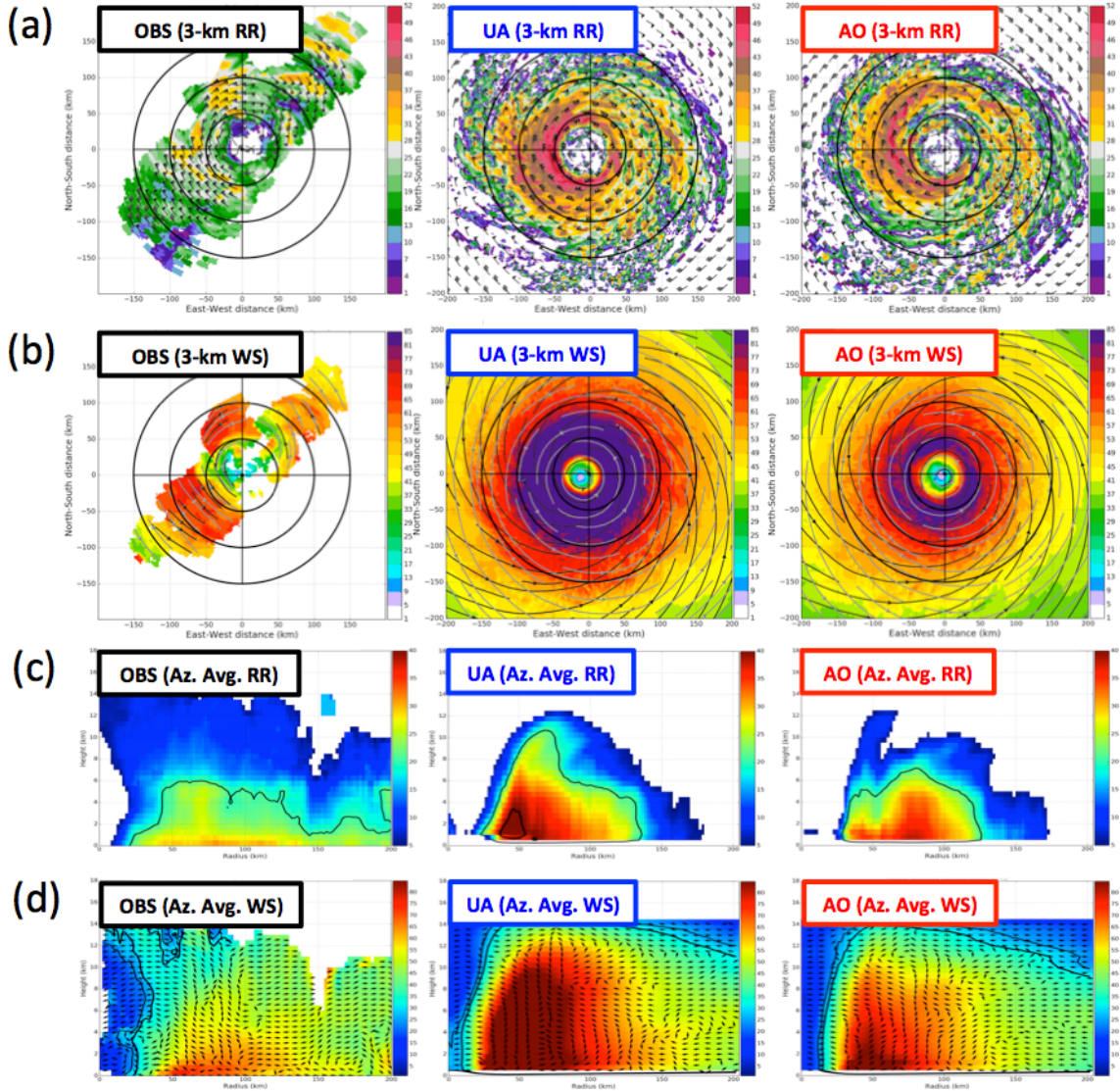


Figure 4.11 (a) NOAA WP-3D 3D Doppler Analysis flight-level composite (Sep 13 2000 UTC – 2410 UTC) and UWIN-CM storm-relative composite (2000 UTC – 2300 UTC) radar reflectivity (b) same as (a) but for wind speed (c) corresponding observed and model 2D azimuthal average radius-height radar reflectivity and (d) wind speed. In rows (a) and (b), black circles show distance every 50km. Flight-level wind barbs are overlaid on reflectivity figures, 0.5 (black) and 3km (grey) streamlines are overlaid on wind figures. For the 2D azimuthal average diagrams, reflectivity is contoured at 20 and 40 dBZ. Wind speed is contoured at 25 and 30 kt. Quivers show the radial-vertical velocity with length normalized to unity.

Near peak intensity, both model simulated TCs have largely symmetric precipitation and

circulation structure. Two structures distinguish the observed and coupled (AO) TC in particular – separate eyewall and rainband structures, and the vertical depth of strong reflectivity and winds. Flight-level model simulated radar reflectivity shows strong convection in UA near 50 km from center wrapped around ~3/4 of the storm center, with 40 – 45 dBZ directly radially adjacent to this eyewall. Observations and reflectivity from the coupled (AO) TC demonstrate the presence of a radially inward spiraling rainband (from forward right to rear left) and a partial, more axisymmetric eyewall predecessor. Precipitation remains too strong in both model simulations, but the coupled TC matches the observed structure by radius and quadrant reasonably well. From the azimuthal average summary plots in (c) and (d), we see UA is vertically compact but more intense than AO, with 30+ dBZ reflectivity returns reaching about 7 km. In the observed transect, 20-dBZ reflectivity returns reach 6 km height (as in AO) and overall echo top height is 10-14 km. Reflectivity returns in AO reach 12 km just inside the 50-km RMW, otherwise the majority of the storm has < 10 km echo tops.

We conclude this section with a remark on the model TC energetics. Despite having similar forward speed and vertical wind shear (DLS) that are suggestive of a similar evolution in the model large-scale atmosphere, without coupling to an interactive ocean (as in UA), the model TC does not suffer the reduction in air-sea enthalpy flux experienced by the AO simulated TC and the real Ophelia. To illustrate this, time-series of the latent heat flux compared with maximum wind speed (MWSP) are shown for the model TCs in Figure 4.12.

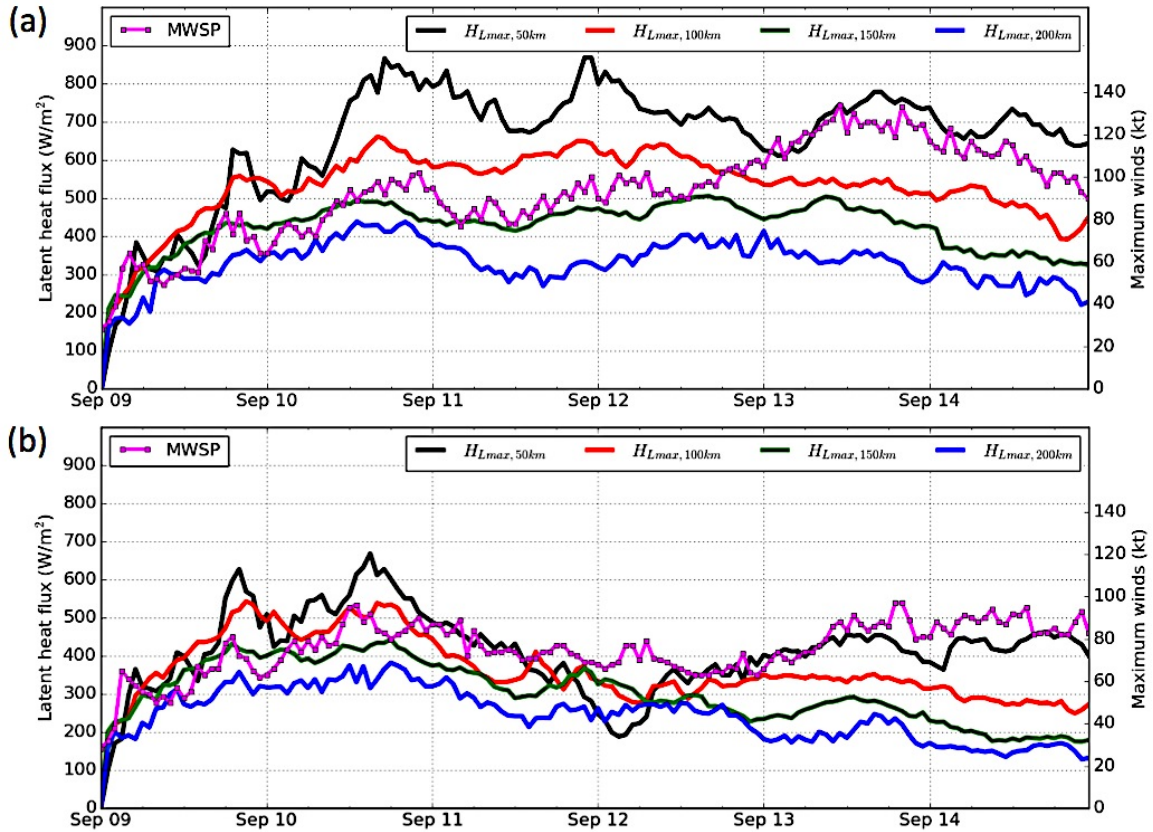


Figure 4.12 Timeseries of azimuthal average latent heat flux at 50km (black), 100km (red), 150km (green), and 200km (blue) for (a) UWIN-CM UA simulation and (b) UWIN-CM AO simulation. MWSP is given in magenta for the simulations in their respective panel.

Model latent heat flux is computed using the bulk aerodynamic flux formula,

$$H_L = \rho U_{10} [L_v C_e (q_{SSST} - q_{a10})] \quad (4.1)$$

where  $\rho$  is the air density,  $U_{10}$  is the 10-meter wind speed ( $\text{ms}^{-1}$ ),  $L_v$  is the enthalpy of vaporization,  $C_e$  is the air-sea enthalpy flux transfer coefficient,  $q_{SSST}$  is the specific humidity at the sea-surface temperature, and  $q_{a10}$  is the specific humidity of the air at the temperature at 10-meter height. From equation (4.1), the latent heat flux is a function of wind speed and air-sea moisture disequilibrium. In Figure 4.12, the latent heat flux is

computed as an azimuthal average quantity at 50, 100, 150, and 200 km from the storm center in (a) UA and (b) AO to show the relative magnitude of latent heat fluxes as a function of ocean coupling and determine at what times in the simulations the wind intensity and moisture disequilibrium respectively contribute to latent flux. Separating by 50km azimuths also reveals whether the strongest latent fluxes occur near or far from the storm center. Not surprisingly, latent heat fluxes are larger in the UA simulation for all four azimuthal averages after September 10 1200 UTC. Since the uncoupled TC is not aware of ocean cooling or evolution of any kind, and the maximum wind speed closely follows the timeseries of maximum 50km azimuthal average flux through the simulation we can state that both moisture disequilibrium and high wind speeds contribute to larger latent heat flux throughout the storm over the course of its evolution. In contrast, the maximum (minimum) of the maximum 50km azimuthal average fluxes are 22 (68) % lower in the AO simulation. Furthermore, the spread of latent flux timeseries at all azimuths is small (e.g. September 11 0000 UTC – September 12 0000 UTC, where the highest and lowest values are  $< 200 \text{ Wm}^{-2}$  apart). After September 11 1200 UTC, the maximum latent heat flux increases sharply by  $100 \text{ Wm}^{-2}$  and levels off through September 12 1800 UTC, first at 100, then 150, and finally to a lesser magnitude at 200 km from storm center. After September 13 0000 UTC when the AO storm is recovering over the Gulf Stream, the latent flux timeseries separates by azimuth similar to the UA simulation and the 50km maximum latent flux follows the MWSP trend reasonably well for the remainder of the timeseries. These timeseries show the expansion of AO (increase in latent fluxes far from storm center) late on September 11 – September 12 and contraction of UA (during RI) and AO (during recovery) on September 13.

## 4.2 Role of air-sea interaction on inner-core collapse and recovery

### 4.2.1 Air-sea enthalpy flux modification and structure change

In the real world, the atmosphere and ocean communicate momentum and heat back and forth via the air-sea interface and cannot be separated for the benefit of scientific inquiry. While tropical cyclones manifest themselves as an atmospheric disturbance of strong winds and heavy precipitation, they are energetically dependent upon the ocean. Having described the evolution of the model structure and intensity in the previous section, here we will examine the role of air-sea interaction in the collapse and recovery of the inner core in Hurricane Ophelia. In particular we subdivide the discussion in terms of latent heat flux modification due to storm-induced upper ocean cooling and propagation over the Gulf Stream as well as changes in the distribution of these fluxes as a function of storm size and maximum wind intensity. Both will be connected to the observed and coupled (AO) model simulated structure and intensity changes previously described.

Much in the way that gasoline provides fuel for an internal combustion engine, air-sea enthalpy fluxes from the ocean provide fuel for tropical cyclones. Furthering this analogy, if any heat engine is cut off from fuel or is unable to distance itself from the waste products produced as a result, the efficiency and function of the engine altogether will be compromised. Strong upper-ocean cooling induced by Ophelia's surface winds was well captured in the coupled model. The storm's cyclonic wind stress persisting over the ocean on diurnal timescales facilitated the upwelling of much cooler water and shallowing of the model ocean-mixed layer (OML) beneath the storm. A diagram depicting the physical processes in TC-induced ocean cooling through a sample TC cross-section is given in Figure 4.13.

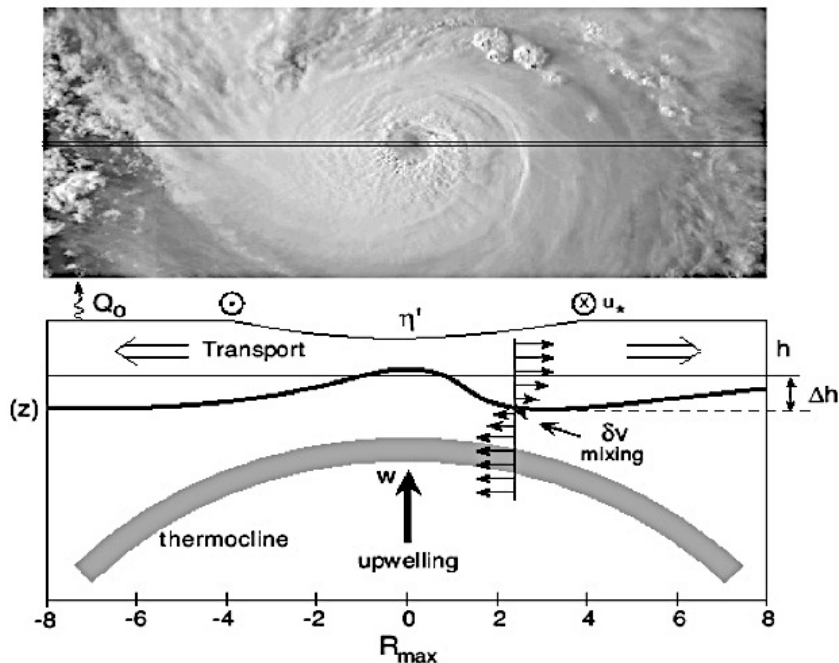


Figure 4.13 Summary of TC-induced upper ocean cooling physical processes through a sample TC in cross-section.

Previous studies have described forced cooling of the ocean during hurricane passage (e.g. Price, 1991) while more recent work (e.g. Halliwell et al. 2015) places ocean response in the context of the storm size and speed. In the figure above, three processes are depicted pertaining to TC-induced ocean cooling. As all three processes are dynamically or thermodynamically driven by the coupled TC-ocean environment, each occurs in every TC although their relative magnitude depends on various factors (e.g. size, forward speed, SST). Upwelling and shear-induced mixing are mechanically driven by stress from TC surface winds on the ocean. Evaporation is typically most dominant in the outer core regions where winds are relatively weak. Past work has shown that 85-90% of SST cooling is driven by upwelling and shear-induced mixing (Elsberry et al. 1976; Price 1981; Shay et al. 1992; Jacob et al. 2000). Since the AO model simulation (hereafter Ophelia) has a forward speed  $< 5 \text{ ms}^{-1}$  at all times after September 10 1800

UTC (when the cold pool begins to form), we computed the azimuthal average of surface – 100 m upper ocean mean temperature (T100) and surface wind speed to show depth-integrated cooling as it evolves from the pre-storm upper ocean state. Figure 4.14 shows storm-relative T100 spatial maps, azimuthal average T100, and Ophelia’s maximum wind speed (a) just as the cold pool begins to form and (b) 36h later, once the cold pool was near peak magnitude.

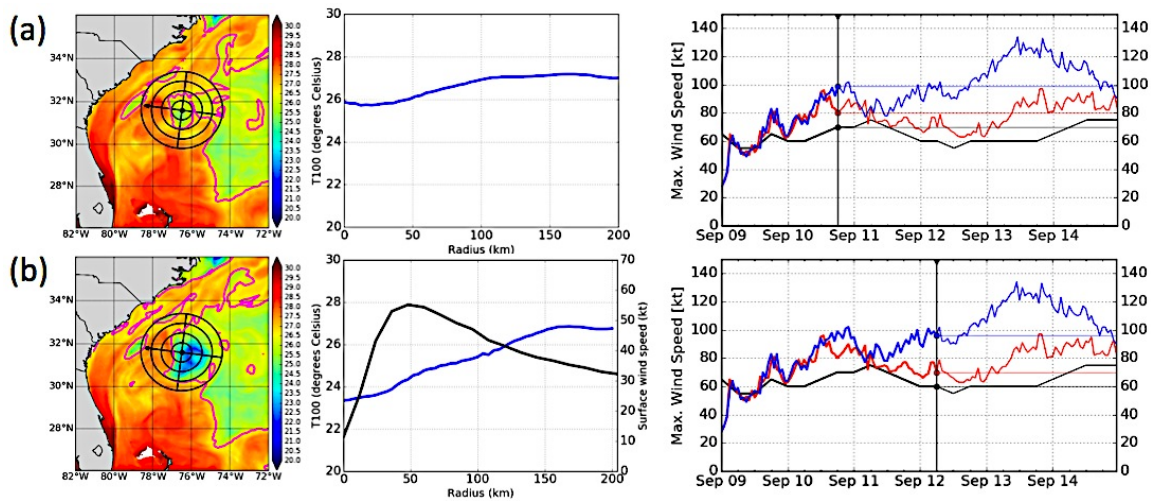


Figure 4.14 (a) T100 (left, deg C), azimuthal average T100 (center, blue), and observed/model maximum wind speed for September 10 1800 UTC (b) same as (a) except for September 12 0600 UTC. Azimuthal average surface wind speed (kt) is given in the center panel.

As Ophelia began its anticyclonic loop September 10 1800 UTC, MWSP was 80 kt. A lobe of 25.5 – 26°C T100 located on the western fringe of a broader region of cooler upper ocean east of the Gulf Stream signified the upwelling that would form the cold pool had begun. The black dot and arrow in the left panel of row (a) show the position and heading of the storm as it will be once reaching the time depicted in row (b). The azimuthal average field shows local depression of T100 below or near 26°C is confined to ~50 km from storm center early, but spreads and cools further over the 36h thereafter.

By September 12 0600 UTC, although 10 kt weaker the cumulative impact of upwelling and shear-driven entrainment in the upper ocean had cooled the azimuthally averaged T100 below 26°C out to 120 km from storm center. At and within the 60-km surface RMW on September 12 0600 UTC, T100 had cooled by 1.5 – 2.5°C from the initial state depicted at far left in panel (a). Given the complex track during the loop phase and the spreading of cooler T100 associated with the cold pool we expect the inner collapse to begin as a local weakening of precipitation structure in particular quadrants over which the cold pool is situated, then to spread to encompass the entire inner core as was observed during RAINEX. Convection should be diminished or absent beginning in the rear-right quadrant first, accounting for the asymmetric structure in the early stages of the inner core collapse. Storm-relative snapshots of T100 overlaid with 3-km radar reflectivity given in Figure 4.15 capture the decreased asymmetry of the upper ocean OML temperature structure and absence of convection over the core of the cold pool by September 12 0600 UTC.

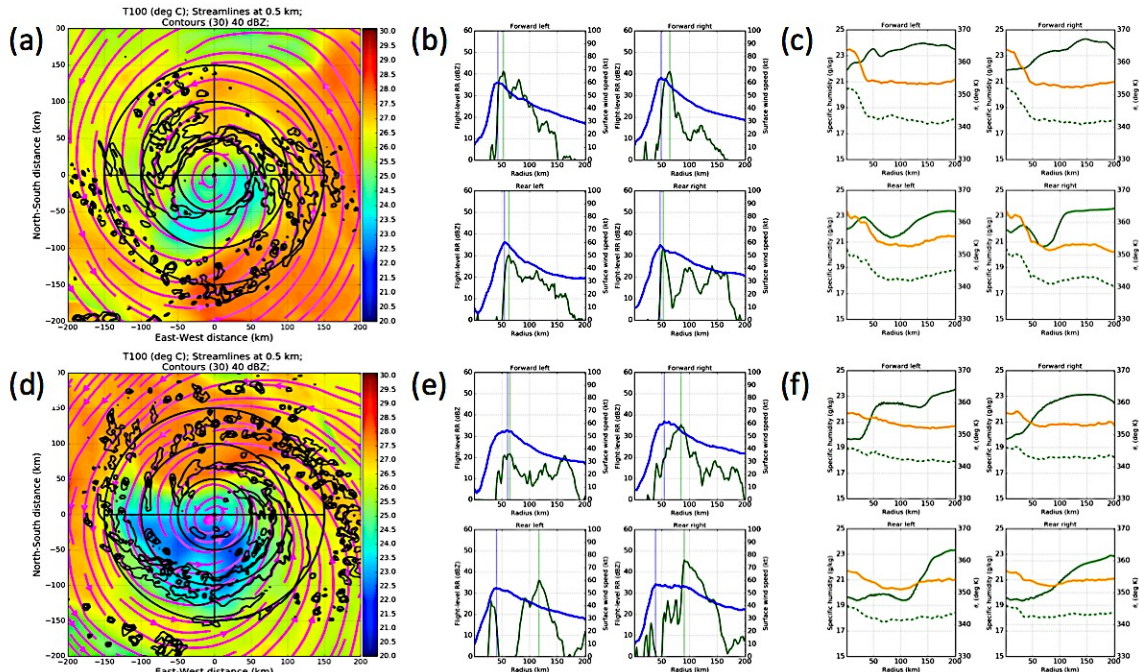


Figure 4.15 (a) storm-relative T100 (deg C), 0.5km streamlines (magenta, kt), and flight-level radar reflectivity (contoured at 20 and 40 dBZ) (b) quadrant azimuthal average surface wind speed (kt) and flight-level radar reflectivity (dBZ) with RMW and RMR indicated by the vertical blue and green lines (c) quadrant azimuthal average qSST (g/kg; green solid),  $q_{a10}$  (g/kg; dashed green), and equivalent potential temperature (deg K; orange). Azimuthal averages 0-200 km. Top row corresponds to September 11 0600 UTC, bottom row corresponds to September 12 0600 UTC.

In Figure 4.15, (a) – (c) show the TC on September 11 0600 UTC, during an early part of the cold pool interaction. Flight-level radar reflectivity and surface wind speed are azimuthally averaged in (b), as are  $q_{SST}$ ,  $q_{a10}$ , and surface  $\theta_e$  in (c). 24-25 °C T100 associated with the cold pool is mainly confined to the rear quadrants. Azimuthal average comparisons by quadrant reveal negligible differences in the along-radius structure of the vortex, however radar reflectivity returns are 10 dBZ weaker over the rear quadrants and the jagged appearance in the forward-left and rear-right quadrants compared with panel (a) is related to the incomplete but convective eyewall and radially inward spiral rainbands composed of more generally stratiform reflectivity (between 20 – 40 dBZ). The four-panel shows the azimuthal average moisture disequilibrium and equivalent potential temperature (EPT) by quadrant. In the forward quadrants,  $q_{SST}$  and  $q_{a10}$  have opposite trends at and beyond the RMW; over the developing cold pool however, both the sea surface and near-surface air are cooling 30-80 km from storm center. Hence, when the cold pool is localized early on September 11, positive moisture disequilibrium and enthalpy flux conditions occur over the undisturbed forward quadrants, and are suppressed over the core of the cold T100 anomaly signature of the cold pool in the rear quadrants. Azimuthal average reflectivity also demonstrates strong to intense convection is not being supported over these quadrants. After moving south-southwest from September 11 0000 UTC – 1800 UTC, Ophelia changes direction toward the northwest.

In so doing, the storm begins to track over more of the previously upwelled colder water and the cold pool fills out. By September 12 0600 UTC, Ophelia is near completion of its loop phase. The region of coldest T100 has spread considerably and all four quadrants have depth-integrated upper ocean temperatures of 21 – 26°C. Ophelia’s center is ~6h from crossing the western edge of the cold pool at this time, and the most intense cooling is over the rear quadrants (Figure 4.15d), where the OML remains shallow (25-50 km). From the T100 azimuthal average evolution shown in Figure 4.14, the ‘pre-storm’ upper ocean was already a modestly cool 26 – 27°C over the 0 – 100 km region before the most intense upwelling and mixing occurs. Unlike early on September 11, the circulation and precipitation maxima are no longer aligned in all four quadrants. The azimuthal average surface RMW remains approximately 50 km, however the structure of the radial profile of the wind in each quadrant has weakened and the cross-RMW gradient is less pronounced over the rear quadrants. Strong precipitation is not supported within the RMW in the inner core but rather at 75-100 km radii from the storm center. The most intense precipitation occurs in a large, discrete rainband wrapping cyclonically inward from far rear-right towards the region directly due north of storm center. This rainband is situated over 27-28°C T100 beyond the edge of the cold pool and over the Gulf Stream ahead of Ophelia. As a result, positive moisture disequilibrium is favored most strongly in the forward right and rear right quadrants between 75-80 km from the storm center, consistent with the region of highest enthalpy inner core air outside the eye and stronger enthalpy fluxes at distant radii.

TC-induced upper ocean cooling clearly acted to reduce air-sea enthalpy flux in the inner core region, forcing an expansion of precipitation (and shortly thereafter, the

vortex itself). Equivalent potential temperature within the RMW falls from greater than 360K to between 355-356 K at the storm center. The radial structure of EPT levels off between 352-354 K over the 24h period previously described. Cooling of the near-surface air over the cold pool greatly reduces the eye-inner core gradient in EPT typically distinguishing the warm core, stabilizing and effectively homogenizing the near-surface air in the inner core much as shear-driven mixing homogenized OML T100. Even with a cooler ocean, Ophelia's surface circulation still exerts wind stress on the ocean surface and evaporation (although diminished) still occurs. Local enthalpy flux is still present, however it conveys less energy. As seen in Figure 4.15d, however, streamlines of the near-surface circulation show converging air spirals inward from beyond 200 km in the rear-right quadrant along and ahead of the axis of the discrete convective outer band. Advection of high-enthalpy air relative to that over the cold pool core may contribute to the support of this precipitation, particularly as the source air directly upstream of this outer rainband is being advected from a region of ocean with 0.5 – 1°C cooler T100 as positive moisture disequilibrium is enhanced by both increasing  $q_{SST}$  and decreasing  $q_{a10}$ .

Structure and intensity evolution of TCs passing over favorable ocean environments has been investigated in previous studies (e.g. Loop Current WCEs or the Gulf Stream) (Shay et al. 2000; Bosart et al. 2000; Nguyen & Molinari 2012). Ophelia's convective reinvigoration and recovery over the Gulf Stream provides a unique and insightful addendum to these past works. Prior to the entire inner core being over the Gulf Stream, the vertical structure of the ocean beneath the storm changed rapidly in the along-track axis. A spatial map of T100 and storm-relative vertical cross-section of 0 –

200 m upper ocean temperature overlaid with mixed layer depth (MLD) shown in the left and center panels of Figure 4.16a depict the adjacent cold pool and Gulf Stream structure. In panel (b) as in Figure 4.14b, we show T100 relative to the storm's position, azimuthal average T100 and surface wind speed radial profiles, and the maximum intensity – here for September 13 1200 UTC, preceding Ophelia's northward turn parallel to the Gulf Stream.

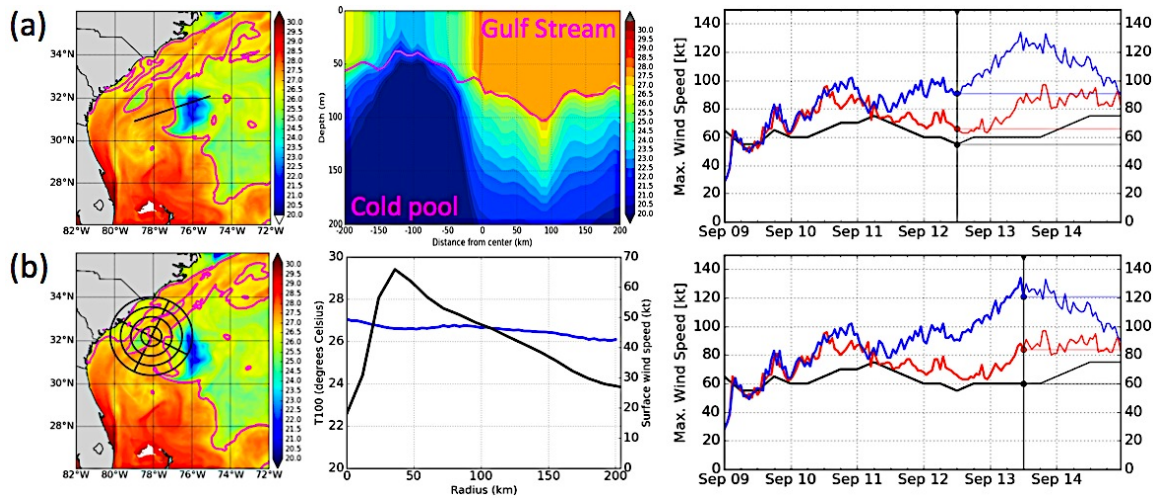


Figure 4.16 (a) T100 (left, deg C), upper ocean along-track vertical transect (center), and observed/model maximum wind speed for September 12 1200 UTC (b) same as (a) except for September 12 1300 UTC. Azimuthal average T100 (blue, deg C) and surface wind speed (black, kt) is given in the center panel.

Between September 12 0600 UTC and September 13 1200 UTC, Ophelia moved west of the ridge of shallow mixed layer depths 30 – 60m associated with the storm-induced cold pool, and turned north parallel to the warm ( $27.5 + ^\circ\text{C}$ ) and deep (MLD 60 – 100m) OML of the Gulf Stream. The azimuthal average radial profile in the center panel of 4.16b shows the nearly uniform  $\sim 27^\circ\text{C}$  T100 even at large radii. Ophelia intensifies by 20kt over the 24h period between rows (a) and (b). Despite continuing to move slowly and having strong maximum winds (85 kt), the favorable, deep oceanic heat source provided by the Gulf Stream buffers the surface and OML from the upwelling/entrainment of

colder sub-ML waters. Additionally, with Ophelia turning parallel to the coast after September 13 1200 UTC with a more linear track any cooling that occurs from stress-induced shear mixing in the upper ocean will occur right and behind the storm motion rather than beneath the entire inner core. Here we have shown Ophelia intensifies by the largest magnitude throughout the simulation period (20 kt) after departing a weakly stratified, cold upper ocean and propagating over a stratified, substantially warmer upper ocean. Figure 4.17 connects this intensification to recovery of the inner core structure with storm-relative T100 maps overlaid with moderate to strong precipitation and azimuthal average flight-level reflectivity, surface wind speed, and moisture disequilibrium by quadrant. Panels (a) – (c) are from September 12 1200 UTC, while (d) – (f) are from September 13 1200 UTC.

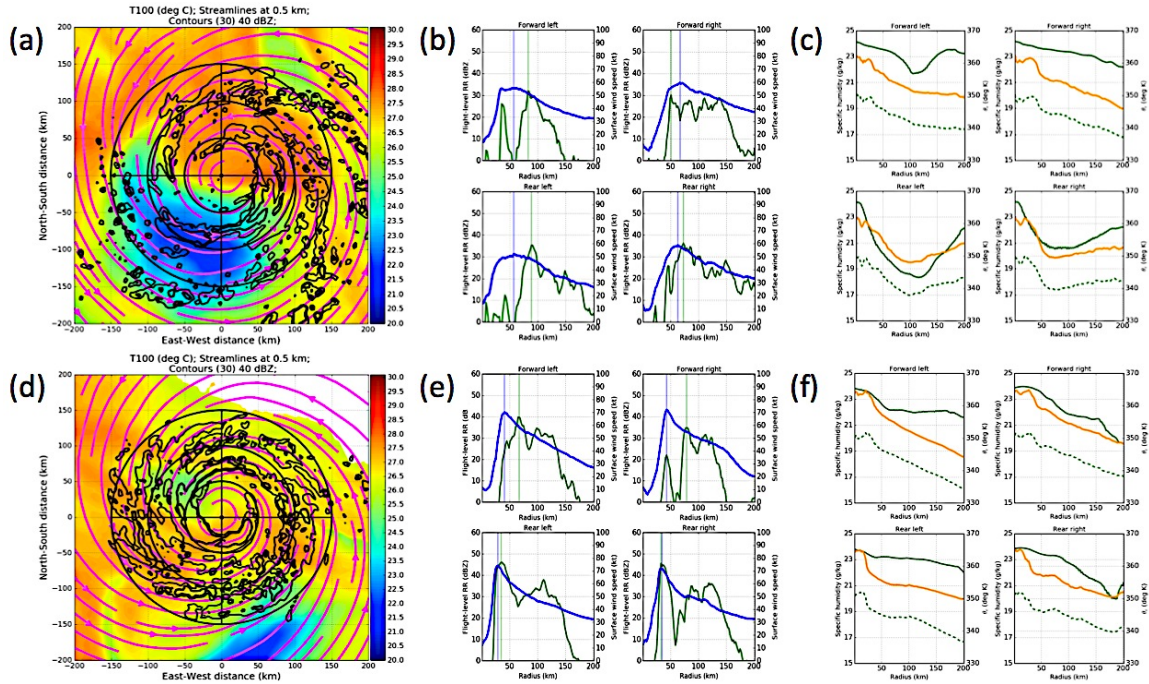


Figure 4.17 (a) storm-relative T100 (deg C), 0.5km streamlines (magenta, kt), and flight-level radar reflectivity (contoured at 20 and 40 dBZ) (b) quadrant azimuthal average surface wind speed (kt) and flight-level radar reflectivity (dBZ) with RMW and RMR indicated by the vertical blue and green lines (c) quadrant azimuthal average qSST (g/kg; green solid), qa10 (g/kg; dashed green), and equivalent potential temperature (deg K;

orange). Azimuthal averages 0-200 km. Top row corresponds to September 12 1200 UTC, bottom row corresponds to September 13 1200 UTC.

Thin (thick) black contours in (a) and (d) in Figure 4.17 denote 30 (40) dBZ reflectivity returns indicative of moderate precipitation and intense convection. Ophelia becomes more compact and symmetric over the 12h period shown, with an intense crescent-shaped rainband ~25 km wide nearly enclosing the storm center September 13 1200 UTC. This feature was situated above 27 – 27.5 °C T100 and extended from rear-left to rear-right approximately 35-40 km from the storm center. A second convective rainband wrapped radially inward from rear-right to forward left near 100 km, however the azimuthal average radar reflectivity In (e) shows there is ~25 km radial separation between these features. Ophelia's broad, weaker wind field on September 12 strengthens (by 4-12 kt by quadrant) and the cross eyewall gradients sharpen as the storm RMW contracts from 70 – 75 km to 35 – 40 km between the times. Over the rear-left and rear-right quadrants containing the ‘pre-eyewall’ precipitation structure, reflectivity at the RMR exceeds 40 dBZ and the RMR and RMW are nearly collocated. Comparing azimuthal average reflectivity profiles in (b) and (e) against the upper ocean environment also reveals the earlier separation between RMW and RMR when Ophelia had expanded (September 12 0600 UTC – 1800 UTC) and that intensity of precipitation in each quadrant was inconsistent and weaker, dominated by more stratiform 20 – 30 dBZ returns. Conversely, convective (40 + dBZ) and more stratiform (e.g. 20 – 30 dBZ) reflectivity returns associated with a distinct newly forming eyewall and inner core rainband appear radially adjacent, separated by a small region of weaker returns between. As discussed earlier, Ophelia regains mature TC structure over the Gulf Stream. A new eyewall forms and the

storm possesses moderate to intense convection with the azimuthal average moderate returns reaching 6-7 km and average echo top height of 8-10 km. Moisture disequilibrium profiles in (f) demonstrate an inner-core to environment radial gradient is reestablished by September 13 1200 UTC. Both  $q_{SST}$  and  $q_{a10}$  decrease steadily from the 0 to 200km in all quadrants, with higher enthalpy air present nearer to the storm center. In each quadrant,  $q_{SST}$  and  $q_{a10}$  reverse and positive moisture disequilibrium occurs within the respective quadrant RMWs. This observation does not discount air-sea enthalpy flux occurring at or beyond the RMW, but specifically emphasizes the presence of high enthalpy air and latent fluxes inside the inertially stable region of Ophelia's recovering inner core.

#### ***4.2.2 Storm size implications for local and non-local air-sea enthalpy flux***

In the previous section, we used analysis of coupled model output to describe how air-sea interaction facilitated the collapse and recovery of Ophelia's inner core structure via air-sea enthalpy flux (i.e. energy availability) modification in the upper ocean and near-surface hurricane boundary layer atmosphere. To this point the focus was on positive moisture disequilibrium, which has been shown in recent work to be more representative than raw SST or ocean heat content in describing the favorability of TC intensity change (Cione, 2015). Here, we will shift our attention to storm size and its impact on the upper ocean and the distribution of air-sea enthalpy fluxes. The timeseries of MWSP and RMW are shown for comparison in Figure 4.18.

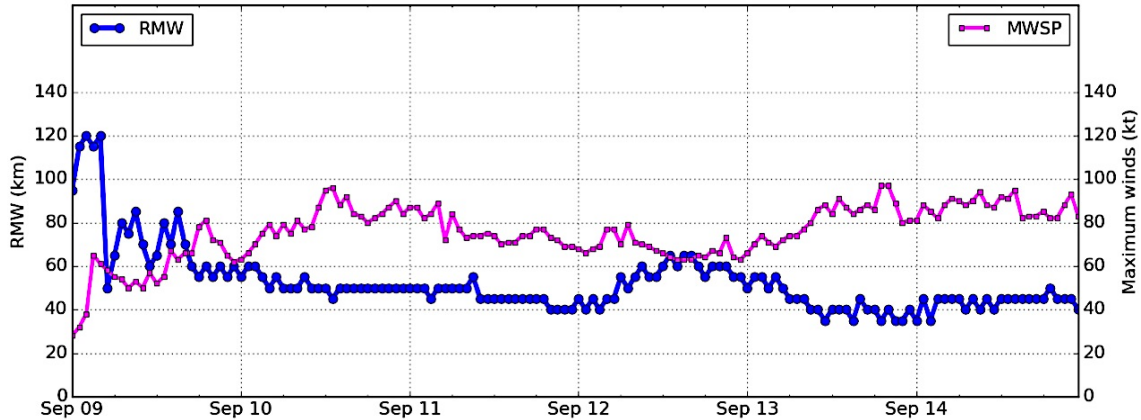


Figure 4.18 Timeseries of UWIN-CM AO radius of maximum wind (blue, km) and maximum wind speed (magenta, kt), September 9 – 15.

Ophelia's RMW remains almost steady between 40 and 50 km for a majority of the simulation after the spin-up period early on September 9, with two exceptions. From September 12 0000 UTC – September 13 1200 UTC, Ophelia's circulation expands (from 80 to 160km diameter) and then contracts, reaching a maximum (minimum) diameter of 160 (70) km September 12 1200 UTC (September 13 1800 UTC). The expansion coincided with limited change in intensity. Ophelia's largest period of intensification accompanies contraction of the RMW by more than 220 % immediately thereafter. Azimuthal average radius-height profiles of model wind speed at three select times (September 12 0000 UTC, 1200 UTC, and September 13 1200 UTC) are shown in Figure 4.19. These times were chosen to demonstrate the circulation structure changes and provide a comprehensive view of Ophelia's size and depth during the expansion and contraction. Magenta lines denote the 75-km radius from storm center and 6-km height as a reference.

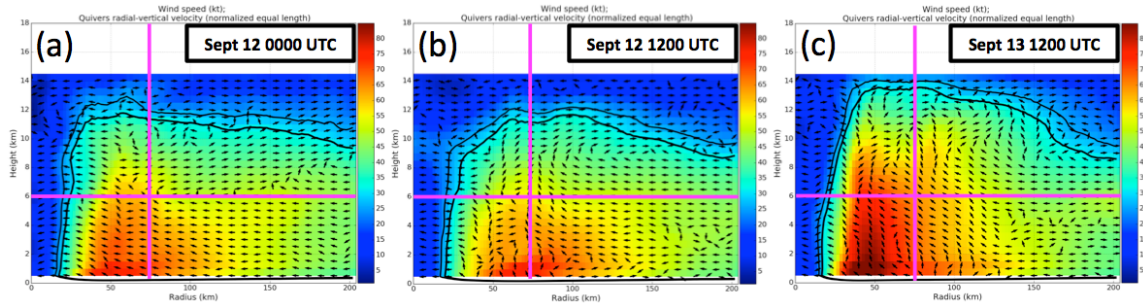


Figure 4.19 2D azimuthal average radius-height diagrams of UWIN-CM AO wind speed (0-18 km, 0.5km intervals) at (a) September 12 0000 UTC (b) September 12 1200 UTC and (c) September 13 1200 UTC. Magenta lines denote 6km altitude and 75km radius.

Near the end of its anti-cyclonic loop phase September 12 0000 UTC, Ophelia's azimuthal averaged circulation had a surface RMW near 50km and 64-kt (hurricane-force) winds extended vertically only 5-6 km. 70+ kt winds were confined within 75km of the storm center. Twelve hours later, hurricane force wind depth had shallowed further to less than 3km; below this height, 64+ kt winds reach outward to near 100km. While the storm was expanding, it was also broadening, becoming more uniform along radius, and had a noticeable ‘squashed’ appearance. Panel (c) shows the contracted storm ~6h prior to Ophelia’s maximum wind intensity. The vortex has recovered, and become deep (64kt winds at 8+ km), more upright, and intense, with uninterrupted vertical motion near and inside the RMW. To get a clear picture of the momentum transfer between the TC surface winds and upper ocean before and at the storm’s peak size, we present storm-relative snapshots of surface ocean currents and T100, along with azimuthal average profiles (Figure 4.20).

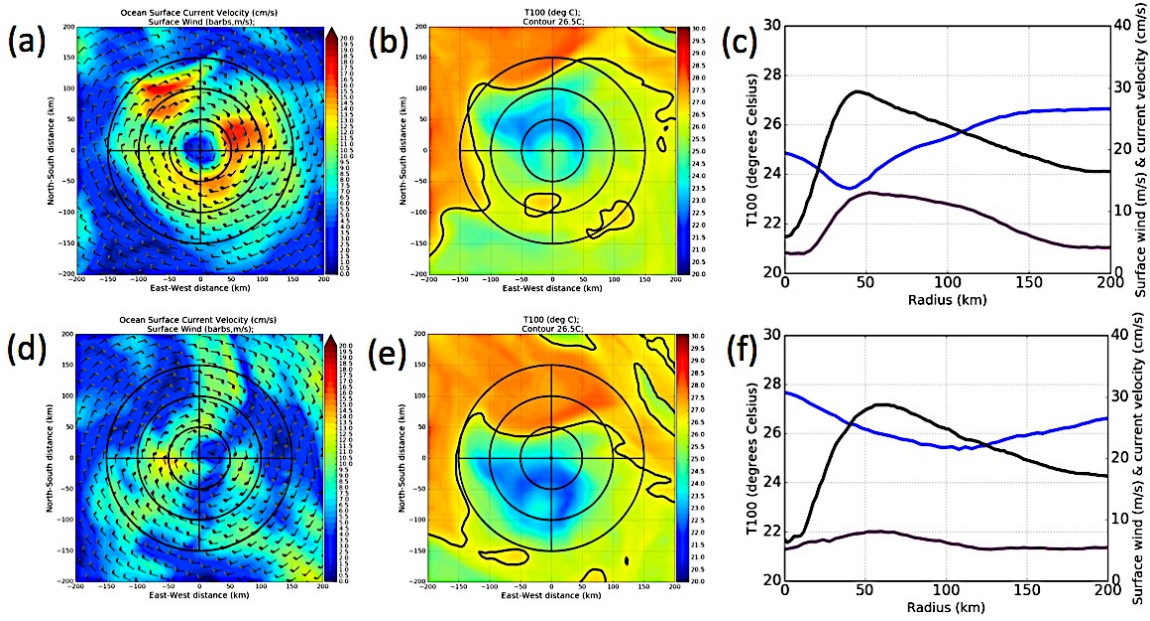


Figure 4.20 Storm-relative UWIN-CM AO (a) surface current velocity (cm/s) (b) T100 (deg C) and (c) azimuthal average profiles of surface wind speed (m/s, black), T100 (deg C, blue), and surface current velocity (cm/s, purple). Top row is for September 12 0000 UTC, bottom row is for September 12 1200 UTC.

Prior to the expansion, two large regions of strong surface current velocity in the range  $15\text{-}19 \text{ cm s}^{-1}$  are present within 200km radius. The crescent-shaped feature spanning the rear-left, rear-right, and forward-right quadrants was associated directly with Ophelia's  $35\text{-}40 \text{ ms}^{-1}$  maximum winds over those quadrants. The second, comma-shaped region was  $> 25\text{km}$  away from the RMW over the forward-left quadrant. The strongest surface currents over the forward right (50-100 km radius) and forward-left (100 – 125 km) quadrants were collocated with  $23\text{-}24^\circ\text{C}$  T100 temperatures. By contrast, the surface currents 12h later (Figure 4.20d) were weaker and more disorganized, distributed across different quadrants of the storm and not clearly underlying the RMW or regions of particularly strong winds. Surface wind and current velocities are compared in the azimuthal average profiles for the two times in (c) and (f). Before the expansion occurs, the cold pool has not completely filled with sub- $24^\circ\text{C}$  T100 and the coldest upper ocean

temperatures are aligned with the radius of strongest surface wind and current velocities. Once the storm expands and weakens, TC-ocean feedback decreases the magnitude of frictional dissipation by the wind stress, and TC to ocean momentum transfer lessens. Surface current velocities are generally  $10 - 12 \text{ cms}^{-1}$  by September 12 1200 UTC, with the azimuthal average being even weaker, approximately  $5 - 10 \text{ cms}^{-1}$ . T100, surface wind and current velocity are not as aligned here. While the surface current maxima still occurs near the RMW ( $\sim 60 \text{ km}$ ), the along-radius trend is almost neutral (little increase or decrease) and neither this nor the surface winds match the minima of T100 near 100km from center.

Ophelia's acute turn from south to northwest early on September 12 complicates the ocean response to the enlarged vortex. Storm-induced upwelling initiated the ocean modification at a time when Ophelia was smaller, but with higher MWSP ( $80 - 85 \text{ kt}$ ). Upwelling transported cold sub-OML water toward the surface to compensate for Ekman divergence of surface waters, as required by mass continuity. The strength of upwelling is proportional to Ekman divergence,

$$-\nabla \cdot U_{Ek} = -\left(\frac{\partial u_{Ek}}{\partial x} + \frac{\partial v_{Ek}}{\partial y}\right) \quad (4.2)$$

where Ekman transport terms  $u_{Ek}$  and  $v_{Ek}$  are

$$u_{Ek} = \frac{1}{\rho f} \frac{\partial \tau}{\partial y} \quad (4.3a)$$

$$v_{Ek} = -\frac{1}{\rho f} \frac{\partial \tau}{\partial x} \quad (4.3b)$$

and wind stress  $\tau$  is proportional to the square of the surface velocity.

As the ocean near the storm center cools, air-sea enthalpy fluxes inside and near the RMW are reduced. Since the TC is comparatively small when the cold pool is first

forming, the local reduction in heat and moisture translates quickly to weakening of buoyant vertical mass transport and mid-level release into the warm core. Less energy therefore can be converted to spin up or even maintain tangential wind velocity. Ophelia's wind speed steadily falls as a result of upwelling, and the TC-ocean feedback that initiated the cold pool forming also lessens. Regardless of the maximum intensity, Ophelia is still coupled and continues to confer momentum to the ocean. Similar to upwelling, enhancement of surface current velocity by the TC is related to the wind speed however shear-induced mixing in the upper ocean is related to overturning of the near-surface water. With the upper ocean already cooled and the OML having been shallowed by upwelling, even small momentum transfer by the TC to the surface can aid horizontal spreading of the cold pool, as depicted in Figure 4.20 (b) and (e).

To quantify the amount of kinetic energy transferred to the ocean as a function dependent on storm maximum wind speed *and* size, we computed integrated kinetic energy (IKE; Powell and Reinhold, 2007) using the method described in PR07 for the H\*WIND surface wind analysis products (see Chapters 2,3). In brief, the IKE value is a weighted sum of three components corresponding to polynomial linear regression fits describing the relative magnitude of the IKE based on various wind radii. Using this approach, maximum wind speed is more heavily weighted over storm size when the TC is stronger.

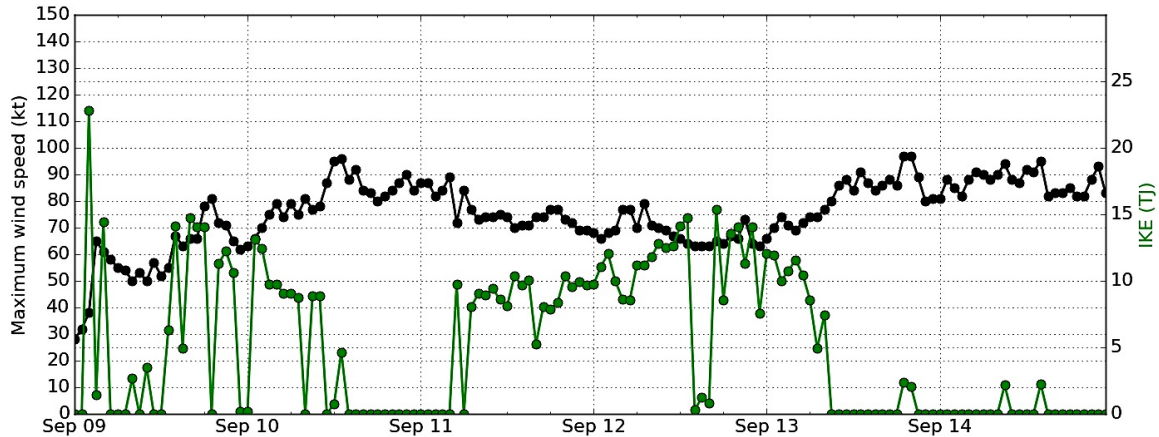


Figure 4.21 Timeseries of UWIN-CM AO maximum wind speed (black, kt) and integrated kinetic energy (using PR07 method; green, TJ), September 9 – 15.

From the timeseries, we can first acknowledge a caveat presented in PR07 that plagues this comparison to MWSP. While this approach to computing IKE includes multiple wind radii and accounts for the relative strength of a storm, it is derived from approximated relationships using observationally composited H\*WIND surface wind fields and is sensitive to the exact MWSP. Specifically, when Ophelia is stronger and smaller, IKE is weaker (or zero) using this method. IKE does however, generally remain non-zero and between 7.5 – 10 TJ, maximizing near midway on September 12 when Ophelia expands and then decreasing as the storm contracts. To conclude this discussion, Figure 4.21 below shows the maximum azimuthal average surface wind speed every 50km from storm center. This timeseries shows the simultaneous weakening of 50km  $V_s, max$  (by ~2.5 kt) and strengthening of 100km  $V_s, max$  by similar magnitude from September 12 0000 UTC – 1200 UTC as Ophelia’s RMW expands. For all other periods during the simulation, the typical decrease in  $V_s, max$  occurs moving to further distance from storm center.

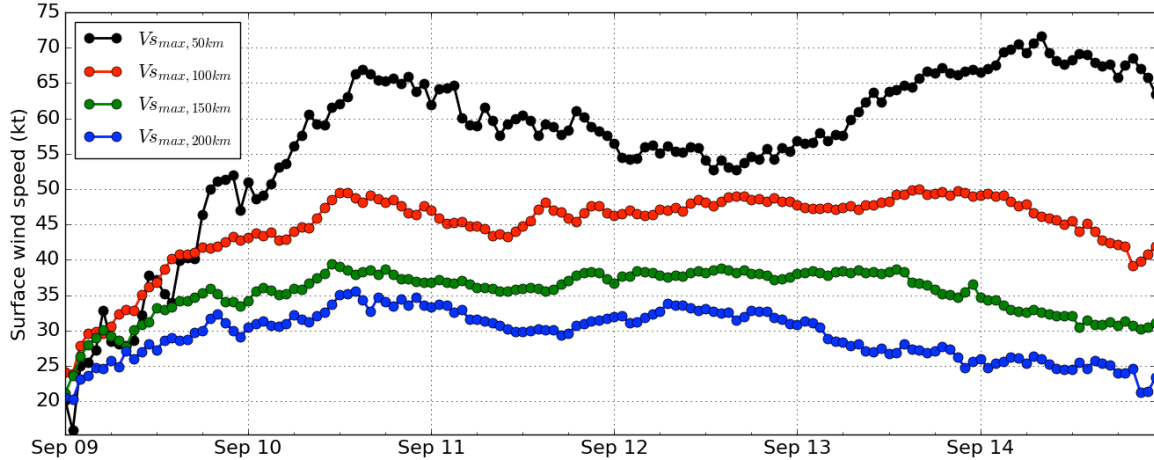


Figure 4.22 Timeseries of UWIN-CM AO azimuthal average surface wind speed at 50km (black), 100km (red), 150km (green), and 200km (blue), September 9 – 15.

#### 4.2.3 Summary

Here, we briefly summarize the evolution of the surface moisture disequilibrium, storm size, and intensity as described by the surface circulation. These two factors contribute to the air-sea enthalpy flux, specifically latent heat flux and ultimately the location, depth, and intensity of precipitation – a hallmark of TC structure. To show changes in surface moisture disequilibrium, storm size and intensity impact (via IKE), precipitation, and surface winds we use timeseries from UWIN-CM AO simulation output. Timeseries quantities are the azimuthal average difference, with the 100km average subtracted from the 50km average. By taking the difference between near-center and more distant radii, we can more easily discern local and non-local air-sea interactions and their contribution to the structural evolution described earlier. Figure 4.23 shows the timeseries for contributing components to latent heat flux, namely the surface moisture disequilibrium and storm size/intensity as given by integrated kinetic energy (Powell and Reinhold, 2007).

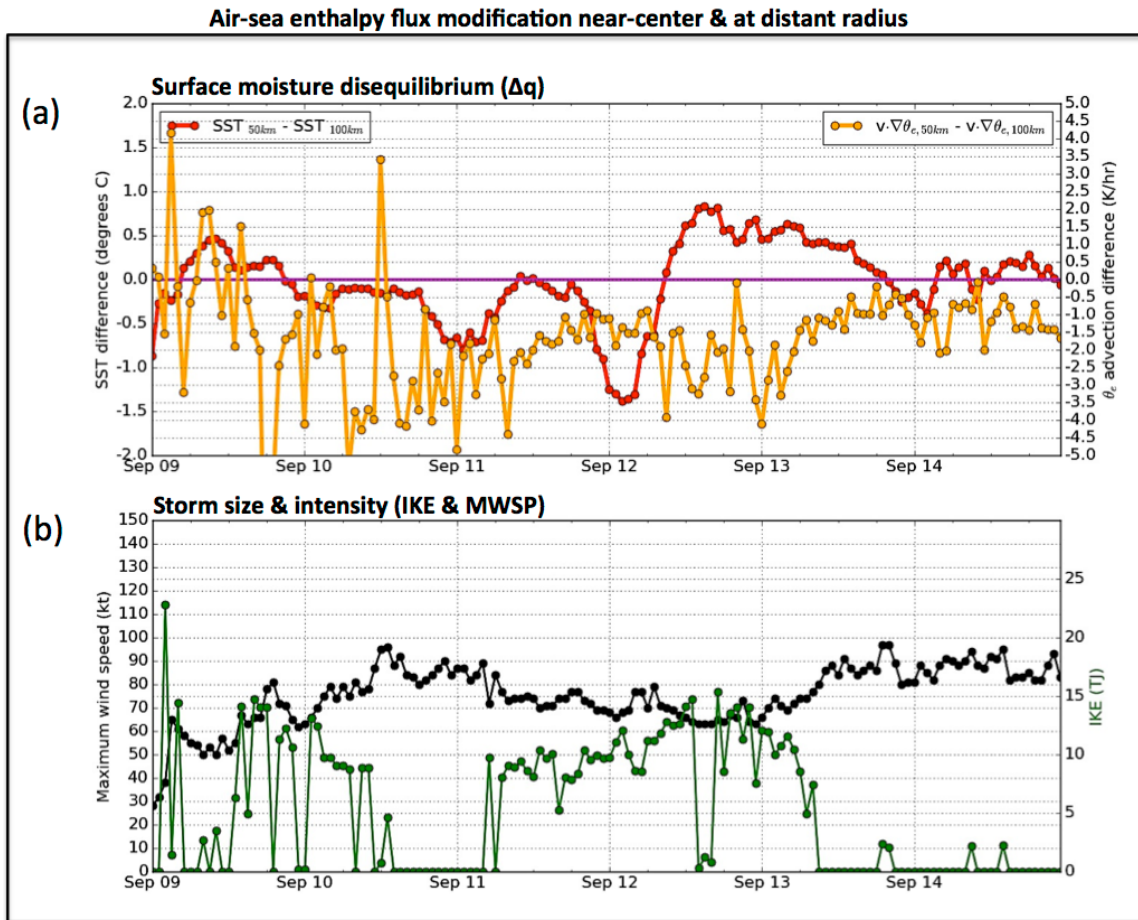


Figure 4.23 Timeseries of UWIN-CM AO (a) azimuthally averaged SST difference (red, deg C) and surface equivalent potential temperature advection (orange, K/hr) overlaid with a magenta line denoting zero (b) MWSP (black, kt) vs. IKE (green, TJ; PR07).

Equivalent potential temperature advection is computed using the outermost parent UWIN-CM WRF domain and surface winds (d01) as vortex-following grids in the Ophelia simulations are sufficiently small as to exclude much of the ambient environment. The equation used for equivalent potential temperature (EPT) is

$$\theta_e = T \left( \frac{p_0}{p} \right)^{\Gamma(1 + \Gamma_{md}Q)} \exp \left( \frac{3376}{T_{LCL}} - 2.54 \right) \cdot Q(1 + 0.81Q) \dots (4.4)$$

where  $T$  is temperature (K),  $p_0$  is standard reference pressure,  $p$  is the full pressure field,  $\Gamma = R_d/c_{pd} = 287/1004$ ,  $\Gamma_{md} = 0.608 - 0.887$ ,  $Q$  is the water vapor mixing ratio,

$T_{LCL} = 55 + \left( \frac{2840}{\ln\left(\frac{T^{3.5}}{e}\right) - 4.81} \right)$  is the temperature at lifted condensation level,  $e = \frac{Qp}{\varepsilon+Q}$  is the vapor pressure. This variable serves as a metric for the near-center to distant radius enthalpy gradient and nonlocal input via advection of air of differing enthalpy. From Figure 4.23a, we see that  $\Delta(-\mathbf{v} \cdot \nabla \theta_e)_{50-100}$  shown in orange remains negative for almost the entire simulation, while  $\Delta SST_{50-100}$  changes sign for periods ranging from 2 – 36h in length. The gradient of SST (and hence qSST) is more variable in time than that of surface EPT advection, and the tendency of the individual terms demonstrates that after September 11 0000 UTC the ocean (via qSST) is more critical to the location and intensity of the greatest surface moisture disequilibrium (described as ‘positive enthalpy flux condition’ in Cione, 2015). During interaction with the cold pool, centered about the time maximum near-center cooling occurs,  $\Delta SST_{50-100}$  is negative and  $\Delta(-\mathbf{v} \cdot \nabla \theta_e)_{50-100}$  remains almost steady near -0.5 K/hr. This 20h period includes Ophelia’s southwestward anti-cyclonic loop segment during which upper ocean mixing aids upwelling and spreads negative SSTa, and the turn northwestward when the cold pool attains maximum SSTa near-center. The near-steady surface EPT advection indicates the enthalpy content on average at 50 and 100km was relatively homogenous, although slightly favoring higher values at 100km. As Ophelia transitions from cold pool to Gulf Stream upper ocean environments,  $\Delta SST_{50-100}$  again becomes positive. Surface EPT advection is quite variable, but with a negative trend (-1 decreasing to -4K/hr) between September 12 0600 UTC and September 13 0000 UTC that indicates the enthalpy distribution along-azimuth at 50 and 100km is becoming more separated. In particular, the negative trend implies higher enthalpy air is present at 100 km (vs 50 km) due to

advection. Nearing peak intensity around September 13 1800 UTC, both  $\Delta SST_{50-100}$  and  $\Delta(-v \cdot \nabla \theta_e)_{50-100}$  approach zero, with the former remaining slightly positive and the latter remaining increasingly (-1.5 to -2K/hr) negative through September 15 0000 UTC. In panel (b) of Figure 4.23, the integrated kinetic energy (IKE; PR07) is shown along with MWSP (kt). Both MWSP and IKE are not spatially distributed quantities, and hence are shown as raw variables with no differencing. From September 11 0000 UTC to September 12 0000 UTC, Ophelia weakens by 20 kt. Over the 24h thereafter, the storm weakens a net 5 kt. Although weakening after interacting with its cold pool, the circulation expands considerably – as reflected by IKE, which remains  $> 10 \text{ TJ} (10 \cdot 10^9 \text{ kJ})$  almost continuously through September 13 0600 UTC. Near its peak diameter of  $\sim 130 \text{ km}$  on September 12 1800 UTC, Ophelia's IKE exceeds 15 TJ. The period of largest IKE is consistent with SST (and T100, not shown here) cooling near-center associated with upwelling, horizontal mixing and kinetic energy dissipation from Ophelia's surface winds. Collectively, the timeseries demonstrate that air-sea enthalpy flux modification involves both the upper ocean and near-surface atmosphere, with changes in qSST arising from the cold pool and Gulf Stream interactions dominating the variability of  $\Delta q_{50-100}$ . Furthermore, the inverse trend in  $\Delta SST_{50-100}$  and  $\Delta(-v \cdot \nabla \theta_e)_{50-100}$  terms from September 12 0600 – September 12 1800 UTC coincides with Ophelia's expansion and largest IKE values. The positive tendency of  $\Delta SST_{50-100}$  reflects increasing distance of the 50km radius from the cold pool core, while  $\Delta(-v \cdot \nabla \theta_e)_{50-100}$  reflects the advection of cooler (warmer) air from the cold pool (outside the storm) closer to storm center (the 100 km radius) (see also Figure 4.17a). Evidently, the circulation's size permits the advection of higher-enthalpy air masses into regions further

from storm center while simultaneously the inner-core is subject to negative surface EPT advection from the cold pool even as the storm moves away.

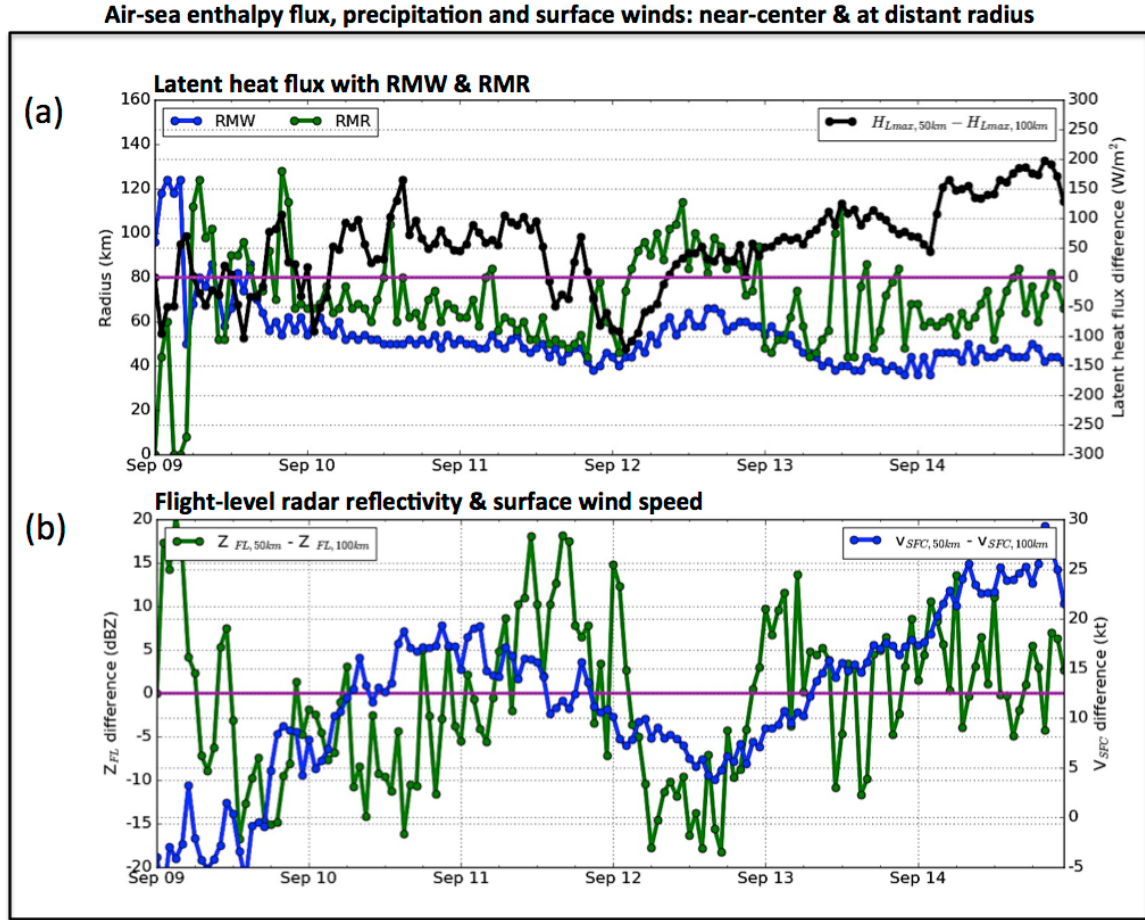


Figure 4.24 Timeseries of UWIN-CM AO (a) azimuthally averaged latent heat flux difference (black,  $\text{Wm}^{-2}$ ) overlaid with flight-level RMR (green, km) and surface RMW (blue, km). (b) Azimuthally averaged flight-level radar reflectivity difference (green, dBZ) and azimuthally averaged surface wind speed (blue, kt). Magenta line denotes zero.

In order to demonstrate the combined effect of air-sea flux modification by TC-ocean feedbacks and storm size, panel (a) of Figure 4.24 above shows a timeseries of the latent heat flux difference between 50 and 100 km from storm center. Also plotted is the radius of maximum wind (RMW) and radius of maximum flight-level radar reflectivity (RMR). A timeseries of flight-level radar reflectivity difference and surface wind speed difference between 50 and 100 km is shown in panel (b). Using September 11 0000 UTC as a

milepost for the time after which the ocean becomes indivisibly critical to the AO simulation evolution, it can be seen that the latent heat flux is greater at 50km for the majority of the time after this hour – the exception being for the nearly 24h period September 11 1200 UTC – September 12 1200 UTC. This is the period encompassing the cold pool evolution/interaction. Responding to the weakening, cooling inner core, both the RMR and RMW begin expanding coincident with the global minimum latent heat flux difference (-125 Wm<sup>-2</sup>, occurs at September 12 0100 UTC). The maximum surface diameter (by RMW) lags behind the RMR by 5-6h, consistent with increasing latent heat flux at 50km (positive latent heat flux difference). RMR contracts from 85 km to 45 km over the last 6h of September 12, as latent heat flux difference begins to increase further. Comparing the timeseries in Figure 4.23, the latent heat flux difference trend after September 12 0900 UTC matches the behavior of  $\Delta SST_{50-100}$  reasonably well through September 13 0600 UTC. It should be noted here that for 60% of the period Ophelia's RMR exceeds 60km, the latent heat flux difference remains near-steady around 50 Wm<sup>-2</sup> (25% of global maximum difference). Latent heat flux still occurs at both 50 and 100km, however, prior to September 13 0000 UTC the strongest precipitation is occurring outside the RMW in part due to strong surface winds and advection of higher-enthalpy air further from storm center (see Figure 4.24b). Finally, in this chapter we have shown modification and redistribution of air-sea enthalpy fluxes induced by the TC circulation and its feedback with an interactive ocean instigated structure and intensity changes in UWIN-CM AO similar to those observed by RAINEX. Specifically, we have emphasized the importance of the ocean as a facilitator of local air-sea enthalpy flux modification and the expanded TC circulation as a vehicle for changing air-sea enthalpy flux distribution

through wind-stress mixing. Furthermore, we recognize the role of advection in supporting convection at distant radii in contrast to the weaker precipitation in the inner core.

## **Chapter 5: Conclusions**

### **5.1 Role of air-sea interaction**

In this study, we aimed to better understand the role of air-sea interaction and its contribution to structure and intensity changes in tropical cyclones, specifically the effects of coupling to an interactive ocean, modification of air-sea enthalpy fluxes and structure and intensity changes via air-sea interaction, and how the timing of these changes is dependent on the feedbacks and interaction between the storm and ocean. High-resolution Six-day UWIN-CM forecasts of Hurricane Ophelia were used to investigate structure and intensity changes observed during RAINEX, in particular the collapse and recovery of the storm's inner core. Uncoupled atmosphere and atmosphere-ocean coupled model experiments produced vastly different storm structure and intensity. Without an interactive ocean, the energy available to the TC was overestimated in the uncoupled storm, and it underwent two periods of intensification, including an RI phase September 13 -14 that were not observed in the real storm. Shallow and asymmetric storm structure during the cold pool interaction, expansion of the storm afterwards, and the eventual recovery of the eyewall and rainbands over the Gulf Stream were well captured in the coupled experiment. Good agreement between RAINEX observations and the coupled model storm allowed for a targeted study of air-sea interaction in Ophelia. Herein, we present conclusions based on detailed analysis of the storm structure, intensity, and changing storm and ocean environments:

- (1) Without an interactive ocean, SST remains too warm and results in an overestimation of air-sea fluxes that supply energy to the uncoupled TC. Intensity is adversely affected as pressure deepens and wind speed increases in response to the

favorable ocean environment. Though the uncoupled storm has very strong winds throughout the simulation, the storm cannot communicate them to the ocean despite moving with a similarly slow forward speed to the coupled storm. As a result, a sink for the storm's kinetic energy (via wind stress) is cut-off, as is the wind-evaporation feedback. Overestimation of energy produces a TC with deep, symmetric, overly intense precipitation (though precipitation bias is an outstanding problem, even in coupled simulations). The uncoupled atmosphere storm is too strong, and having only an atmosphere is insufficient to capture key feedbacks and air-sea interactions that have an impact on the structure and intensity.

(2) In the real world, the ocean and atmosphere exchange energy as heat and moisture, and momentum via the air-sea interface. Ophelia was weakly steered throughout the RAINEX campaign and model simulations, and executed an anti-cyclonic loop over ~36 hours late September 10 through early September 12. Both model simulations captured the loop, but in the coupled storm, Ophelia had reached a local maximum in wind intensity (~ 90 kt) prior to beginning the loop. A cold pool formed due to upwelling, responding to the storm's cyclonic wind stress diverging surface water beneath the TC. Transfer of momentum from the storm's surface winds to surface ocean currents was only felt in the coupled storm, and acted to homogenize the ocean mixed-layer (OML) and spread the cooling. After 1800 UTC September 11, the storm began to move northwestward, back over the previously formed cold pool. Colder SST induced by the storm reduced inner core air-sea flux, cooled and homogenized the surface equivalent potential temperature. Moisture disequilibrium was reduced locally, however advection of high-enthalpy air along converging streamlines in the far near-surface circulation

enhanced enthalpy flux and subsequent precipitation far from the storm center. Reduction of, or rather, accurate representation of the energy available to the storm was reflected in the structure evolution as well. Though the model track loop is smaller and more variable than the true storm, the inner core precipitation intensity weakens and the type of precipitation present is impacted by the air-sea enthalpy flux modification. The inner core, though not as weak as that seen by RAINEX, did contain the diversity of precipitation types during the early stages of the collapse. It was dominated by continuous, more stratiform precipitation, but featured some discrete rainbands far from the center and a partially formed eyewall with convection and trailing stratiform rain adjacent. Shallow or absent precipitation was observed first in specific regions of the storm where the cold pool was forming, but expanded to include much of the inner core by 0600 UTC September 12. Presence of the interactive ocean allows the depth and symmetry of convection, and ultimately the intensity to be adversely affected. As the storm's intensity weakens, particularly 1800 UTC September 11 – 0000 UTC September 12, the cold pool magnitude levels off ( $\sim 23.5 - 24^{\circ}\text{C}$  minimum SST) as the wind stress feedback is reduced. The presence of an interactive ocean is critical to producing the cold pool and explaining its distribution relative to wind-stress input from the storm, capturing the structure of the inner-core decay, and limiting vertical depth of the storm through ocean-to-atmosphere stabilization of the boundary layer atmosphere.

(3) Using time-series produced from UWIN-CM analysis, we were able to examine the timing of the structure and intensity changes in the context of the air-sea interaction. In particular, the timing of reintensification of the storm September 13 – 14 while the storm was over the Gulf Stream yielded a particularly intriguing result.

Beginning 0600 September 12, Ophelia's center was moving west-northwest away from its the cold pool. The inner core had weakened over the preceding 12h, and the storm began to expand by 0900 UTC September 12. The radius of maximum reflectivity expanded first, followed a few hours later by the RMW, reaching a maximum separation of ~60 km offset by 2-3 hours around 1200 UTC September 12. Ophelia's 34-kt winds were vast, though weak during this period, likely responsible for the cold pool spreading behind and slightly right of the track between 0600 – 1200 UTC. Due to the weak winds and T100, air-sea enthalpy flux was greatly reduced in the inner-core region. Distant discrete convection began to emerge after 1200 UTC, supported by warm Gulf Stream T100 and advection of high-enthalpy air that enhanced positive surface moisture disequilibrium. As more of the inner-core moved over  $> 26^{\circ}\text{C}$  T100, precipitation became increasingly discrete, cellular and more intense. The RMW steadily contracted, but the storm failed to intensify until 0000 UTC September 13, when Ophelia was fully over the Gulf Stream and the strongest convection was near and inside the RMW. Air-sea interaction facilitated structure and intensity change over the cold pool had consequences for the storm's dynamics and its future evolution, particularly the recovery. Intensity change occurred almost immediately when enthalpy flux was reduced (cold pool), but was delayed by the altered storm's structure and adjustment to a newly favorable ocean environment over the Gulf Stream, consistent with previous idealized ocean impact studies (e.g. Halliwell, et al. 2015). A brief summary of the differences in the evolution of precipitation structure and distribution in the model storms is given for four 'stages' in Ophelia's life cycle below in Figure 5.1.

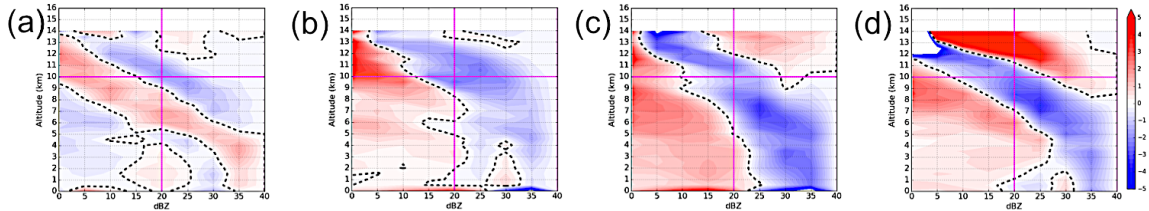


Figure 5.1 Grouped contoured frequency by altitude (CFAD) difference summary diagrams for radar reflectivity during the (a) organization, (b) cold-pool interaction, (c) expansion, and (d) recovery stages (left to right) in UWIN-CM AO – UA (frequency difference, % per dBZ per m). The magenta lines denote 10-kilometer altitude, 20 and 40 dBZ. The black dotted contour indicates 0%.

The summary CFADs above show the difference of AO – UA model radar reflectivity composited into four groups. Stage 1 is the organizing stage in the period after both model storms have spin-up, September 9 1500 – September 10 0000 UTC. Stage 2 is the time when the real Ophelia is weakening and asymmetric while interacting with its cold pool, September 11 1800 – September 12 0500 UTC. Stage 3, September 12 0600 – 1800 UTC, occurs immediately following the model storm departure away from the cold pool, when the real storm’s inner core remains weak, and the storm had expanded. The final stage encompasses Ophelia’s recovery over the Gulf Stream, September 13 0600 – 1800 UTC.

During spin-up, the model storms both have diagonal structure to the profiles, with precipitation spread across both weak and strong intensities. The uncoupled storm has greater frequency of stronger reflectivity returns (~20-30 dBZ) at higher altitudes (8–12 km) shown by the diagonal dark blue region. By comparison, the coupled storm dominated region of the profile is shifted to lower altitudes (~3-7 km for highest frequency difference over 20-35 dBZ relative to UA). Above 8 km, the coupled model storm also has more frequent weaker (<15 dBZ) reflectivity returns. Model pressure and intensity are nearly identical, with UA slightly stronger. Figure 5.1a demonstrates the

coupled storm has a similar, but weaker vertical distribution of precipitation with greater frequency of weaker reflectivity.

Between 1800 UTC September 11 and 0500 UTC September 12, the uncoupled storm begins its first period of organized intensification while the coupled storm weakens in response to upwelling and interaction with the resultant cold pool. In Figure 5.1b, the diverging intensity between the two storms is matched by stronger differences in the distribution and intensity of their precipitation. Strongly negative CFAD difference values dominate the 20+ dBZ region of the profile. This is most pronounced above 8 km for moderate returns (20 – 30 dBZ) and between 3-7 km for strong convective returns ( $> 30$  dBZ), demonstrating the uncoupled storm is stronger and deeper than AO during this period. AO has substantially higher weak return frequency, particularly at higher altitudes indicated by the large positive values on the left end of the profile. Interaction with the cold pool due to coupling resulted in a shallower, less intense TC (Figure 5.1b).

After traversing its cold pool, the real Ophelia expands, shallows further, and remains near-steady intensity with some slight weakening. The difference CFAD profile in Figure 5.1c shows an ~6-9 km region with weak returns favored for AO and much more frequent strong returns for UA. Almost the entire area less than 20 dBZ and below 10 km contains positive values, while the area over that vertical depth  $> 20$  dBZ is almost entirely negative. The strongly negative regions associated with UA dominating the reflectivity frequency are much more diagonal and narrower in spread than similar regions where AO dominates. While the coupled storm does have reflectivity above 10 km, the dBZ is very weak ( $\leq 10$  dBZ); the large positive region extends gradually closer to the surface approaching 15 dBZ. In summary, Figure 5.1c shows the largest region

where the coupled model reflectivity frequencies dominate is broad and shallow (less than 9 km) as the storm expands. Conversely, the UA-dominated region of the profile has a larger magnitude, is more compact, and extends almost continuously from the surface upward as the storm continues to intensify.

In the final stage, both model storms are over the Gulf Stream. The uncoupled storm undergoes RI during this period (0600 – 1200 UTC September 13). Diagonal positive and negative difference bands appear in the profile similar to the structure the storms had in Stage 1 (Figure 5.1a) but with a larger magnitude. Consistent with more organization of the uncoupled relative to the coupled storm, the negative difference section of the profile is strong and narrower. The segment extends continuously from the surface upward and splits the positive difference part of the profile into two sections. In AO, the TC is recovering over the Gulf Stream and re-establishing deep, more intense precipitation for the first time since prior to the cold-pool interaction. A diagonal band of positive difference values reaches from 0-25 dBZ from near 11km downward to 5km. A second, more strongly positive difference region including the 25-35 dBZ reflectivity range is seen between 10km and the top of the model. Overall, both storms are mature, but AO is slightly weaker and deeper than UA, which dominates more heavily from 0-8 km over the moderate to intense convection range (25+ dBZ).

Figure 5.2 presents Hovmoller diagrams of azimuthal average UWIN-CM AO TC and ocean structure. Specifically, radar reflectivity (dBZ), wind speed (kt), near-surface moisture convergence (g/kg/s) and T100 (deg C) show summary evolution of the precipitation, circulation, and proxies for the relative location of air-sea enthalpy flux modification.

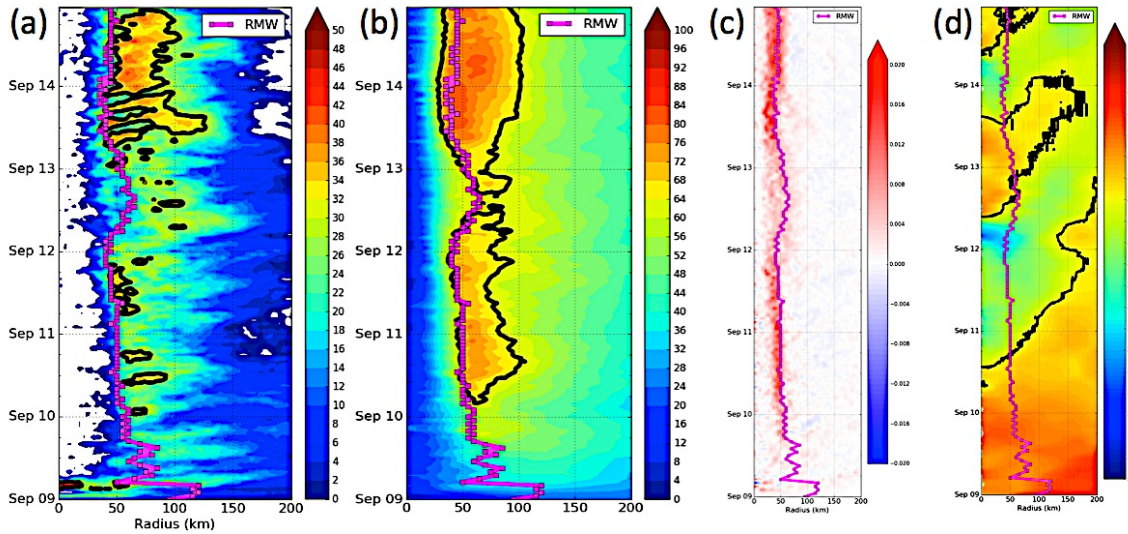


Figure 5.2 Hovmoller diagrams of UWIN-CM AO (a) flight-level radar reflectivity with 30 dBZ contours (b) flight-level wind speed with 64 kt contoured (c) 0.5km moisture convergence, and (d) T100 with 26.5C contoured. RMW is overlaid in magenta on all diagrams.

In Figure 5.2 (a) and (b), the inner core collapse and weakening of the azimuthal average circulation can be clearly seen. As the precipitation weakens there is a separation between approximately September 11 1800 UTC and September 12 0600 UTC (seen by the gap in 30 dBZ contours at about this time). This gap corresponds with the coldest T100 values inside and near the RMW. Although the model azimuthal average reflectivity and winds lack a clearly-defined secondary horizontal maxima, the expansion of the RMW and RMR following the cooling and inner core convection is gone are consistent with the formation of a secondary eyewall or rainband assuming eyewall-like structure that is commonly seen in EWRC. Additionally, when the UWIN-CM AO simulated storm reached maximum size, azimuthal average T100 was 26.5-27°C and positive moisture convergence extended over a 50km radial width. The question remains as to whether EWRC was initiated by TC-induced ocean cooling eroding the inner core, or interrupted an ongoing incipient EWRC. Overintensification of precipitation and wind intensity

relative to observations (Ophelia reached only Category 1 at maximum intensity), initial condition model ocean error, and track error may all contribute to difficulty discerning the specific structures in the azimuthal mean that are related to EWRC. Despite this, the fully-coupled UWIN-CM storm exhibits many symptoms of traditional EWRC that help explain its evolution and survival over intense upper ocean cooling: air-sea enthalpy flux cut-off in the inner core, presence of a second ring of discrete convection (here supported by non-local air-sea enthalpy flux), weakening or near-steady intensity change during the expanded stage, contraction and formation of a new eyewall. This recovery is the end-stage of EWRC, however additional research is needed.

## REFERENCES

- Anthes, R.A., 1974. The Dynamics and Energetics of Mature Tropical Cyclones. *Reviews of Geophysics*, 12(3), pp.495–522.
- Anthes, R.A. & Chang, S.W., 1978. Response of the Hurricane Boundary Layer to Changes of Sea Surface Temperature in a Numerical Model. *Journal of the Atmospheric Sciences*, 35(7), pp.1240–1255.
- Bender, M.A. & Ginis, I., 2000. Real-Case Simulations of Hurricane – Ocean Interaction Using A High-Resolution Coupled Model : Effects on Hurricane Intensity. *Monthly Weather Review*, 128(4), pp.917–946. Available at: [http://journals.ametsoc.org/doi/abs/10.1175/1520-0493\(2000\)128%3C0917:RCSOHO%3E2.0.CO;2](http://journals.ametsoc.org/doi/abs/10.1175/1520-0493(2000)128%3C0917:RCSOHO%3E2.0.CO;2).
- Black, M.L. et al., 2002. Eastern Pacific Hurricanes Jimena of 1991 and Olivia of 1994: The Effect of Vertical Shear on Structure and Intensity. *Monthly Weather Review*, 130, pp.2291–2312. Available at: [http://dx.doi.org/10.1175/1520-0493\(2002\)130%3C2291:EPHJOA%3E2.0.CO;2](http://dx.doi.org/10.1175/1520-0493(2002)130%3C2291:EPHJOA%3E2.0.CO;2).
- Bosart, L.F. et al., 2000. Environmental Influences on the Rapid Intensification of Hurricane Opal (1995) over the Gulf of Mexico. *Monthly Weather Review*, 128(2), pp.322–352. Available at: [http://journals.ametsoc.org/doi/abs/10.1175/1520-0493\(2000\)128%3C0322:EIOTRI%3E2.0.CO;2](http://journals.ametsoc.org/doi/abs/10.1175/1520-0493(2000)128%3C0322:EIOTRI%3E2.0.CO;2).
- Busch, N.E., Chang, S.W. & Anthes, R.A., 1976. A Multi-Level Model of the Planetary Boundary Layer Suitable for Use with Mesoscale Dynamic Models. *Journal of Applied Meteorology*, 15(9), pp.909–919.
- Camp, J.P. & Montgomery, M.T., 2001. Hurricane Maximum Intensity: Past and Present. *Monthly Weather Review*, 129(7), pp.1704–1717.
- Cangialosi, J. & Chen, S.S., 2004. A Numerical Study of the Topographic Effects on Structure and Rainfall in Hurricane Georges (1998). *26th Conference on Hurricanes and Tropical Meteorology*, pp.528–529. Available at: <http://www.scopus.com/inward/record.url?eid=2-s2.0-3042786541&partnerID=tZOTx3y1>.
- Chan, J., Duan, Y. & Shay, L., 2001. Tropical Cyclone Intensity Change From A Simple Ocean-Atmosphere Coupled Model. *Journal of the Atmospheric Sciences*, 58(2), pp.154–172. Available at: [http://apps.webofknowledge.com/full\\_record.do?product=UA&search\\_mode=GeneralSearch&qid=1&SID=S1dRY4S4N ZyZqZnLiEC&page=1&doc=10&cacheurlFromRightClick=no](http://apps.webofknowledge.com/full_record.do?product=UA&search_mode=GeneralSearch&qid=1&SID=S1dRY4S4N ZyZqZnLiEC&page=1&doc=10&cacheurlFromRightClick=no).
- Charney, J.G. & Eliassen, A., 1964. On the Growth of the Hurricane Depression. *Journal of the Atmospheric Sciences*, 21(1), pp.68–75

- Chen, S.S. et al., 2013. Directional Wind–Wave Coupling in Fully Coupled Atmosphere–Wave–Ocean Models: Results from CBLAST-Hurricane. *Journal of the Atmospheric Sciences*, 70(10), pp.3198–3215. Available at: <http://journals.ametsoc.org/doi/abs/10.1175/JAS-D-12-0157.1>.
- Chen, S.S. et al., 2007. The CBLAST-Hurricane Program and The Next-Generation Fully Coupled Atmosphere-Wave-Ocean Models for Hurricane Research and Prediction. *Bulletin of the American Meteorological Society*, 88(3), pp.311–317.
- Chen, S.S. & Curcic, M., 2016. Ocean Surface Waves in Hurricane Ike (2008) and Superstorm Sandy (2012): Coupled Model Predictions and Observations. *Ocean Modelling*, 103(2007), pp.161–176.
- Chen, S.S., Knaff, J. a. & Marks, F.D., 2006. Effects of Vertical Wind Shear and Storm Motion on Tropical Cyclone Rainfall Asymmetries Deduced from TRMM. *Monthly Weather Review*, 134(11), pp.3190–3208. Available at: <http://journals.ametsoc.org/doi/abs/10.1175/MWR3245.1>.
- Cione, J.J. et al., 2013. Observations of Air–Sea Interaction and Intensity Change in Hurricanes. *Monthly Weather Review*, 141(7), pp.2368–2382. Available at: <http://journals.ametsoc.org/doi/abs/10.1175/MWR-D-12-00070.1>.
- Cione, J.J., 2015. The Relative Roles of the Ocean and Atmosphere As Revealed By Buoy Air-Sea Observations in Hurricanes. *Monthly Weather Review*, 143(2003), pp.904–913.
- Cione, J.J. & Uhlhorn, E.W., 2003. Sea Surface Temperature Variability in Hurricanes: Implications with Respect to Intensity Change. *Monthly Weather Review*, 131(8), pp.1783–1796.
- Corbosiero, K.L., Molinari, J. & Black, M.L., 2005. The Structure and Evolution of Hurricane Elena (1985). Part I: Symmetric Intensification. *Monthly Weather Review*, 133(10), pp.2905–2921.
- Curcic, M., 2015. Explicit Air-Sea Momentum Exchange in Coupled Atmosphere-Wave-Ocean Modeling of Tropical Cyclones.
- Curcic, M., Chen, S.S. & Özgökmen, T.M., 2016. Hurricane-Induced Ocean Waves and Stokes Drift and Their Impacts On Surface Transport and Dispersion in the Gulf of Mexico. *Geophysical Research Letters*, pp.1–9.
- D’Asaro, E.A. et al., 2014. Impact of Typhoons On the Ocean in the Pacific. *Bulletin of the American Meteorological Society*, 95(9), pp.1405–1418.

- Dare, R.A. & McBride, J.L., 2011. Sea Surface Temperature Response to Tropical Cyclones. *Monthly Weather Review*, 139(12), pp.3798–3808. Available at: <http://www.scopus.com/inward/record.url?eid=2-s2.0-84855813573&partnerID=tZOTx3y1>.
- DeMaria, M. & Kaplan, J., 1994. A Statistical Hurricane Intensity Prediction Scheme (SHIPS) for the Atlantic Basin. *Wea. Forecasting*, 9, pp.209–220. Available at: [http://dx.doi.org/10.1175/1520-0434\(1994\)009%3C0209:ASHIPS%3E2.0.CO;2](http://dx.doi.org/10.1175/1520-0434(1994)009%3C0209:ASHIPS%3E2.0.CO;2).
- Dudhia, J., 1993. A Nonhydrostatic Version of the Penn State–NCAR Mesoscale Model: Validation Tests and Simulation of an Atlantic Cyclone. *Monthly Weather Review*, 121(5), pp.1493–1513.
- Dunion, J.P. & Velden, C.S., 2004. The Impact of the Saharan Air Layer on Atlantic Tropical Cyclone Activity. *Bulletin of the American Meteorological Society*, 85(3), pp.353–365.
- Elsberry, R.L., Fraim, T.S. & Trapnell, R.N., 1976. A Mixed Layer Model of The Oceanic Thermal Response to Hurricanes. *Journal of Geophysical Research*, 81(6), p.1153.
- Emanuel, K.A., 1986. An Air-Sea Interaction Theory for Tropical Cyclones. Part I: Steady-State Maintenance. *Journal of the Atmospheric Sciences*, 43(6), pp.585–605.
- Fisher, E.L., 1958. The Exchange of Energy Between The Sea and the Atmosphere in Relation to Hurricane Behavior. *Journal of Meteorology*, 15, pp.164–171.
- Gamache, J.F. et al., 2003. Automatic Doppler Analysis of Three-Dimensional Wind Fields in Hurricane Eyewalls. In *Preprints, 26<sup>th</sup> Conference on Hurricanes and Tropical Meteorology*.
- Gilhousen, D.B., 1987. A Field Evaluation of NDBC Moored Buoy Winds. *Journal of Atmospheric and Oceanic Technology*, 4(1), pp.94–104. Available at: [http://journals.ametsoc.org/doi/abs/10.1175/1520-0426\(1987\)004%3C0094:AFEONM%3E2.0.CO;2](http://journals.ametsoc.org/doi/abs/10.1175/1520-0426(1987)004%3C0094:AFEONM%3E2.0.CO;2).
- Gray, W.M., 1968. Global View of the Origin of Tropical Disturbances and Storms. *Monthly Weather Review*, 96(10), pp.669–700.
- Gray, W.M., Ruprecht, E. & Phelps, R., 1975. Relative Humidity in Tropical Weather Systems. *Monthly Weather Review*, 103(8), pp.685–690. Available at: [http://journals.ametsoc.org/doi/abs/10.1175/1520-0493\(1975\)103%3C0685:RHITWS%3E2.0.CO%3B2](http://journals.ametsoc.org/doi/abs/10.1175/1520-0493(1975)103%3C0685:RHITWS%3E2.0.CO%3B2).
- Grell, G.A., Dudhia, J. & Stauffer, D.R., 1994. A Description of the Fifth-generation Penn State/NCAR Mesoscale Model (MM5). *NCAR Technical Note NCAR/TN-398+STR*, (December), p.121.

- Halliwell, G.R. et al., 2015. Idealized Study of Ocean Impacts on Tropical Cyclone Intensity Forecasts. *Monthly Weather Review*, 143(4), pp.1142–1165. Available at: <http://journals.ametsoc.org/doi/abs/10.1175/MWR-D-14-00022.1>.
- Hildebrand, P.H. et al., 1996. The ELDORA/ASTRAIA Airborne Doppler Weather Radar: High-Resolution Observations from TOGA COARE. *Bulletin of the American Meteorological Society*, 77(2), pp.213–232.
- Hill, C. et al., 2004. The Architecture of the Earth System Modeling Framework. *Computing in Science & Engineering*, 6(1), pp.18–28.
- Hong, S.-Y., Noh, Y. & Dudhia, J., 2006. A New Vertical Diffusion Package With An Explicit Treatment of Entrainment Processes. *Monthly Weather Review*, 134(9), pp.2318–2341. Available at: <http://journals.ametsoc.org/doi/abs/10.1175/MWR3199.1>.
- Hong, X. et al., 2000. The Interaction Between Hurricane Opal (1995) and a Warm Core Ring in the Gulf of Mexico. *Monthly Weather Review*, 128(5), pp.1347–1365.
- Houze, R.A. et al., 2006. The Hurricane Rainband and Intensity Change Experiment. *Bulletin of the American Meteorological Society*, 87(11), pp.1503–1521.
- Jacob, S.D. et al., 2000. The 3D Oceanic Mixed Layer Response to Hurricane Gilbert. *Journal of Physical Oceanography*, 30(6), pp.1407–1429. Available at: <http://www.scopus.com/inward/record.url?eid=2-s2.0-0033855475&partnerID=tZOTx3y1>.
- Jordan, C.L., 1958. Mean Soundings for the West Indies Area. *Journal of Meteorology*, 15(1), pp.91–97.
- Jordan, C.L., 1964. On The Influence of Tropical Cyclones On the Sea Surface Temperature. In *Proceedings from the Symposium on Tropical Meteorology*. pp. 614–622.
- Kain, J.S. & Fritsch, J.M., 1993. Convective Parameterization for Mesoscale Models: The Kain-Fritsch Scheme. In *The Representation of Cumulus Convection in Numerical Models* (pp. 165-170). American Meteorological Society.
- Lee, C.-Y. & Chen, S.S., 2014. Stable Boundary Layer and Its Impact on Tropical Cyclone Structure in a Coupled Atmosphere–Ocean Model. *Monthly Weather Review*, 142(5), pp.1927–1944. Available at: <http://journals.ametsoc.org/doi/abs/10.1175/MWR-D-13-00122.1>.
- Lee, C.-Y. & Chen, S.S., 2012. Symmetric and Asymmetric Structures of Hurricane Boundary Layer in Coupled Atmosphere-Wave-Ocean Models and Observations. *Journal of the Atmospheric Sciences*, p.120627080711003.
- Leipper, D.F., 1967. Observed Ocean Conditions and Hurricane Hilda, 1964. *Journal of*

- the Atmospheric Sciences*, 24(2), pp.182–186.
- Leipper, D.F. & Volgenau, D., 1972. Hurricane Heat Potential of the Gulf of Mexico. *Journal of Physical Oceanography*, 2, pp.218–224.
- Lorsolo, S., Gamache, J. & Aksoy, A., 2013. Evaluation of the Hurricane Research Division Doppler Radar Analysis Software Using Synthetic Data. *Journal of Atmospheric and Oceanic Technology*, 30(6), pp.1055–1071.
- Malkus, J.S., 1958. On the Structure and Maintenance of the Mature Hurricane Eye. *Journal of Meteorology*, 15(4), pp.337–349.
- Malkus, J.S. & Riehl, H., 1960. On the Dynamics and Energy Transformations in Steady-State Hurricanes. *Tellus A*, 12(1), pp.1–20.
- Marks, F.D. & Houze, R.A., 1984. Airborne Doppler Radar Observations in Hurricane Debby. *Bulletin of the American Meteorological Society*, 65(6), pp.569–582. Available at: [http://journals.ametsoc.org/doi/abs/10.1175/1520-0477\(1984\)065%3C0569%3AADROIH%3E2.0.CO%3B2](http://journals.ametsoc.org/doi/abs/10.1175/1520-0477(1984)065%3C0569%3AADROIH%3E2.0.CO%3B2).
- Marks, F.D. & Shay, L.K., 1998. Landfalling Tropical Cyclones: Forecast Problems and Associated Research Opportunities. *Bulletin of the American Meteorological Society*, 79(2), pp.308–323.
- Miller, B.I., 1958. On the Maximum Intensity of Hurricane. *Journal of Meteorology*, 15, pp.184–195.
- Nguyen, L.T. & Molinari, J., 2012. Rapid Intensification of a Sheared, Fast-Moving Hurricane over the Gulf Stream. *Monthly Weather Review*, 140(10), pp.3361–3378.
- Ooyama, K. V., 1969. Numerical Simulation of the Life Cycle of Tropical Cyclones. *Journal of the Atmospheric Sciences*, 26, pp.3–40. Available at: [http://dx.doi.org/10.1175/1520-0469\(1969\)026%3C0003:NSOTLC%3E2.0.CO;2](http://dx.doi.org/10.1175/1520-0469(1969)026%3C0003:NSOTLC%3E2.0.CO;2).
- Palmen, E., 1948. On the Formation and Structure of Tropical Hurricanes. *Geophysica*, 3, pp.26–38.
- Peng, M.S., Jeng, B.-F. & Williams, R.T., 1999. A Numerical Study on Tropical Cyclone Intensification. Part I: Beta Effect and Mean Flow Effect. *Journal of the Atmospheric Sciences*, pp.1404–1423.
- Perlboth, I., 1967. Hurricane Behavior As Related To Oceanographic Environmental Conditions. *Tellus*. Available at: <http://onlinelibrary.wiley.com/doi/10.1111/j.2153-3490.1967.tb01481.x/abstract>.
- Perlroth, I., 1969. Effects of Oceanographic Media on Equatorial Atlantic Hurricanes. *Tellus*, pp.230–244.

- Powell, M.D. & Reinhold, T.A., 2007. Tropical Cyclone Destructive Potential By Integrated Kinetic Energy. *Bulletin of the American Meteorological Society*, 88(4), pp.513–526.
- Price, J.F., 2009. Metrics of Hurricane-Ocean Interaction: Vertically-Integrated or Vertically-Averaged Ocean Temperature? *Ocean Science*, 5(3), pp.351–368.
- Price, J.F., 1981. Upper Ocean Response to a Hurricane. *Journal of Physical Oceanography*, 11(2), pp.153–175.
- Price, J.F., Sanford, T.B. & Forristall, G.Z., 1994. Forced Stage Response to a Moving Hurricane. *Journal of Physical Oceanography*, 24(2), pp.233–260.
- Rappaport, E.N. et al., 2009. Advances and Challenges at the National Hurricane Center. *Weather and Forecasting*, 24(2), pp.395–419.
- Reasor, P.D., Eastin, M.D. & Gamache, J.F., 2009. Rapidly Intensifying Hurricane Guillermo (1997). Part I: Low-Wavenumber Structure and Evolution. *Monthly Weather Review*, 137(2), pp.603–631. Available at: <http://dx.doi.org/10.1175/2008MWR2487.1%5Cnhttp://journals.ametsoc.org/doi/abs/10.1175/2008MWR2487.1>.
- Riehl, H., 1954. *Tropical Meteorology*, New York, NY: McGraw-Hill.
- Rogers, R. et al., 2003. A Numerical Study of the Impact of Vertical Shear on the Distribution of Rainfall in Hurricane Bonnie (1998). *Monthly Weather Review*, 131(8), pp.1577–1599. Available at: <http://journals.ametsoc.org/doi/abs/10.1175//2546.1>.
- Rogers, R. et al., 2006. The Intensity Forecasting Experiment: A NOAA Multiyear Field Program for Improving Tropical Cyclone Intensity Forecasts. *Bulletin of the American Meteorological Society*, 87(11), pp.1523–1537.
- Rogers, R., Reasor, P. & Lorsolo, S., 2013. Airborne Doppler Observations of the Inner-Core Structural Differences between Intensifying and Steady-State Tropical Cyclones. *Monthly Weather Review*, 141(9), pp.2970–2991. Available at: <http://journals.ametsoc.org/doi/abs/10.1175/MWR-D-12-00357.1>.
- Rosenthal, S.L., 1971. The Response of a Tropical Cyclone Model to Variations in Boundary Layer Parameters, Initial Conditions, Lateral Boundary Conditions, and Domain Size. *Monthly Weather Review*, 99(10), pp.767–777.
- Rotunno, R. & Emanuel, K.A., 1987. An Air–Sea Interaction Theory for Tropical Cyclones. Part II: Evolutionary Study Using a Nonhydrostatic Axisymmetric Numerical Model. *Journal of the Atmospheric Sciences*, 44(3), pp.542–561.

- Samsury, C.E. & Zipser, E.J., 1995. Secondary Wind Maxima in Hurricanes: Airflow and Relationship to Rainbands. *Monthly Weather Review*, 123(12), p.3502. Available at: [http://adsabs.harvard.edu/cgi-bin/nph-data\\_query?bibcode=1995MWRv..123.3502S&link\\_type=EJOURNAL%5Cn\(null\)](http://adsabs.harvard.edu/cgi-bin/nph-data_query?bibcode=1995MWRv..123.3502S&link_type=EJOURNAL%5Cn(null)).
- Schade, L.R. & Emanuel, K.A., 1999. The Ocean's Effect on the Intensity of Tropical Cyclones: Results from a Simple Coupled Atmosphere–Ocean Model. *Journal of the Atmospheric Sciences*, 56(4), pp.642–651.
- Shapiro, L.J. & Willoughby, H.E., 1982. The Response of Balanced Hurricanes to Local Sources of Heat and Momentum. *Journal of the Atmospheric Sciences*, 39(2), pp.378–394.
- Shay, L.K. et al., 1992. Upper Ocean Response to Hurricane Gilbert. *Journal of Geophysical Research*, 97(C12), p.20227.
- Shay, L.K., Goni, G.J. & Black, P.G., 2000. Effects Of a Warm Oceanic Feature on Hurricane Opal. *Monthly Weather Review*, 128(5), pp.1366–1383. Available at: <http://www.scopus.com/inward/record.url?eid=2-s2.0-0033913432&partnerID=tZOTx3y1>.
- Shea, D.J. & Gray, W.M., 1973. The Hurricane's Inner Core Region. I. Symmetric and Asymmetric Structure. *Journal of the Atmospheric Sciences*, 30(8), pp.1544–1564. Available at: [http://journals.ametsoc.org/doi/abs/10.1175/1520-0469\(1973\)030%3C1544%3A%2E2.0.CO%3B2%5Cnhttp://hurricane.atmos.colostate.edu/Includes/Documents/Publications/sheagray1973.pdf](http://journals.ametsoc.org/doi/abs/10.1175/1520-0469(1973)030%3C1544%3A%2E2.0.CO%3B2%5Cnhttp://hurricane.atmos.colostate.edu/Includes/Documents/Publications/sheagray1973.pdf).
- Skamarock, W.C. & Klemp, J.B., 2007. A Time-Split Nonhydrostatic Atmospheric Model for Weather Research and Forecasting Applications. , (1), pp.1–43.
- Surgi, N. et al., 2006. Hurricane Initialization in HWRF Model. In *27th Conference on Hurricanes and Tropical Meteorology*. pp. 2–3.
- Tenerelli, J.E. et al., 2001. High-Resolution Simulations of Hurricane Floyd using MM5 Coupled with a Wave Model. *Tenth PSU/NCAR Mesoscale Model User's Workshoop*.
- Testud, J., Hildebrand, P.H. & Lee, W.-C., 1995. A Procedure to Correct Airborne Doppler Radar Data for Navigation Errors Using the Echo Returned from the Earth's Surface. *Journal of Atmospheric and Oceanic Technology*, 12(4), pp.800–820. Available at: <http://journals.ametsoc.org/doi/abs/10.1175/1520-0426%281995%29012%3C0800%3AAPTCAD%3E2.0.CO%3B2>.
- Uhlhorn, E.W. et al., 2007. Hurricane Surface Wind Measurements from an Operational Stepped Frequency Microwave Radiometer. *Monthly Weather Review*, 135(9), pp.3070–3085. Available at: <http://dx.doi.org/10.1175/MWR3454.1>.

- Uhlhorn, E.W. & Black, P.G., 2003. Verification of Remotely Sensed Sea Surface Winds in Hurricanes. *Journal of Atmospheric and Oceanic Technology*, 20(1), pp.99–116.
- Wallcraft, A.J., Metzger, E.J. & Carroll, S.N., 2009. Software Design Description for the HYbrid Coordinate Ocean Model ( HYCOM ) Version 2.2. , p.NRL/MR/732009-9166.
- Willoughby, H.E., 1988. The Dynamics of Tropical Cyclone Core. *Aust. Met. Mag.*, 36, pp.183–191.
- Willoughby, H.E., Clos, J.A. & Shoreibah, M.G., 1982. Concentric Eye Walls, Secondary Wind Maxima, and The Evolution of the Hurricane vortex. *Journal of the Atmospheric Sciences*, 39(2), pp.395–411. Available at: [http://adsabs.harvard.edu/cgi-bin/nph-data\\_query?bibcode=1982JAtS...39..395W&link\\_type=ABSTRACT%5Cn\(null\)](http://adsabs.harvard.edu/cgi-bin/nph-data_query?bibcode=1982JAtS...39..395W&link_type=ABSTRACT%5Cn(null)).
- Willoughby, H.E., Marks, F.D. & Feinberg, R.J., 1984. Stationary and Moving Convective Bands in Hurricanes. *Journal of the Atmospheric Sciences*, 41(22), pp.3189–3211.
- Wimmers, A.J. & Velden, C.S., 2007. MIMIC: A New Approach to Visualizing Satellite Microwave Imagery of Tropical Cyclones. *Bulletin of the American Meteorological Society*, 88(8), pp.1187–1196.
- Wu, C.-C., Lee, C.-Y. & Lin, I.-I., 2007. The Effect of the Ocean Eddy on Tropical Cyclone Intensity. *Journal of the Atmospheric Sciences*, 64(10), pp.3562–3578.
- Yuter, S.E. & Houze, R. a., 1995. Three-Dimensional Kinematic and Microphysical Evolution of Florida Cumulonimbus. Part II: Frequency Distributions of Vertical Velocity, Reflectivity, and Differential Reflectivity. *Monthly Weather Review*, 123(7), pp.1941–1963. Available at: [http://journals.ametsoc.org/doi/abs/10.1175/1520-0493\(1995\)123%3C1941:TDKAME%3E2.0.CO;2](http://journals.ametsoc.org/doi/abs/10.1175/1520-0493(1995)123%3C1941:TDKAME%3E2.0.CO;2).

